JOHANNES GUTENBERG UNIVERSITÄT MAINZ

Institute of Physics

A Single-Ion Autonomous Clock

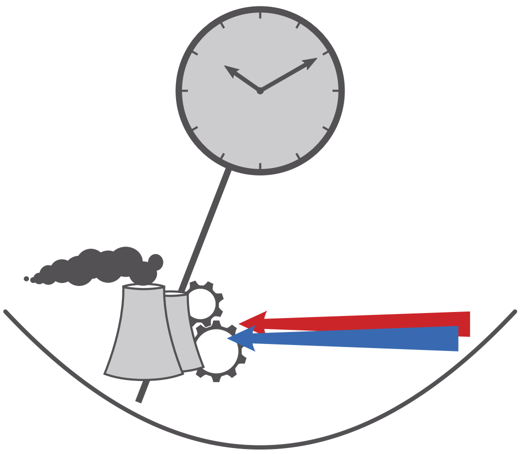

A thesis submitted in partial fulfillment of the requirements for the degree of

Master of Science

By Martin Wagener

Submitted by:	Martin Wagener Johannes Gutenberg-Universität Mainz Institute of Physics Staudingerweg 7 55128 Mainz
Matriculation Number:	2731788
Supervisor:	Dr. Ulrich Poschinger
1. Evaluator:	Prof. Dr. Ferdinand Schmidt-Kaler
2. Evaluator:	Prof. Dr. Randolf Pohl
Submitted on:	6. December 2018

This document is set in Palatino, compiled with pdfLaTeX and `Biber`.

It is based on a LaTeX template from Karl Voit, which can be found at
https://github.com/novoid/LaTeX-KOMA-template,
and uses KOMA script

Statutory Declaration

I declare that I have authored this thesis independently, that I have not used other than the declared sources/resources, and that I have explicitly marked all material which has been quoted either literally or by content from the used sources.

Eidesstattliche Erklärung

Hiermit erkläre ich, dass ich die vorliegende Arbeit selbstständig und nur unter Zuhilfenahme der ausgewiesenen Hilfsmittel angefertigt habe. Sämtliche Stellen der Arbeit, die im Wortlaut oder dem Sinn nach anderen Werken entnommen sind, habe ich durch genaue Quellenangaben kenntlich gemacht.

Mainz, ______________________ ______________________

Date Signature

Zusammenfassung

In dieser Arbeit stellen wir die experimentelle Realisierung einer autonomen Uhr vor, die auf einem von Strahlungsdruck getriebenen, gefangen Ion basiert – einem *Phononen Laser*. Das vom Ion emittierte Fluoreszenzlicht ist mit der Schwingungsfrequenz modelliert. Die Detektionszeiten der emittierten Photonen bilden daher ein 'klick'-Signal welches zur Zeitmessung genutzt werden kann. Ein theoretisches Modell des Systems wurde entwickelt, welches die Herleitung eines Phasendiffusionskoeffizienten ermöglicht. Dieser kann genutzt werden um die Stabilität der Uhr in Zusammenhang mit den Operationsparametern zu bringen. Die Allan-Varianz wird verwendet um die Uhrenstabilität zu quantifizieren und wir präsentieren ein Verfahren um sie aus den gestreuten Photonen zu bestimmen. Neben der detaillierten Analyse der gemessenen Daten werden wir Zusammenhänge zwischen der Stabilität und den thermodynamischen Ressourcen untersuchen, die nötig sind um die Uhr zu betreiben. Die hier vorgestellten Daten stehen zu großen Teilen in Konflikt mit der entwickelten Theorie. Im Laufe der Arbeit werden wir mögliche Gründe dafür diskutieren und mögliche Verbesserungen vorschlagen. Zusätzlich zu diesen Messungen der Uhrenstabilität werden wir Methoden einführen um die Operationsparameter zu kalibrieren. Dies beinhaltet den Sättigungsparameter und die Frequenzverstimmung der Laser, die für den Antrieb der Uhr genutzt werden und die Messung der absoluten Streurate des Ions.

Abstract

In this thesis, we describe the experimental implementation of an autonomous clock based on a radiation-pressure driven trapped-ion *phonon laser*. The resonance fluorescence emitted by the ion is modulated at the oscillator frequency, therefore the detection times of the scattered photons provide a 'click' signal which can serve for timekeeping. We provide a theoretical analysis of this system, which includes the derivation of a phase-diffusion constant, which serves to relate the clock stability to the operation parameters. We describe the employed measurement protocol used to assess the clock performance in terms of its Allan variance, and present a detailed analysis of acquired data. Furthermore, we evaluate connections of the clock performance to the thermodynamical cost that is required to drive it. The data acquired in the course of this thesis do exhibit qualitative conflicts with the theoretical predictions. Possible reasons for this finding are investigated and improved measurement schemes are proposed. Furthermore, we present auxiliary measurement schemes employed for precise calibration the operation parameters, namely the detunings and saturation parameters for the laser beams driving the autonomous clock, and for measurement of the total photon scattering rates.

Contents

Acronyms

AOM	acousto-optical modulator
DC	direct current
EMCCD	electron multiplying charge-coupled device
EOM	electro optical modulator
FFM	flicker frequency modulation
FPM	flicker phase modulation
FWHM	full width at half maximum
IQR	interquartile range
PBS	polarizing beam splitter
PMT	photomultiplier tube
RAP	rapid adiabatic passage
RF	radio frequency
RWFM	random walk frequency modulation
RWPM	random walk phase modulation
TLS	two-level system
TTL	transistor-transistor logic
VCO	voltage-controlled oscillator
WFM	white frequency modulation
WPM	white phase modulation

Symbols

Atom-Light Interaction

γ	natural line width.
δ	frequency detuning from resonance.
$\mathbf{d}$	dipole operator.
$\mathcal{D}$	matrix element of the dipole operator.
$\tilde{\mathcal{D}}$	reduced matrix element of the dipole operator.
Ω	Rabi frequency.
$\tilde{\Omega}$	reduced Rabi frequency.
S_0	resonant saturation parameter.
Γ	scattering rate.
$\mathbf{k}$	wavevector.

The Ion Oscillator

v	velocity of the ion.
ν	velocity dependent forces on the ion caused by light pressure.
λ	velocity dependent intensity of the Langevin force on the ion.
ϕ	oscillation phase of the ion.
ω	oscillation frequency of the ion.
S_c, S_a	resonant saturation parameter of the cooling and amplification beam.
$\delta_a\ \delta_c$	frequency detunings from resonance for amplification and cooling beam.
$\alpha_a\ \alpha_c$	dimensionless frequency detunings from resonance for amplification and cooling beam.
β, β_{OP}	dimensionless oscillation amplitude of the ion and the steady state amplitude (operating point).
D_ϕ	phase diffusion coefficient.

Miscellaneous

σ_y^2	Allan variance.
$R_\pm$	spin flip rates.
S_y	power spectral density.
ξ	2ξ is the full width at half maximum (FWHM) of the broadening lorentzian.
$\hbar$	Planck constant.
μ_B	Bohr magneton.

1. Introduction

Laser cooled atomic ions in Paul traps [1, 2] are an ideal platform for numereous experiments where a high degree of control over motional and internal degrees of freedom is necessary. Laser cooling [3, 4] enables cooling to the motional ground state [5] and coherent excitation can be used to achieve control over the internal quantum state of the ion [6, 7]. These methods are widely used for quantum information, metrology, simulation and computing [8, 9, 10]. In recent years trapped ions have also been used to implement thermal machines on the quantum level [11, 12]. The validity of concepts commonly known from macroscopic heat engines like heat, work, efficiency and entropy can be investigated. It is a goal of the emerging field of *quantum thermodynamics* to explore new features of these machines that arise due to their quantum character [13, 14, 15]. Erker et al. [16] have theoretically studied an autonomous quantum clock based on a microscopic heat engine to investigate the connections between thermodynamics and time.

In standard thermodynamics, time plays an important role through the concept of irreversibility. If a process is irreversible, i.e. if the total entropy is increased, a direction for the arrow of time is established. Thus there is already a quite fundamental connection between time and thermodynamics in classical physics. Erker et al. have taken this one step further and investigated connections between *time measurement* and entropy. Regarding the periodic cycles of their autonomous heat engine as ticks of a clock, they find that waste heat, i.e. entropy production, is a resource needed for accurate time keeping. Initially, this is a result limited to their specific system. Their argument is then extended to general clocks. They conjecture that entropy production is necessary for arbitrary time measurement devices and that a fixed entropy production sets an upper bound for the performance of the clock. This can be compared to other fundamental limits as the Landauer limit [17] or the quantum speed limit [18]. Just as state-of-the-art computers operate far away from these limits, common clocks are far from being thermodynamically efficient and are not limited by entropy production. Finding a system to test this conjecture is therefore not necessarily easy.

In this thesis, we propose that a single ion which is oscillating in an harmonic trap driven by radiation pressure forces is a reasonable candidate. This system was first implemented by Vahala et al. [19] [1]. Due to its similarities to an optical laser it has been named *phonon laser* by them. A laser beam blue detuned from an electric dipole transition supplies energy to the ion in each oscillation cycle. This can be seen analogous to a pendulum in a mechanical clock which is likewise supplied with energy during each cycle to overcome losses through friction. The photons scattered by the ion are modulated

[1] A similar system was independently proposed by Kaplan [20]

with the oscillation frequency and can therefore be detected to obtain a periodic clock signal. Additionally, the scattered photons are also our measure of waste heat as they are scattered from the low entropy laser beam into random vacuum modes. In contrast to the heat engine driven clock or frequency standards, the oscillation frequency of the ion is fixed by the trapping potential. However, the radiation pressure of the driving beams will have an effect on the oscillation phase and thus the oscillation stability. The goal of this thesis will consequently be to investigate connections between the oscillation stability and the scattering rate and to relate them to the work by Erker et al.

The aim of this thesis is *not* to construct an atomic clock using Ramsey interferometry or to compete with the accuracy of such devices. In contrast to atomic clocks, our system runs *autonomous* and the oscillation phase is not governed by any external control. Here, the essential part of the clock is the ion itself and its motional degrees of freedom, making it a "pendulum" clock in the microscopic limit.

Supplementing the oscillation stability measurements, we will introduce a scheme to measure the photon detection efficiency of the setup. This is relevant as the photon scattering rate will be our measure of waste heat and to quantify the amount of scattering per oscillation period. Additionally, we present a method of calibrating the resonant saturation parameter and the frequency detuning of a laser beam driving a certain atomic dipole transition. This enables us to quantify the forces exerted on the ion by the lasers and to relate measurements and theory.

Below, we will first give a short overview over the work on heat engines by Erker et al. and introduce the proposed ion phonon laser clock. Then the required theoretical foundations are discussed in Chapter 2. This will include a brief introduction into the interaction between atoms and light and the theoretical model of the oscillating ion in a trap, which has been developed in close collaboration with Nahuel Freitas. In Chapter 3, the experimental setup including the actual ion trap, electronics and lasers are reviewed. Subsequently, the two supplementary measurement schemes are introduced in Chapter 4 and Chapter 5. Finally, the oscillation stability measurements are explained and presented in Chapter 6 and then discussed in Chapter 7. In Chapter 8 we then summarize the results of this thesis and give an outlook for future measurements and improvements.

1.1. A Microscopic Clock Driven by a Heat Engine

In [16] Erker et al. show that for a microscopic clock increasing its performance in terms of stability or resolution requires increased production of waste heat, i.e. entropy production. They use the periodicity of an autonomous heat engine, based on a quantum system, as a clock and show analytically and through simulations that such a connection exists in this system. They conjecture that this is a fundamental connection between time measurement and thermodynamics and that any clock will show such a behavior. In this section, this heat engine model will be introduced before discussing their findings and the connection to this thesis.

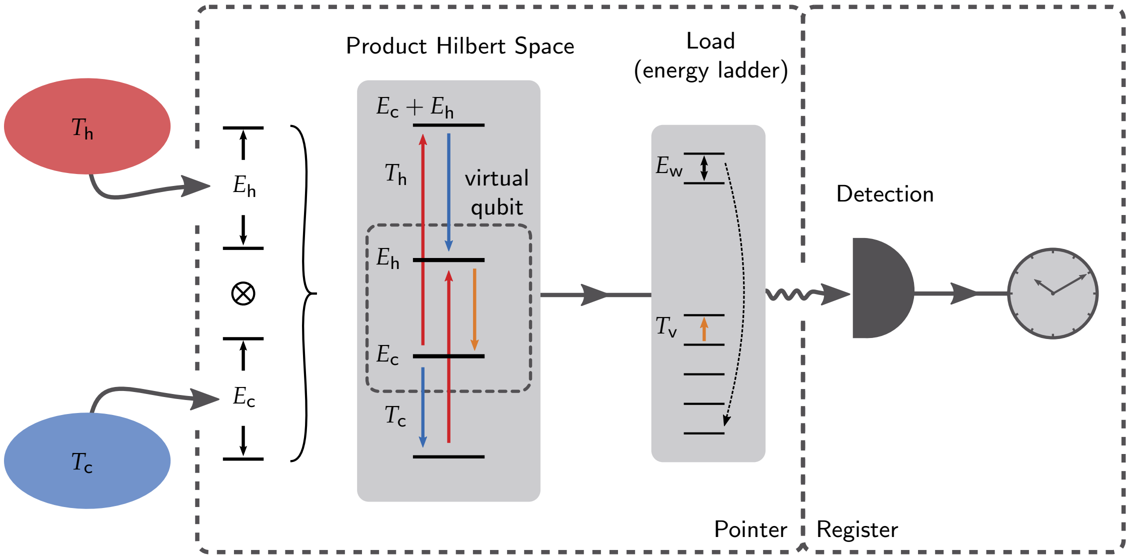

Figure 1.1.: Sketch of the theoretical model of a heat engine used as a clock in [16]. The system consists of two main parts: The pointer and the register. The interaction of the pointer with the environment is well defined and happens only through the qubits connected to the two thermal baths at temperatures T_c and T_h to allow rigorous bookkeeping of the heat flowing in and out of the system. The two qubits with energy spacing E_c and E_h form a four dimensional product Hilbert space of which the two middle levels are defined as the *virtual* qubit. Interaction with the baths drives the transitions inside this Hilbert space (red and blue arrows). Additionally, the qubits interact with an energy ladder which has an energy spacing $E_w = E_h - E_c$ matching that of the virtual qubit. If the virtual Temperature T_v is negative, a virtual qubit decay can drive the ladder up by one rung (orange arrows). Coupling of the upmost and lowest levels of the ladder leads to a decay which happens periodically each time the top is reached. This decay can now be transmitted to the register where it is moves the hands of a clock forward.

1.1.1. The Clock

The clock used by Erker et al. [16] in their work is based on a minimal model of a quantum heat engine first proposed in [21]. We will briefly discuss the fundamental functionality of this system here and refer to the two aforementioned publications for a thorough analysis. The idea is to use two thermal baths at different temperatures as an resource to drive a load. If the evolution of the load is periodic it can be used as a pointer that drives the register, i.e. the hands of the clock as illustrated in Figure 1.1. The heat engine is called *quantum*, as the ladder itself and the coupling to the heat baths is realized using quantum systems. The two baths at temperatures T_c and T_h are connected to two qubits with energy spacing E_c and E_h respectively. We define the temperatures such that $T_c < T_h$ and demand $E_c < E_h$ of the energy spacings. These two qubits form a four dimensional product Hilbert space in which population transfer is driven by the thermal baths, as depicted in Figure 1.1. We define two of the four states as a sub-Hilbert space called the *virtual qubit* which has an energy spacing of $E_w = E_h - E_c$. At equilibrium with the baths the population ratios of the two real qubits are

$$\frac{p^{\mathrm{e}}_{\mathrm{c,h}}}{p^{\mathrm{g}}_{\mathrm{c,h}}} = e^{-\beta_{\mathrm{c,h}} E_{\mathrm{c,h}}} , \tag{1.1}$$

where $p^{\mathrm{g}}_{\mathrm{c}}$ ($p^{\mathrm{e}}_{\mathrm{c}}$) and $p^{\mathrm{g}}_{\mathrm{h}}$ ($p^{\mathrm{e}}_{\mathrm{h}}$) are the populations of the cold and hot ground (excited) qubit states respectively and $\beta_{\mathrm{c,h}} = 1/k_{\mathrm{B}} T_{\mathrm{c,h}}$ are the inverse temperatures. We define a virtual temperature T_{v} through the population ratio of the virtual qubit

$$\frac{p^{\mathrm{e}}_{\mathrm{v}}}{p^{\mathrm{g}}_{\mathrm{v}}} = e^{-\beta_{\mathrm{v}} E_{\mathrm{w}}} , \tag{1.2}$$

with $\beta_{\mathrm{v}} = 1/k_{\mathrm{B}} T_{\mathrm{v}}$, and find

$$k_{\mathrm{B}} T_{\mathrm{v}} = \frac{E_{\mathrm{h}} - E_{\mathrm{c}}}{\beta_{\mathrm{h}} E_{\mathrm{h}} - \beta_{\mathrm{c}} E_{\mathrm{c}}} \tag{1.3}$$

by using $p^{\mathrm{g}}_{\mathrm{v}} = p^{\mathrm{g}}_{\mathrm{h}} p^{\mathrm{e}}_{\mathrm{c}}$ and $p^{\mathrm{e}}_{\mathrm{v}} = p^{\mathrm{e}}_{\mathrm{h}} p^{\mathrm{g}}_{\mathrm{c}}$. The virtual temperature can therefore be positive and negative. A negative temperature corresponds to a population inversion of the virtual qubit. The virtual qubit is additionally coupled to a load, namely an energy ladder, a system consisting of d levels with equal spacing E_{w}. If the virtual qubit is at a negative temperature, energy can be transferred to the ladder by jumping from state n to $n+1$. The ladder system is chosen such that the highest lying level is coupled to the lowest level, therefore the population can decay once the highest level has been reached, emitting a photon of energy $E_\gamma = (d-1)E_{\mathrm{w}}$. This decay renders the climbing of the ladder to be periodic as long as the energy transfer from the virtual qubit happens at a constant rate. The emitted photon is now used as a *tick* of the clock which can be detected by the register to advance the hands of the clock. The imperfection of the clock comes into play as the evolution of the ladder is not deterministic and the ladder is climbed only approximately at a constant rate. The objective is now to investigate the stability of this clock in terms of the amount of heat that is "wasted" into the cold bath, i.e. the amount of entropy increase that is caused by the clock.

1.1.2. The Result

First, we introduce the way clock performance is quantified by Erker et al. The two figures of merit are resolution and accuracy. The resolution ν_{tick} is the number of ticks the clock provides per unit time. The accuracy N is the number of ticks after which the uncertainty of a tick equals the time between two ticks. If we assume the times between ticks to be independently and identically distributed, the uncertainty of a tick after n ticks is just $\sqrt{n}\Delta t_{\mathrm{tick}}$ where Δt_{tick} is the uncertainty of a single tick and N becomes

$$N = \left(\frac{t_{\mathrm{tick}}}{\Delta t_{\mathrm{tick}}} \right)^2 . \tag{1.4}$$

Erker et al. now perform a numerical simulation of the system and find interesting behavior of these two quantities in dependence of the heat Q_c dissipated into the cold

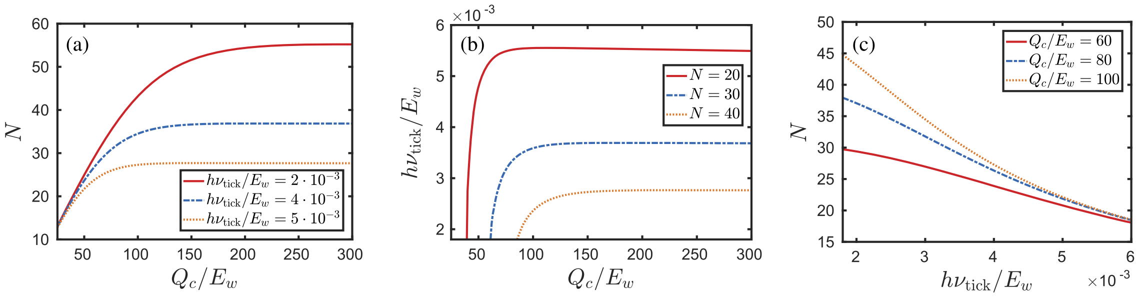

Figure 1.2.: Results of the numerical simulations taken from [16]. (a) Accuracy N over heat dissipated to the the cold bath Q_c for different resolutions. (b) Resolution over Q_c for different accuracies. Both cases show a similar behavior, accuracy and resolution first increase with Q_c before saturating at a constant value. (c) Trade-off between accuracy and resolution. For a fixed amount of Q_c, increasing N will lead to a decrease in resolution and vice-versa. Higher Q_c will lead to higher values for both accuracy and resolution if it is below the saturation threshold.

bath, the results of which are depicted in Figure 1.2. They found that both accuracy and resolution increase for small values of Q_c before saturating at a constant level. Also, there exists a trade-off between accuracy and resolution. For a fixed amount of heat Q_c increasing the accuracy will lead to a decrease in resolution and vice-versa. In order to increase both of these values at the same time, again Q_c needs to be increased. This leads us directly to the conclusion of these simulations: Entropy, here equivalent to the heat dissipated into the cold bath, is a resource needed for time measurement. Obviously, these results are obtained for a specific system and on first sight it is unclear if the connection between entropy and time keeping is universal. Erker et al. however argue that it is. The crucial aspect is the irreversibility of the pointer evolution. In order to get continuous ticks, the periodic evolution of the pointer must be more probable in one direction then its time inverse. An out-of-equilibrium resource must therefore supply free energy to the pointer for continuous operation. As this is not possible with unit efficiency, the total entropy of the system must be increased.

1.2. The Phonon Laser Clock

So far, the aforementioned connection between thermodynamics and timekeeping has only been tested theoretically for a specific system. The motivation for this thesis is to test it in an experiment and also to choose a completely different system to test the conjectured universality of the findings described above. Following the requirements established in [16], we require a system for which interaction with the environment is well characterized to ensure fair bookkeeping of the heat and energy flow and therefore of the entropy increase. We want to use the system as a clock and evidently need a periodic signal which can be detected. Finally, one of the most important requirements is the efficiency of the system. At least for the system discussed above, the connection between heat and clock quality can only be observed for low heat dissipation and most real-life clocks require power input for sustained operation which is orders of magnitude

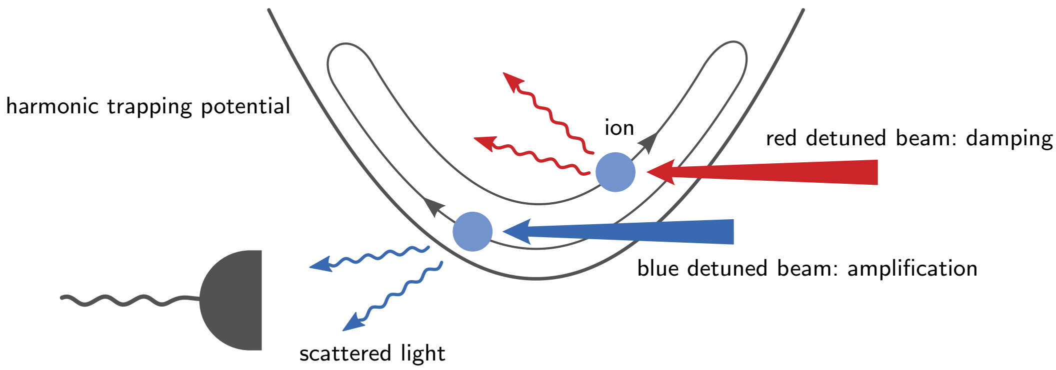

Figure 1.3.: Sketch of the ion oscillator. A single ion is trapped in a harmonic potential. A red detuned laser reduces the momentum of the ion and thus damps is motion, while a blue detuned laser amplifies it. The beams are in resonance with the ion at different points of the oscillation cycle due to the different frequency detunings and the Doppler shift. For well chosen combinations of laser intensities, the oscillation will reach a steady state amplitude. Photons are scattered by the ion with the same periodicity as the oscillation. This can be user to detect the oscillation phase.

higher then the minimal requirement for a microscopic clock proposed by Erker et al. Consequently, we require a system that efficiently converts energy into clock ticks.

We propose that an ion in a harmonic potential, which experiences oscillation-phase dependent damping and amplification forces for sustained oscillation as sketched in Figure 1.3, is a suitable candidate for such an experimental test. This system is realized with a $^{40}Ca^{+}$ ion in a Paul trap, illuminated by laser beams red and blue detuned from an electronic dipole transition, leading to damping and amplification of motion. A mechanical pendulum which looses some energy through friction and is in turn supplied with energy during every oscillation cycle is a suitable macroscopic analogy. This kind of self-sustained ion oscillator has been implemented by Vahala et al. [19] [2] and coined *phonon laser* due to its analogy to an optical laser [3]. We will refer to the oscillating ion as a "phonon laser" or an "ion oscillator" interchangeably in the following.

Even though this ion oscillator is quite different from the heat engine driven clock introduced in Section 1.1, it has certain properties that make it a good candidate for such a test. The first one being its simplicity: Laser-driven self-sustained oscillation is relatively simple compared to an autonomous quantum heat engine. Also the detection of the motion using the very same laser beams as for the drive, as discussed in Section 1.2.3, adds to the appeal of the experiment. One of the important differences compared to the heat engine driven clock, and to all common frequency standards, is the oscillation

[2] A related theory of a similar system was independently proposed by Kaplan [20]

[3] A threshold for the transition from thermal excitation to self-sustained oscillation and stimulated emission of phonons are the key parallels to a laser. The reader is referred to [19] for further discussion on this subject

frequency. It is fixed for the ion by the confinement in the Paul trap. However, the energy input from the lasers does not require any time dependent, external drive: The ion is continuously illuminated by the lasers and no external control determines the phase of the oscillation. Due to the stochastic recoil of the scattered photons the ion will experience momentum kicks which in turn lead to jumps in the phase. The instability of the oscillation caused by this phase noise will be the effect of interest in this thesis.

Additionally to the phase noise we need to measure the entropy production, or analogously the waste heat production, of the system in order to relate the two quantities. Our measure for waste heat is the amount of photons scattered by the ion. This is justified, as every photon absorbed from the low-entropy, coherent and monochromatic laser fields is later scattered, and thus "wasted", into a random vacuum mode.

These considerations set the path for the experiment. For different parameters of the driving laser fields the phase stability of the ion oscillation needs to be evaluated. Subsequently, connections between this stability and the amount of scattered photons can be studied, possibly enabling an experimental test of the connection between thermodynamics and time measurement.

We will discuss general considerations concerning this system in this section and leave the thorough theoretical analysis to Section 2.2.

1.2.1. The ^{40}Ca^{+}Ion

To implement the ion oscillator we use ^{40}Ca^{+} ions. A single valence electron leads to a alkaline-like level scheme of which the relevant part is depicted in Figure 1.4. Due to the short life time of the $4P_{1/2}$ state, driving of the $4S_{1/2} \leftrightarrow 4P_{1/2}$ transition will lead to a large scattering rate. We will therefore use this transition to drive the oscillation. As discussed above, two laser beams, red and blue detuned from this transition, will lead to a self-sustained oscillation of the ion due to velocity dependent radiation pressure forces as discussed in Section 2.1.1.

A magnetic field lifts the degeneracy of the magnetic substates of the $4S_{1/2}$ and $4P_{1/2}$ levels. Decay from both states of the excited $4P_{1/2}$ manifold is possible into both states of the ground state. Consequently, we can not isolate a single two-level system (TLS) using the $4S_{1/2} \leftrightarrow 4P_{1/2}$ transition. All four levels depicted in Figure 1.4(b) must be taken into account. Depending on the polarization of the beams relative to the magnetic field, different transitions are allowed. However, to simplify the analytical description, we will assume a TLS in Section 2.2 and neglect the more complex structure. For low scattering rates this is a good approximation as no level is depleted through optical pumping during a single cycle. It remains however unclear how well the approximation holds for higher scattering rates. We will propose how to realize a near-perfect TLS in Chapter 8 which could be implemented in future work.

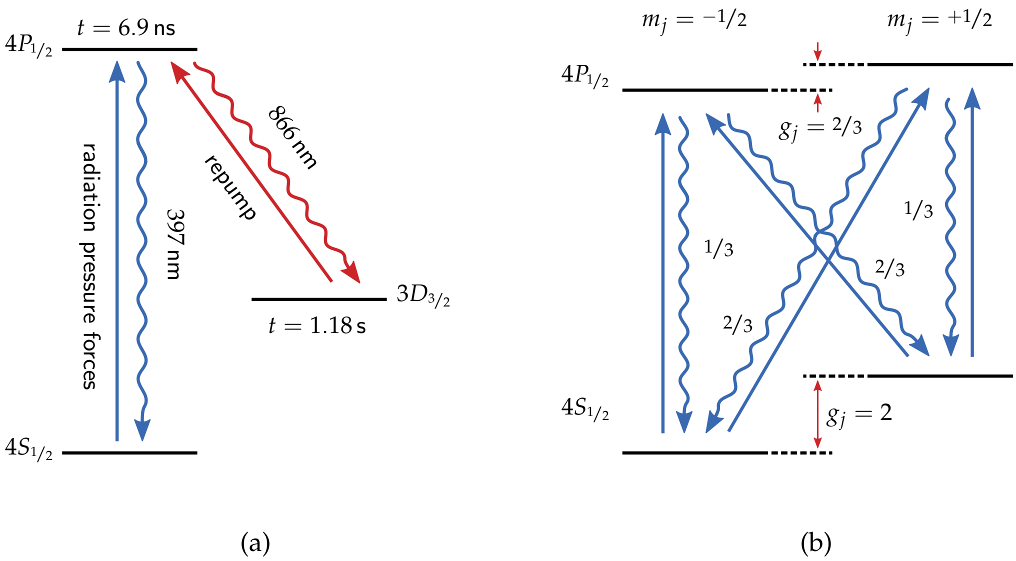

Figure 1.4.: Level scheme of the $^{40}Ca^{+}$ ion. (a) The $4S_{1/2} \leftrightarrow 4P_{1/2}$ dipole transition is used to drive the oscillation using a near 397 nm laser beam. Additional decay into the metastable $3D_{3/2}$ state needs to be taken into account and a near 866 nm beam pumps the population back into the cyclic transition. (b) The two levels used to drive the oscillation are each split due to a finite magnetic field. All transitions between the magnetic substates need to be taken into account. The fractions at the decay arrows denote the ratios at which the respective spontaneous decays take place.

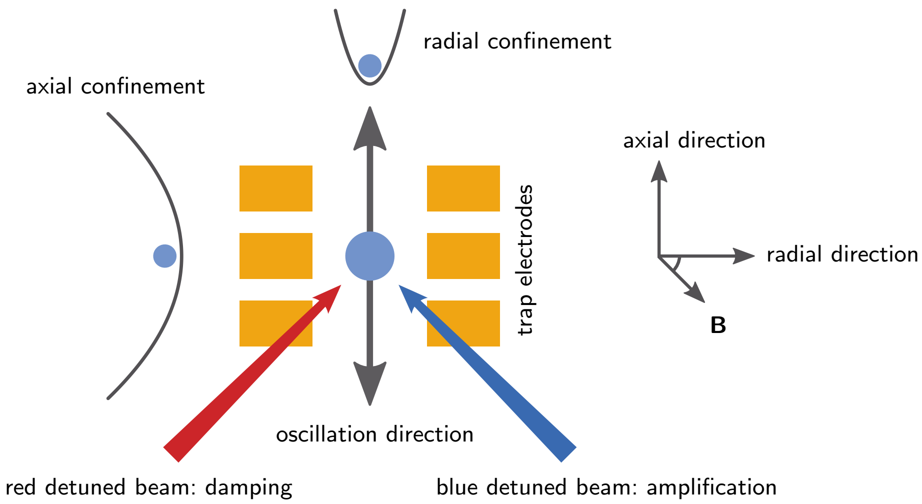

Figure 1.5.: Sketch of the oscillating ion in the trap. The confinement in the radial direction is stronger then in the axial direction. The projections of the laser beams on the axial directions have the same directions while the projections on the radial direction have opposing directions. This both leads to an axial oscillation of the ion. The magnetic field **B** encloses a angle of 45° with the trap axis which will be important later for the polarizations of the beams.

1.2.2. The Setup

A sketch of our experimental setting is shown in Figure 1.5. The ion is confined in a Paul trap and the red and blue detuned beams illuminate the ion on a 45° angle to the trap axis. The ion is confined by a harmonic potential in all spatial directions. Sustained oscillation should consequently be possible in all directions onto which the projection of the driving fields wavevectors are non-zero. In the Paul trap used in the experiments we define an axial direction, in which the confinement is of purely electrostatic nature, and two radial ones, where the confinement is of pondermotive nature. Sustained oscillation is only possible in the plane defined by the two driving beams. The direction of the laser beams will play an important role. As will be discussed in greater detail in Section 2.2.5, the scattering rate caused by the two beams varies over the oscillation cycle (of course this is the essential fact that leads to the oscillation). If the two beams are counter-propagating with respect to a given oscillation direction, the scattering will occur at similar oscillation phases due to the different detunings. If the beams are instead co-propagating with respect to the direction under consideration, the scattering can take place at distinct oscillation phases. It seems plausible that this will favor an oscillation direction for which the beams are effectively co-propagating. This will lead to an axial ion oscillation in our case which is indeed what can be observed in the measurements.

1.2.3. Detection

To detected the ion motion, and ultimately the oscillation phase stability, we exploit the periodicity of the scattered light. As the ion oscillates in the trap it changes its velocity sinusoidaly. Due to the Doppler effect the ion will therefore be in resonance with each laser twice per oscillation period. The scattering rate will consequently be modulated with the oscillation frequency. However, due to the two lasers that are being used the strongest modulation component will be at twice the oscillation frequency. As the rate of detected photons is low compared to the oscillation frequency, we can not simply detect the scattered photons and infer the position of the ion. Instead we will measure the arrival times of the photons at the detector and use a Fourier analysis of these times to compute the underlying frequency. This frequency measurement can then be used to collect frequency samples over time from which an Allan variance can be computed. The Allan variance contains information about various noise contributions to the oscillation phase and frequency and can be used to determine the phase stability of the oscillation.

2. Theory

2.1. Atom-Light Interaction

The experiments in this thesis are based on a laser-driven atomic two-level system (TLS). In this section we will give a short overview on the most simple model for the interaction between the light field and the atom. The atom is assumed to be a quantum mechanical TLS which interacts with a classical electric field. We will not go trough the full derivation but instead state the most important results and the approximations needed to derive them. For a thorough treatment of this topic the reader is referred to the standard text books of atomic physics [22]. After deriving the scattering rate of an ion, we use this result to derive the expression for the radiation pressure force which an electromagnetic wave exerts on an atom in Section 2.1.1.

The Hamiltonian of the laser-driven TLS reads

$$H = \hbar\omega_1 |1\rangle \langle 1| + \hbar\omega_2 |2\rangle \langle 2| + H_{\text{int}} \,, \tag{2.1}$$

where $|1\rangle$ and $|2\rangle$ are the energy eigenstates of the atom and $\hbar\omega_1$ and $\hbar\omega_2$ their energy eigenvalues. In the following, we will assume that $\omega_2 > \omega_1$, making $|1\rangle$ the "ground state" with lower energy and $|2\rangle$ the "excited state" with higher energy. We now need to determine the interaction term H_{int}. Classically, a dipole $e\boldsymbol{r}$ in an electric field $\boldsymbol{E}$ has the potential energy $-e\boldsymbol{r}\boldsymbol{E}$ and we therefore write

$$H_{\text{int}} = -\boldsymbol{d}\boldsymbol{E}(\hat{\boldsymbol{r}}, t) \,, \tag{2.2}$$

with the dipole operator $\boldsymbol{d} = -e\hat{\boldsymbol{r}}$, where e is the electron charge and $\hat{\boldsymbol{r}}$ the position operator. In the following, we will assume $\boldsymbol{E}(\hat{\boldsymbol{r}}, t)$ to vary negligibly over the extent of the atom by making the *dipole approximation* $\boldsymbol{E}(\hat{\boldsymbol{r}}, t) = \boldsymbol{E}(t)$. As we assume interaction with a monochromatic electromagnetic wave, we can write $\boldsymbol{E}(t) = \boldsymbol{\epsilon} E_0 \cos(\omega_{\text{L}} t)$. Using these assumptions one can show that

$$H_{\text{int}} = -\hbar\Omega \cos(\omega_{\text{L}} t)(|1\rangle \langle 2| + |2\rangle \langle 1|), \tag{2.3}$$

by introducing the *Rabi frequency*

$$\Omega = \frac{\langle 2| \boldsymbol{\epsilon} E_0 \boldsymbol{d} |1\rangle}{\hbar} \,. \tag{2.4}$$

The Rabi frequency quantifies the strength of the coupling between the atom and the electric field. By making an exponential ansatz, neglecting rapidly oscillating terms

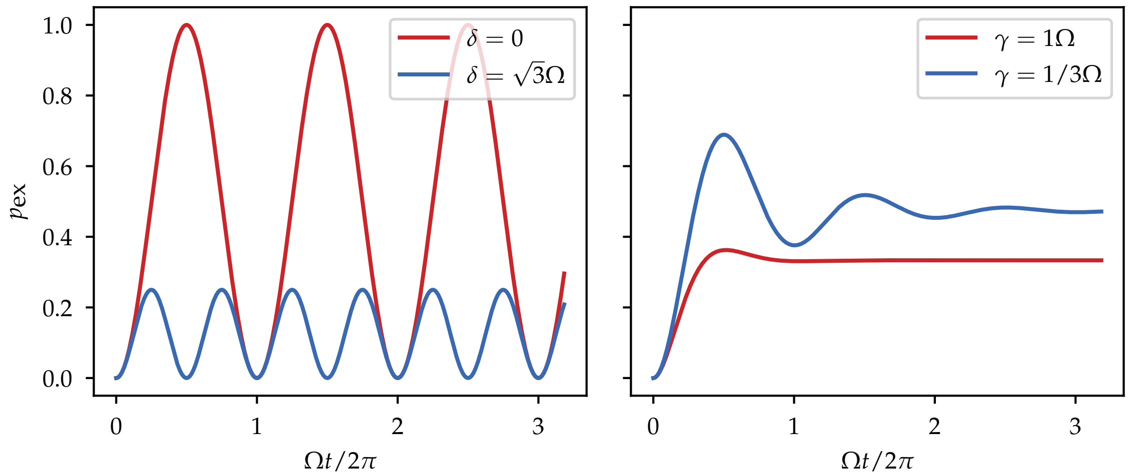

Figure 2.1.: Exited state population probability p_{ex} as a function of the pulse area Ωt. Left, without spontaneous decay for different detunings δ. Right, for two different values of the decay rate γ but with zero detuning.

(*rotating wave approximation*) and transforming into a *rotating frame* one can now solve the Schrödinger equation

$$i\hbar\frac{\partial}{\partial t}\left|\psi(t)\right\rangle = H\left|\psi(t)\right\rangle \tag{2.5}$$

and arrive at the time-dependent populations

$$\begin{aligned} p_1(t) &= \frac{1}{2}(1+\cos(\Omega t)) \\ p_2(t) &= \frac{1}{2}(1-\cos(\Omega t)) \end{aligned} \tag{2.6}$$

for the two states $|1\rangle$ and $|2\rangle$ respectively, if we choose $\delta = \omega_{\mathrm{L}} - (\omega_2 - \omega_1) = 0$ and the initial conditions $p_1(0) = 1$ and $p_2(0) = 0$. The population oscillates at the Rabi frequency. By following the same derivation for finite detuning δ one obtains the population dynamics depicted in Figure 2.1.

Spontaneous Decay

For now we have assumed an infinite lifetime for the excited state: If we would turn off the electric field at any time, the populations would remain unchanged. Taking the experimentally observed decay into account, we will assume a spontaneous decay rate γ from the excited state and represent the state of the TLS by a density matrix. The equation of motion for the density matrix ρ can be written in form of the *optical Bloch*

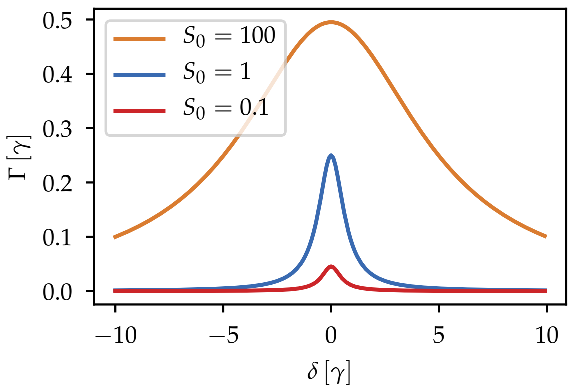

Figure 2.2.: Steady state scattering rate Γ as a function of the frequency detuning δ for different values of the resonant saturation parameter S_0 (see Equations (2.14)).

equations in the rotating frame

$$\begin{aligned}
\dot{\rho}_{11} &= \gamma\rho_{22} + i\frac{1}{2}\Omega(\rho_{21} - \rho_{12}) \\
\dot{\rho}_{22} &= -\gamma\rho_{22} + i\frac{1}{2}\Omega(\rho_{12} - \rho_{21}) \\
\dot{\rho}_{12} &= -\left(\frac{\gamma}{2} + i\delta\right)\rho_{12} + i\frac{1}{2}\Omega(\rho_{22} - \rho_{11}) \\
\dot{\rho}_{21} &= -\left(\frac{\gamma}{2} - i\delta\right)\rho_{21} + i\frac{1}{2}\Omega(\rho_{11} - \rho_{22})
\end{aligned} \tag{2.7}$$

Using the hermiticity and trace condition for the density matrix and by introducing the inversion

$$w = \rho_{22} - \rho_{11}\,, \tag{2.8}$$

one can simplify Equations (2.7) to

$$\begin{aligned}
\dot{\rho}_{21} &= -\left(\frac{\gamma}{2} - i\delta\right)\rho_{21} + i\frac{1}{2}\Omega(\rho_{11} - \rho_{22}) \\
\dot{w} &= -\gamma(w+1) - i\Omega(\rho_{21} - \rho_{12})\,,
\end{aligned} \tag{2.9}$$

which leads to decaying Rabi oscillations as depicted in Figure 2.1.

Steady State Solution and Scattering Rate

One can now solve Equations (2.9) for the steady state case $\dot{w} = 0$ and $\dot{\rho}_{21} = 0$. For a decay rate γ this state will be reached for times $t \gg 1/\gamma$. One obtains the simple expression

$$w = -\frac{1}{1+S} \tag{2.10}$$

for the inversion, using the saturation parameter

$$S = \frac{2\Omega^2}{\gamma^2 + 4\delta^2} \tag{2.11}$$

which has a very intuitive meaning: For $S \ll 1$ the atom will be mainly in the ground state, for $S \gg 1$ the inversion is approximately zero and both states become equally populated. In experiments, the inversion can not be measured directly, instead the rate Γ at which photons are spontaneously scattered from the atom is more easily accessible. Clearly, Γ must be the decay rate times the probability to be in the excited state:

$$p^{\mathrm{ex}} = \rho_{22} = \frac{1}{2}(1+w) = \frac{S}{2(1+S)} = \frac{1}{2}\frac{S_0}{1+S_0+4\,{}^{\delta^2}/_{\gamma^2}}\,, \tag{2.12}$$

using the resonant saturation parameter

$$S_0 = \frac{2\Omega^2}{\gamma^2}\,, \tag{2.13}$$

leads us to

$$\begin{aligned} \Gamma &= \gamma p^{\mathrm{ex}} \\ &= \frac{\gamma}{2}\frac{S_0}{1+S_0+4\,{}^{\delta^2}/_{\gamma^2}} \\ &= \gamma\frac{\Omega^2}{4\delta^2+2\Omega^2+\gamma^2}\,. \end{aligned} \tag{2.14}$$

Therefore the scattering rate is a Lorentzian when viewed as a function of δ with a full width at half maximum (FWHM) of $\sqrt{\gamma^2 + 2\Omega^2}$ as depicted in Figure 2.2. For small light intensities, and thus small Ω and S_0, the line will take the FWHM of γ, explaining the alternative term *natural linewidth* for the decay rate γ. For increasing Ω the line will broaden (Figure 2.2), an effect called saturation broadening. Also we note, that the scattering rate has an upper bound of $\gamma/2$.

2.1.1. Light Pressure

If an atom absorbs a photon while undergoing an internal transition, as described in the previous section, momentum is transferred from the photon to the atom. As the photon with wavevector $\mathbf{k}$ has momentum $\hbar\mathbf{k}$, momentum conservation dictates that this momentum must be transferred to the atom. On the other hand, momentum is again transferred back to a photon if a spontaneous scattering event occurs. The modulus of these two momentum transfers is equal, although their directions are not. The momentum transferred to the atom for an absorption always has the direction of the wavevector while the spontaneously scattered photon is emitted into a random direction. The momentum transfer from the ion to the light field therefore averages to zero over time. Consequently, for a scattering rate Γ an average force of

$$\mathbf{F} = \hbar\mathbf{k}\Gamma \tag{2.15}$$

will be exerted on the atom.

As shown above, the scattering rate depends on the detuning δ of the light frequency from the resonant transition frequency. Furthermore, the effective detuning depends on the atom velocity v through the Doppler effect. If the atom velocity is anti-parallel to the wavevector, the effective detuning is shifted by $\mathbf{kv}$ to higher values while parallel velocity has the opposite effect. The scattering rate Γ in Equations (2.14) will consequently take the form

$$\Gamma = \frac{\gamma}{2}\frac{S_0}{1 + S_0 + 4(\delta - kv)^2/\gamma^2}, \tag{2.16}$$

for finite velocity with modulus v and the projection of the wavevector onto the direction of motion k. If the detuning is now shifted from the atomic resonance in the laboratory frame, we can influence if the force on the atom will increase or decrease the modulus of its momentum. If the rest frame frequency is red detuned ($\delta < 0$) the atom is in resonance with the light field if it moves towards it and will experience a force opposite to its momentum, hence slowing it down. If the rest frame frequency is blue detuned ($\delta > 0$) the case is analogous but opposite and the atom velocity is increased. This effect can be used, to cool down thermally excited atoms with a red detuned laser beam [23, 24]. In the experiments presented in this thesis, we will also use the opposite effect of a blue detuned laser which increases the kinetic energy of the atom.

2.2. Theoretical Analysis of the Ion Oscillator

In this section a theoretical model for the ion motion subject to trap potential and light field interactions, i.e. for the phonon laser, will be established. This model was developed in collaboration with Nahuel Freitas during joined work on the subject. It is similar to the theory in [19] but also includes the oscillation phase and its stability. The general case of a harmonic oscillator subject to velocity dependent and Langevin forces will be discussed first. Subsequently, these results will be specifically evaluated and discussed for the concrete system of an ion subject to light forces caused by frequency detuned laser beams.

2.2.1. Equations of Motion, The General Case

In this section the equations of motion governing the ion motion in the trap will be established and solved for a relatively general case, i.e. without using explicit expressions for the relevant forces. Additionally to the harmonic forces of the trap potential, nonlinear forces due to the laser field and stochastic forces due to spontaneous scattering need to be taken into account. This leads to the need of stochastic calculus, i.e. Itôs calculus [25], of which the main results will be used in the following without discussing them in great detail.

In general, the differential equation describing the ions position x over time assumes the following form

$$\ddot{x} + \nu(\dot{x}) + \omega^2 x = \lambda(\dot{x})\chi(t). \tag{2.17}$$

ν describes the light forces, which depend on the effective detuning from an electronic transition and thus on the velocity $\dot{x}$ trough the Doppler shift. $\lambda(\dot{x})\chi(t)$ describes the white noise contribution due to spontaneous scattering. $\chi(t)$ is a white noise Langevin force with zero correlation time $\langle\chi(t)\chi(t')\rangle = \delta(t-t')$ and $\lambda(\dot{x})$ its velocity dependent amplitude. Finally, the confinement in the harmonic potential is included via the trapping frequency ω.

As the ion will be approximately describing a sinusoidal motion, and phase and amplitude are the quantities of interest, it makes sense to transform into different coordinates:

$$\begin{aligned} x &= A\sin(\omega t + \phi) \\ v &= A\omega\cos(\omega t + \phi)\,, \end{aligned} \tag{2.18}$$

where we have defined the velocity $v = \dot{x}$, or equivalently

$$\begin{aligned} A &= \sqrt{x^2 + (v/\omega)^2} \\ \phi &= \arctan\left(\omega x/v\right) - \omega t\,. \end{aligned} \tag{2.19}$$

Writing Equation (2.17) as a system of first order differential equations in differential form leads to

$$\begin{aligned} \mathrm{d}x &= v\mathrm{d}t \\ \mathrm{d}v &= (-\nu(v) - \omega^2 x)\mathrm{d}t + \lambda(v)\mathrm{d}W\,, \end{aligned} \tag{2.20}$$

where $\mathrm{d}W = \mathrm{d}\chi\mathrm{d}t$ is the differential of uncorrelated white noise [1]. As this is a system of stochastic differential equations, the transformation to the new coordinates Equations (2.19) needs to be done according to the rules of stochastic calculus. Following Itôs formula we get

$$\begin{aligned} \mathrm{d}A = &\frac{\partial A}{\partial t}\mathrm{d}t + \frac{\partial A}{\partial x}\mathrm{d}x + \frac{\partial A}{\partial v}\mathrm{d}v \\ &+ \frac{1}{2}\frac{\partial^2 A}{\partial t^2}\mathrm{d}t^2 + \frac{1}{2}\frac{\partial^2 A}{\partial x^2}\mathrm{d}x^2 + \frac{1}{2}\frac{\partial^2 A}{\partial v^2}\mathrm{d}v^2 \\ &+ \frac{1}{2}\frac{\partial^2 A}{\partial t \partial x}\mathrm{d}t\mathrm{d}x + \frac{1}{2}\frac{\partial^2 A}{\partial t \partial v}\mathrm{d}t\mathrm{d}v + \frac{1}{2}\frac{\partial^2 A}{\partial x \partial v}\mathrm{d}x\mathrm{d}v \end{aligned} \tag{2.21}$$

Note that A, contrary to ϕ, does not explicitly depends on t and partial derivatives with respect to t in Equation (2.21) will vanish. Terms proportional to $\mathrm{d}t^2$ or $\mathrm{d}t\mathrm{d}W$ vanish when we integrate over Equation (2.21) and can therefore be dropped in the following. However, one of the important result of Itô calculus is that $\mathrm{d}W^2 = \mathrm{d}t$. Consequently, contrary to regular calculus, the terms containing $\mathrm{d}x^2$ and $\mathrm{d}v^2$ do not vanish. By then explicitly computing the partial derivatives of A and ϕ using Equations (2.19) and plugging Equations (2.20) and Equations (2.18) into Equation (2.21) we get

$$\begin{aligned} \mathrm{d}A &= \left[\frac{\lambda^2(v)}{2A\omega^2}\sin(\omega t + \phi)^2 - \frac{1}{\omega}\cos(\omega t + \phi)\nu(v)\right]\mathrm{d}t + \frac{\lambda(v)}{\omega}\cos(\omega t + \phi)\mathrm{d}W \\ \mathrm{d}\phi &= \left[\frac{\lambda^2(v)}{A^2\omega^2}\cos(\omega t + \phi)\sin(\omega t + \phi) + \frac{1}{A\omega}\sin(\omega t + \phi)\nu(v)\right]\mathrm{d}t - \frac{\lambda(v)}{A\omega}\sin(\omega t + \phi)\mathrm{d}W, \end{aligned} \tag{2.22}$$

using an analogous approach for $\mathrm{d}\phi$ and $v = v(A, \phi) = A\omega\cos(\omega t + \phi)$. These equations are completely general and do not involve any approximations. They are, however, too complex to find an analytical solution. Therefore reasonable approximations will be made in the following, for which solving of the equations becomes possible.

Small Noise Expansion

One approximation that can be made and that simplifies Equations (2.22) significantly is to assume a small noise contribution. By assuming a noise intensity proportional to ϵ and expanding A and ϕ in powers of ϵ, one can develop a perturbative theory for solving Equations (2.22). For small ϵ terms of higher order can than be neglected, leading to an

[1] Note that strictly speaking the differential $\mathrm{d}W$ only makes sense in an integral as $\chi(t)$ is nowhere differentiable. All differential equations that are used here need to be understood as the differential form of integral equations

approximated set of stochastic differential equations. First, we write Equations (2.22) as

$$\begin{aligned} \mathrm{d}A &= a(A,\phi)\mathrm{d}t + \epsilon b(A,\phi)\mathrm{d}W + \mathcal{O}(\epsilon^2) \\ \mathrm{d}\phi &= c(A,\phi)\mathrm{d}t + \epsilon d(A,\phi)\mathrm{d}W + \mathcal{O}(\epsilon^2) \end{aligned} \tag{2.23}$$

using

$$\begin{aligned} a(A,\phi) &= -\frac{1}{\omega}\cos(\omega t+\phi)\nu(A\omega\cos(\omega t+\phi)) \\ b(A,\phi) &= \frac{1}{\omega}\cos(\omega t+\phi)\lambda(A\omega\cos(\omega t+\phi)) \\ c(A,\phi) &= \frac{1}{A\omega}\sin(\omega t+\phi)\nu(A\omega\cos(\omega t+\phi)) \\ d(A,\phi) &= -\frac{1}{A\omega}\sin(\omega t+\phi)\lambda(A\omega\cos(\omega t+\phi)) \end{aligned} \tag{2.24}$$

Following the method presented in [25] it is assumed that following expansions in ϵ can be made:

$$\begin{aligned} A(t) &= \sum_{n=0}^{\infty}\epsilon^n A_n(t) \\ \phi(t) &= \sum_{n=0}^{\infty}\epsilon^n \phi_n(t) \end{aligned} \tag{2.25}$$

$$a(A,\phi) = a\left(\sum_{n=0}^{\infty}\epsilon^n A_n(t), \sum_{n=0}^{\infty}\epsilon^n \phi_n(t)\right) \tag{2.26}$$

$$= a_0(A_0,\phi_0) + \epsilon a_1(A_0,A_1,\phi_0,\phi_1) + \epsilon^2 a_2(A_0,A_1,A_2,\phi_0,\phi_1,\phi_2) + \dots \tag{2.27}$$

The expansion for b, c and d are carried out analogously. Equation (2.27) follows by doing a Taylor expansion around (A_0,ϕ_0) and sorting by powers of ϵ. This also yields explicit expressions for the a_n, namely for the first two terms

$$\begin{aligned} a_0(A_0,\phi_0) &= a(A_0,\phi_0) \\ a_1(A_0,A_1,\phi_0,\phi_1) &= \frac{\partial a(A_0,\phi_0)}{\partial A_0}A_1 + \frac{\partial a(A_0,\phi_0)}{\partial \phi_0}\phi_1 \end{aligned} \tag{2.28}$$

Plugging in Equations (2.25) and Equation (2.27) into Equations (2.23) and equating terms pertaining to identical powers of ϵ yields a system of equations for the different components A_n and ϕ_n:

$$\begin{aligned} \mathrm{d}A_0 &= a(A_0,\phi_0)\mathrm{d}t \\ \mathrm{d}\phi_0 &= c(A_0,\phi_0)\mathrm{d}t \end{aligned} \tag{2.29}$$

$$\begin{aligned} \mathrm{d}A_1 &= \left(\frac{\partial a(A_0,\phi_0)}{\partial A_0}A_1 + \frac{\partial a(A_0,\phi_0)}{\partial \phi_0}\phi_1\right)\mathrm{d}t + b(A_0,\phi_0)\mathrm{d}W \\ \mathrm{d}\phi_1 &= \left(\frac{\partial c(A_0,\phi_0)}{\partial A_0}A_1 + \frac{\partial c(A_0,\phi_0)}{\partial \phi_0}\phi_1\right)\mathrm{d}t + d(A_0,\phi_0)\mathrm{d}W \end{aligned} \tag{2.30}$$

Hence, A_0 and ϕ_0 are just the unperturbed solutions not including any noise. The advantage that has been gained here is that the equations can be solved sequentially. Equations (2.29) can be solved by means of standard calculus. Using the resulting functions $A_0(t)$ and $\phi_0(t)$, Equations (2.30) can then be solved using stochastic calculus. This is now possible as the coefficients of $\mathrm{d}W$ depend on time exclusively, contrary to the original Equations (2.22) where they depended on the functions $A(t)$ and $\phi(t)$.

Adiabatic Approximation and Timescale Separation

Even using the approximations introduced above analytical solutions for amplitude and phase, or rather statistics like mean and variance, are still beyond reach. Separating timescales of different quantities in the equations using an adiabatic approximation further simplifies the evaluation. The important assumption to be made is that phase and amplitude vary on much slower timescales then a period of the oscillation, i.e. $\dot{A}/A \ll \omega$ and $\dot{\phi} \ll \omega$. This enables the evaluation of the coarse grained evolution of $A(t)$ and $\phi(t)$ to lower order in this adiabatic limit. First, the solution of $A_0(t)$ will be considered. Integrating Equations (2.29) over one oscillation period $\tau = 2\pi/\omega$ yields

$$\begin{aligned} A_0(t+\tau) - A_0(t) &= \int_t^{t+\tau} \mathrm{d}t' a(A_0(t'), \phi_0(t')) \\ &= -\frac{1}{\omega}\int_t^{t+\tau} \mathrm{d}t' \cos(\omega t' + \phi_0(t'))\nu(A_0(t')\omega\cos(\omega t' + \phi_0(t'))) \\ &\approx -\frac{1}{\omega}\int_t^{t+\tau} \mathrm{d}t' \cos(\omega t' + \phi_0(t))\nu(A_0(t)\omega\cos(\omega t' + \phi_0(t))) \\ &= -\frac{1}{\omega}\int_t^{t+\tau} \mathrm{d}t' \cos(\omega t')\nu(A_0(t)\omega\cos(\omega t')) \end{aligned} \tag{2.31}$$

where the adiabatic approximation has been introduced in the third line by replacing $A_0(t') \to A_0(t)$ and $\phi_0(t') \to \phi_0(t)$ in the integral. The integrand is periodic with respect to τ and the $\phi_0(t)$ terms can therefore be omitted in the third line. A differential equation for A_0 is required, so the equation above is rewritten in a way that gives a coarse grained approximation to the time derivative of A_0

$$\begin{aligned} \dot{A}_0 \approx \frac{A_0(t+\tau) - A_0(t)}{\tau} &\approx -\frac{1}{2\pi}\int_t^{t+\tau} \mathrm{d}t' \cos(\omega t')\nu(A_0(t)\omega\cos(\omega t')) \\ &= -\frac{1}{2\pi\omega}\int_0^{2\pi} \mathrm{d}\theta \cos(\theta)\nu(A_0(t)\omega\cos(\theta)) \\ &= -\frac{A_0(t)}{2\pi}\int_0^{2\pi} \mathrm{d}\theta \sin^2(\theta)\nu'(A_0(t)\omega\cos(\theta)) \end{aligned} \tag{2.32}$$

The second line follows from the transform $\theta = \omega t'$ and the third using integration by parts [2]. $\nu' = \frac{\mathrm{d}\nu}{\mathrm{d}v}$ is the derivative of ν. A first order integro-differential equation in A_0,

[2] There is no particular reason why one should use the form in the third line rather than the one in the second. Later on, however, we will use it to be consistent with the notation of [19].

independent of ϕ_0, has thus been obtained:

$$\dot{A}_0 = -\frac{A_0}{2}\bar{\nu}(A_0) \tag{2.33}$$

$\bar{\nu}$ is a damping or gain coefficient, "averaged" over one oscillation cycle

$$\bar{\nu}(A_0) = -\frac{1}{\pi}\int_0^{2\pi} \mathrm{d}\theta \sin^2(\theta)\nu'(A_0(t)\omega\cos(\theta)) \tag{2.34}$$

Proceeding analogously for ϕ_0 by integrating Equations (2.29), we obtain that to zeroth order in the small noise expansion and the adiabatic approximation $\phi_0(t+\tau) - \phi_0(t) = 0$[3] which of course makes sense intuitively as the phase should remain constant for zero noise. To analyze the phase stability we will go to first order in the small noise approximation but remain in the lowest order of the adiabatic approximation. By integrating Equations (2.30) for ϕ_1 and using $\phi_0(t) = \phi_0$ we find that

$$\begin{aligned}
\phi_1(t+\tau) - \phi_1(t) \approx & \frac{\phi_1(t)}{A_0(t)\omega}\int_t^{t+\tau} \mathrm{d}t'\, \nu(\omega A_0\cos(\omega t' + \phi_0))\cos(\omega t' + \phi_0) \\
& - \phi_1(t)\int_t^{t+\tau} \mathrm{d}t'\, \nu'(\omega A_0\cos(\omega t' + \phi_0))\sin^2(\omega t' + \phi_0) \qquad (2.35) \\
& - \frac{1}{A_0(t)\omega}\int_t^{t+\tau} \mathrm{d}W(t')\, \lambda(\omega A_0\cos(\omega t' + \phi_0))\sin(\omega t' + \phi_0) \\
& = -\frac{1}{A_0(t)\omega^2}\int_0^{2\pi} \mathrm{d}W(\theta)\, \lambda(\omega A_0\cos(\theta))\sin(\theta) \qquad (2.36)
\end{aligned}$$

Again, the terms containing A_1 vanish due to symmetry reasons and the first two lines cancel each other which can be easily seen by integrating the second line by parts. We now have an expression for the phase increment over one oscillation period $\phi_1(t+\tau) - \phi_1(t)$ which is purely stochastic and of which the mean and variance can be evaluated. The fact that the integral is purely stochastic directly leads to the conclusion, that the mean must vanish

$$\langle \phi_1(t+\tau) - \phi_1(t) \rangle = 0. \tag{2.37}$$

Further, since $\phi_1(t+\tau) - \phi_1(t)$ does not depend on $\phi_1(t)$ it follows that $\langle \phi_1(t+\tau)\phi_1(t)\rangle = 0$. By squaring Equation (2.36) and taking the mean we then arrive at [4]

$$\Delta\sigma_\phi^2 := \langle \phi^2(t+\tau)\rangle - \langle \phi^2(t)\rangle = \frac{1}{A_0^2\omega^3}\int_0^{2\pi} \mathrm{d}\theta \lambda^2(\omega A_0\cos(\theta))\sin^2(\theta) \tag{2.38}$$

Where $\Delta\sigma_\phi^2$ is defined as the increase in phase variance over one period. Starting with a perfectly defined phase at $t = 0$, we then obtain the phase variance after n oscillation cycles

$$\langle \phi^2(n\tau)\rangle = 2D_\phi n\tau \tag{2.39}$$

[3] It can be easily seen, that the integral vanishes due to symmetry reasons.

[4] We use the result of Itôs calculus: $\langle (\int \mathrm{d}W(s)\, g(s))^2\rangle = \int \mathrm{d}s\, g^2(s)$ for a Wiener process $W(s)$.

with the phase diffusion coefficient

$$D_\phi = \frac{\Delta\sigma_\phi^2}{2\tau} = \frac{1}{4\pi}\frac{1}{A_0^2\omega^2}\int_0^{2\pi} \mathrm{d}\theta \lambda^2(\omega A_0 \cos(\theta)) \sin^2(\theta) \tag{2.40}$$

2.2.2. Explicit Expressions for the Light Forces

So far, we have analyzed the equation of motion for a nonlinear, dissipative oscillator using the general expressions $\lambda(v)$ and $\nu(v)$ for the Langevin force due to spontaneous scattering and the deterministic forces due to light pressure. Now, we want to find explicit forms for these for the case of an ion in an harmonic trap, subject to two laser beams blue and red detuned from an electronic dipole transition. Here, we will consider the case of an ideal two level system. The red detuned laser will decelerate the ions motion, leading to a ν that is negative for negative v (hence leading to force in positive x-direction). Analogously, the blue detuned laser will act in an opposite manner (see Section 2.1.1 for a discussion on radiation pressure forces). The damping and amplification forces caused by these two laser fields will therefore counteract each other. In the following we will see in which cases they cancel and a stable oscillation is possible.

Using Equations (2.14), assuming a small resonant saturation parameter $S_0 \ll 1$ and taking the Doppler shift into account yields the scattering rates

$$R_j(v) = \frac{\gamma}{2} \frac{S_j}{1 + (2\delta_j/\gamma - 2kv/\gamma)^2} \tag{2.41}$$

for the cooling ($j = c$) and amplification ($j = a$) laser. k is the projection of the wavevector onto the axis of motion, v the ion velocity, $\delta_{a,c}$ the detunings from resonance and $S_{a,c}$ the resonant saturation parameters of the two beams. As described in Section 2.1.1, the absorption of photons by the ion from the light field leads to a net force of

$$F_j(v) = \hbar k R_j(v)\,, \tag{2.42}$$

which yields the velocity dependent, deterministic term in Equation (2.17)

$$\nu(v) = -\frac{\hbar k}{m}\left[R_c(v) + R_a(v)\right]\,. \tag{2.43}$$

The interaction with the light field will lead not only to deterministic forces for each photon absorption but also to stochastic ones due to spontaneous scattering. Spontaneous scattered photons are emitted in random directions and at random times, yielding a white noise Langevin force with intensity λ. Each scattered photon will lead to a change in velocity of $\hbar k/m$. As the photons are emitted uniformly in all directions, the effective change in velocity per photon will have zero mean and the variance $(\hbar k/m)^2$. Using the geometric factor z that describes the projection of the photon emissions onto the axis of oscillations we obtain

$$\lambda^2(v) = z\left(\frac{\hbar k}{m}\right)^2 \left[R_c(v) + R_a(v)\right]\,. \tag{2.44}$$

To follow the notation established in [19], we introduce the functions

$$\begin{aligned} \kappa(v) &= -\frac{1}{mS_c}\frac{\mathrm{d}F_c(v)}{\mathrm{d}v} \\ g(v) &= \frac{1}{mS_a}\frac{\mathrm{d}F_a(v)}{\mathrm{d}v} \end{aligned} \tag{2.45}$$

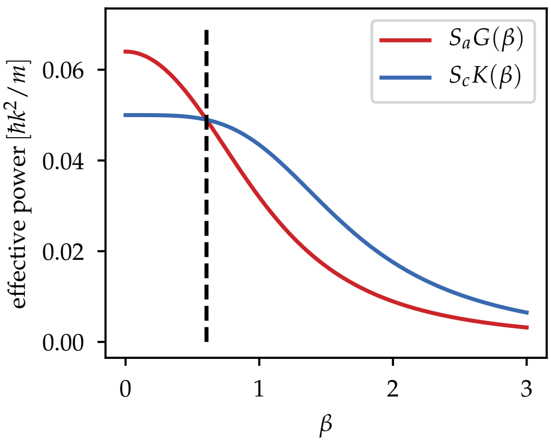

Figure 2.3.: Effective powers of cooling and amplification beams (see Equation (2.47) and Equation (2.49)) over the dimensionless amplitude β for $S_a = S_c = 0.1$, $\alpha_c = -1$, $\alpha_c = 0.5$. The intersection of the two curves corresponds to the steady state oscillation amplitude β_{OP} (dashed line).

and the cycle averaged versions

$$\begin{aligned} G(v) &= \frac{1}{\pi}\int_0^{2\pi} d\theta\, g(v\cos(\theta))\sin^2(\theta) \\ K(v) &= \frac{1}{\pi}\int_0^{2\pi} d\theta\, k(v\cos(\theta))\sin^2(\theta)\,, \end{aligned} \tag{2.46}$$

with which the deterministic part of the equation of motion for the oscillation amplitude becomes

$$\dot{A}_0 = \frac{1}{2}A_0\left[S_aG(\omega A_0) - S_cK(\omega A_0)\right]\,. \tag{2.47}$$

Analytical solutions of the integrals in Equation (2.46) can be calculated and are discussed in appendix A. Also we can write the phase diffusion coefficient by using Equation (2.44) in Equation (2.40), as

$$\begin{aligned} D_\phi &= \frac{\Delta\sigma_\phi^2}{2\tau} \\ &= \frac{z}{4\pi}\left(\frac{\hbar k/m}{\omega A_0}\right)^2\int_0^{2\pi} d\theta\,\left[R_c(\omega A_0\cos(\theta)) + R_a(\omega A_0\cos(\theta))\right]\sin^2(\theta) \end{aligned} \tag{2.48}$$

2.2.3. Operating Point

We will first look at the behavior of the steady state solution for the the oscillation amplitude to gain insight on the stability and the amplitude of the oscillation in dependence of the operation parameters S_a, S_c, δ_a, δ_c. For a steady state oscillation, i.e. $\dot{A}_0 = 0$,

$$\vartheta \equiv S_aG(\omega A_0) - S_cK(\omega A_0) = 0 \tag{2.49}$$

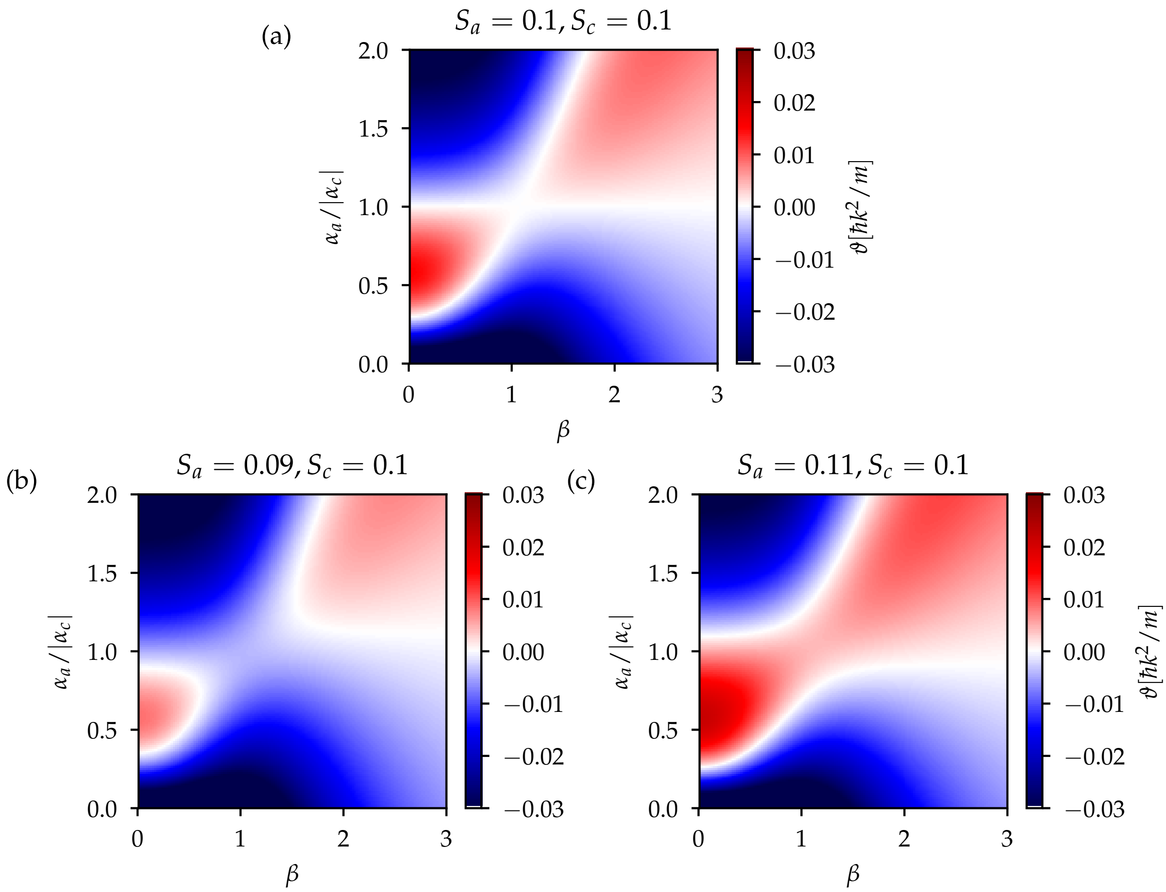

Figure 2.4.: ϑ as a function of the amplification detuning α_a and the velocity amplitude β for different saturation parameter ratios. $\alpha_c = -1$ for all cases. Positive ϑ means net amplification and negative ϑ net damping of the oscillation amplitude. Stable steady state amplitudes are those for which $\vartheta = 0$ (white lines) and $\partial\vartheta/\partial\beta < 0$.

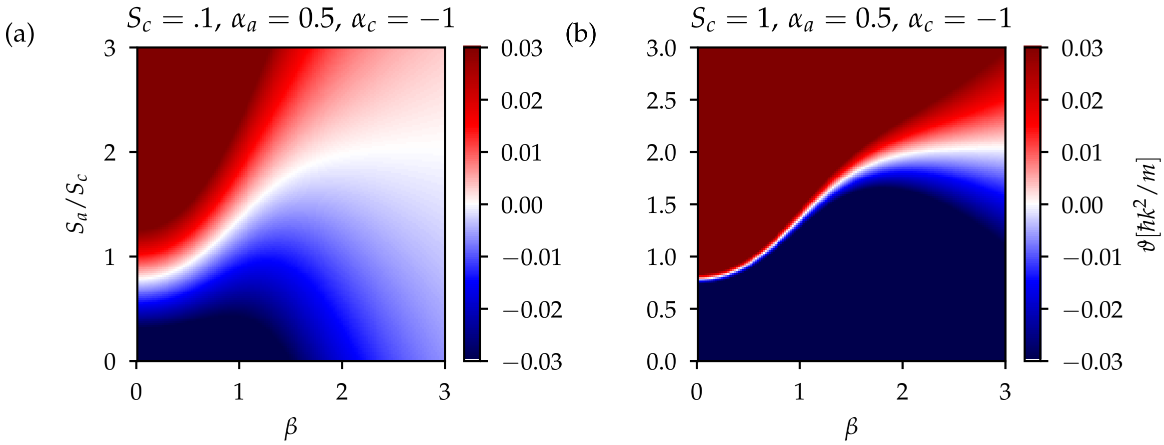

Figure 2.5.: ϑ as a function of the amplification saturation parameter ratio S_a/S_c and the velocity amplitude β. Stable steady state amplitudes are those for which $\vartheta = 0$ (white lines) and $\partial\vartheta/\partial\beta < 0$. Therefore only a limited region of S_a/S_c is stable, as can be seen from the plot. (a) and (b) differ only in their value of S_c. For larger S_c the effective force restoring the operating point is stronger.

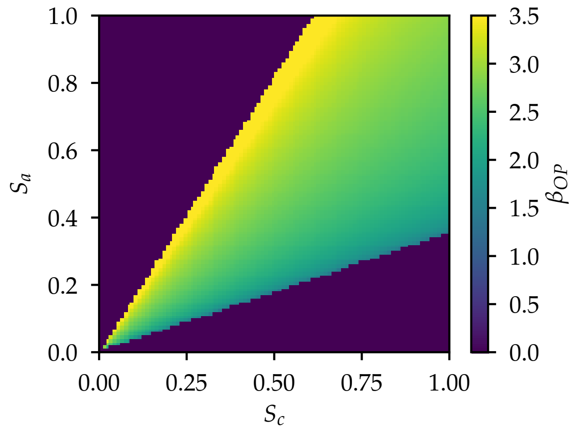

Figure 2.6.: Oscillation amplitude β_{OP} as a function of the saturation parameters ($\alpha_c = -3$, $\alpha_a = 2$). One can easily recognize the threshold behavior of the oscillation depending on the laser intensities.

must hold. In the following we will use the dimensionless expressions

$$\begin{aligned} \alpha_a = 2\delta_a/\gamma \qquad \alpha_c = 2\delta_c/\gamma \\ \beta = 2k\omega A_0/\gamma \end{aligned} \tag{2.50}$$

for the detunings and the oscillation amplitude. Using the solutions for the integrals G and K provided in appendix A we can numerically evaluate ϑ for different operation parameters. For fixed S_a, S_c, α_a, α_c we get a dependence of the effective powers of the cooling and amplification beams on the amplitude β as depicted in Figure 2.3. We see that in this specific case a root of ϑ, marked by a dashed line, exists. Furthermore, at this point $\mathrm{d}\vartheta/\mathrm{d}\beta < 0$ which means that the oscillation is amplified below this point and is damped above it. The oscillation will consequently be stable and we call the corresponding amplitude β_{OP} the *operating point*. If no root of ϑ exists or if $\mathrm{d}\vartheta/\mathrm{d}\beta|_{\beta_{OP}} > 0$ the oscillation will not be stable. We will now discuss how this operating point behaves for general combinations of the operation parameters.

We first consider the case of identical saturation parameters $S_a = S_c$ and plot ϑ in Figure 2.4(a) versus the blue detuning α_a and the velocity amplitude β, for a fixed values of α_c and the saturation parameters. For $\alpha_a < |\alpha_c|$ there is a transition from $\vartheta > 0$ to $\vartheta < 0$ for increasing β, yielding stable oscillations. The oscillation amplitude will assume a value for which $\vartheta = 0$, which defines the operating point of the oscillation. For $\alpha_a > |\alpha_c|$ excursions to increased amplitude lead to increased amplification (and vice versa for small amplitudes) prohibiting stable oscillation. Additionally, there is a threshold value for α_a below which ϑ is always negative and only damping is possible. We also discuss the case of unbalanced saturation parameters $S_a \neq S_c$ which is depicted in Figure 2.4(b) and Figure 2.4(c). For $S_a < S_c$ the stability region is smaller as compared to the balanced case. For $S_a > S_c$ the amplitude diverges for α_a approaching $|\alpha_c|$.

Alternatively, we can investigate the stability in terms of the ratio of the saturation parameters. In Figure 2.5 ϑ is plotted as a function of S_a/S_c and β and for fixed detunings. Again there is a threshold of S_a/S_c below which no stable oscillation is possible. Also, an upper bound of the stability region in terms of S_a/S_c can be seen. Inside this region the oscillation amplitude increases with increasing S_a/S_c. Additionally, the stable amplitude β does not depend on S_c but will be confined tighter for larger S_c.

For equal saturation parameters $S_a = S_c = S$ and detunings $\alpha_a \lessapprox \alpha_c$ (the oscillation is not stable for $\alpha_a \geq \alpha_c$) convenient approximations can be made that allow for derivations of analytic expression that would otherwise be hard or impossible. In the following we will partly use this specific case of operation parameters to derive analytic expressions, e.g. for the phase diffusion coefficient. To gain insight into more general cases we will use numerical methods.

The first expression we can find in this case, is one for the operating point β_{OP}. Using the analytical expressions for G and K derived in appendix A one can show that for large $|\alpha_c|$ (and $S_a = S_c$, $\alpha_a \lessapprox \alpha_c$) the operating point amplitude becomes approximately

$$\beta_{OP} = |\alpha_c| + \frac{1}{\sqrt{3}} \tag{2.51}$$

Alternatively, β_{OP} can be numerically evaluated for arbitrary values of the operation parameters by finding roots of ϑ.

2.2.4. Phase Diffusion Coefficient

As already discussed, the phase stability determines the quality of the clock. Due to the spontaneous emission events, the ion experiences random momentum kicks that lead to phase diffusion, i.e. a random walk of the oscillation phase. To quantify the dephasing rate, we will use the *phase diffusion coefficient* D_ϕ which has already been introduced in Equation (2.39). Starting from the integral expression Equation (2.48) for D_ϕ and using I_D introduced in appendix A we get

$$D_\phi = \frac{z}{4\pi}\left(\frac{\hbar k/m}{\omega A_0}\right)^2 \frac{\gamma}{2}\left[S_c I_D(\alpha_c, \beta) + S_a I_D(\alpha_a, \beta)\right] . \tag{2.52}$$

Equation (2.52) holds generally for arbitrary values of the saturation parameters, detunings and amplitude. We can therefore calculate the stable oscillation amplitude numerically by finding the root of ϑ (Equation (2.49)) and then compute D_ϕ using Equation (2.52).

For the aforementioned case $S_a = S_c = S$, $\delta_a \lessapprox \delta_c$, we can also find an analytical expression for D_ϕ. If we use the approximate expression Equation (2.51) to eliminate β and the explicit expression for I_D we obtain

$$D_\phi = z\frac{(\hbar k^2/m)^2}{\gamma/2}\, S\, 3^{1/4}\, |\alpha_c|^{-7/2} . \tag{2.53}$$

In this case, and for the used approximation, the phase diffusion therefore becomes larger with increasing light intensity or decreasing detuning. We will see however below that this does not hold for arbitrary operation parameters.

2.2.5. Scattering During an Oscillation Cycle

The amount and distribution of scattered photons during an oscillation cycle are important for several reasons: First, the distribution of photon scattering events over the oscillation cycle determines the ability to measure the phase via the scattered photons: If the scattering rate is *not* sharply peaked around a certain phase, the detected phase will have a large uncertainty. Instead of a random walk in phase for the phase diffusion case, this will lead to white noise in phase. Second, the total amount of scattered photons during a cycle is important as it determines the phase diffusion coefficient.

In the unsaturated case ($S_a, S_c \ll 1$) and for a small change in the Doppler shift during an emission event ($kA_0\omega^2/\gamma^2 \ll 1$), the total scattering rate for the instantaneous velocity v is the sum of the rates of the two beams

$$R(v) = R_c(v) + R_a(v) . \tag{2.54}$$

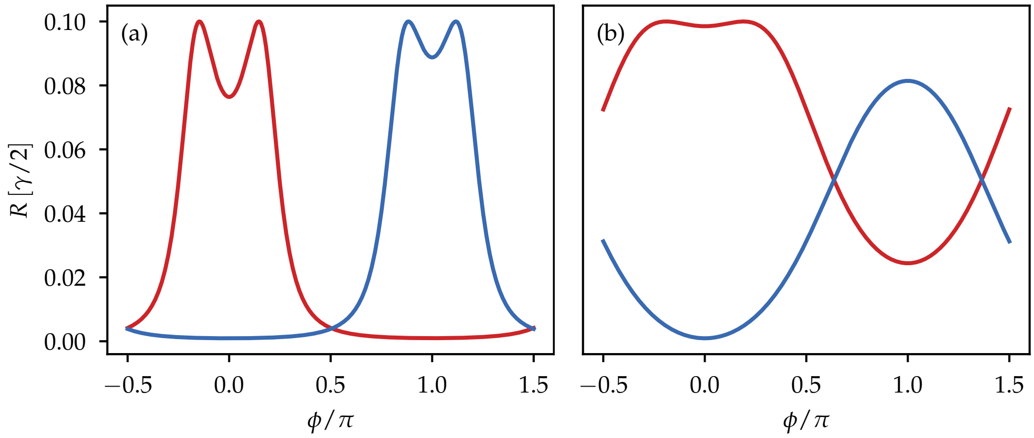

Figure 2.7.: Scattering rate during a cycle over the oscillation phase ϕ for $S_a = S_c = 0.1$. Scattering rate of the cooling beam R_c in blue and of the amplification beam R_a in red. (a) For large detunings $\alpha_c = -5,\ \alpha_a = 4.9$. (b) For small detunings $\alpha_c = -1,\ \alpha_a = 0.5$.

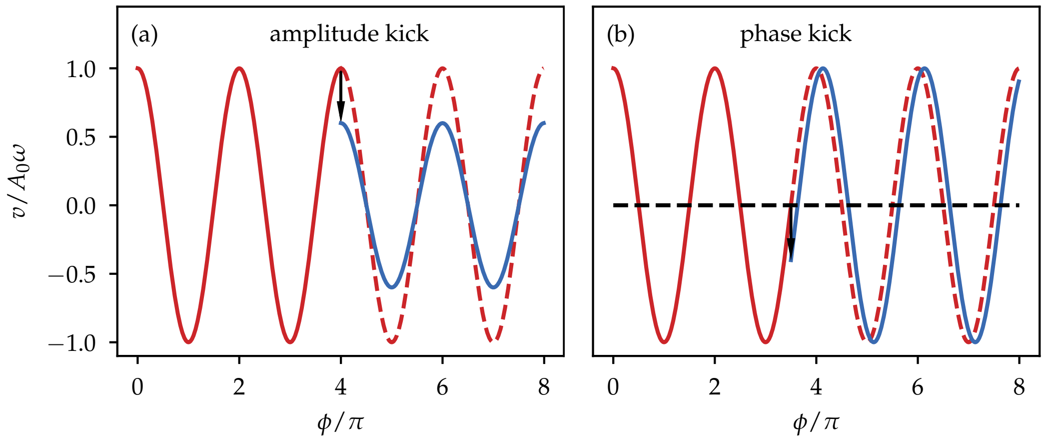

Figure 2.8.: Different behavior of the oscillation for different phases of a scattering event. In both cases, the scattering of a photon (black arrow, exaggerated in the figure) changes the instantaneous velocity v by the same amount. (a) If the scattering occurs at a point of maximum velocity, the change in velocity will lead to change in amplitude but the oscillation phase will be unchanged. (b) If the scattering occurs for zero velocity, the amplitude will stay unchanged while the change in phase will be maximal. The horizontal dashed line simply marks $v = 0$.

For a sinusoidal oscillation $v = \omega A_0 \cos(\phi)$ we can describe the total scattering rate as a function of the oscillation phase ϕ. An exemplary plot of R versus ϕ is depicted in Figure 2.7. We can observe that during a full oscillation cycle two main peaks, one for each beam, are present. As $v = \omega A_0 \cos(\phi)$, resonant velocity is reached twice per cycle for each of the two beams resulting in two sub-peaks for each beam. The separation of these sub-peaks evidently depends on the detuing from resonance. For the equal intensities and detunings approximation and for large α_c we can express the width at half height of the resonance peaks as a function of α_c

$$\delta\phi = 2\sqrt{2(1+1/\sqrt{3})}\,|\alpha_c|^{-1/2}\,. \tag{2.55}$$

Larger detunings will therefore lead to a more narrow peak. Also higher intensities will lead to saturation broadening and a wider peak (this is outside the large α_c approximation and therefore does not appear in Equation (2.55)).

We can also derive an expression for the total amount of scattered photons during a cycle by integrating the scattering rate over one cycle. By again using the integral expressions from appendix A we get the total number of photons

$$N_c = \frac{\gamma/2}{\omega}\left[S_c I_N(\alpha_c,\beta) + S_a I_N(\alpha_a,\beta)\right]\,. \tag{2.56}$$

Within the equal detuning and intensities approximation, this leads to

$$N_c = \frac{\gamma/2}{\omega} S\pi 3^{3/4} |\alpha_c|^{-1/2}\,. \tag{2.57}$$

For this particular case, we can relate the two quantities and get the phase diffusion coefficient in terms of N_c:

$$D_\phi = \frac{z\omega}{\pi\sqrt{3}}\left(\frac{\hbar k^2/m}{\gamma/2}\right)^2 N_c\,|\alpha_c|^{-3} \tag{2.58}$$

It is noteworthy that the maxima of the scattering are always close to the maxima of the velocity (see Figure 2.7). This leads to the conclusion that the photon scattering event will mainly lead to a change in oscillation amplitude rather than in a change in oscillation phase as can be easily comprehended from Figure 2.8. This makes the oscillation inherently phase stable.

2.2.6. Measure of Oscillator Stability

Analogously to the definition of the clock accuracy introduced in Section 1.1 we define the accuracy N_A as the number of cycles at which the uncertainty of the start of the cycle equals a cycle duration, i.e. $\Delta\phi(t = N_A\tau) = 2\pi$ for $\tau = {}^{2\pi}/_{\omega}$. Using the equal intensities and detunings approximations Equation (2.39) and Equation (2.58) we get

$$N_c\, N_A = \frac{\sqrt{3}\pi^2}{z}\left(\frac{\gamma/2}{\hbar k^2/m}\right)^2 |\alpha_c|^3\,. \tag{2.59}$$

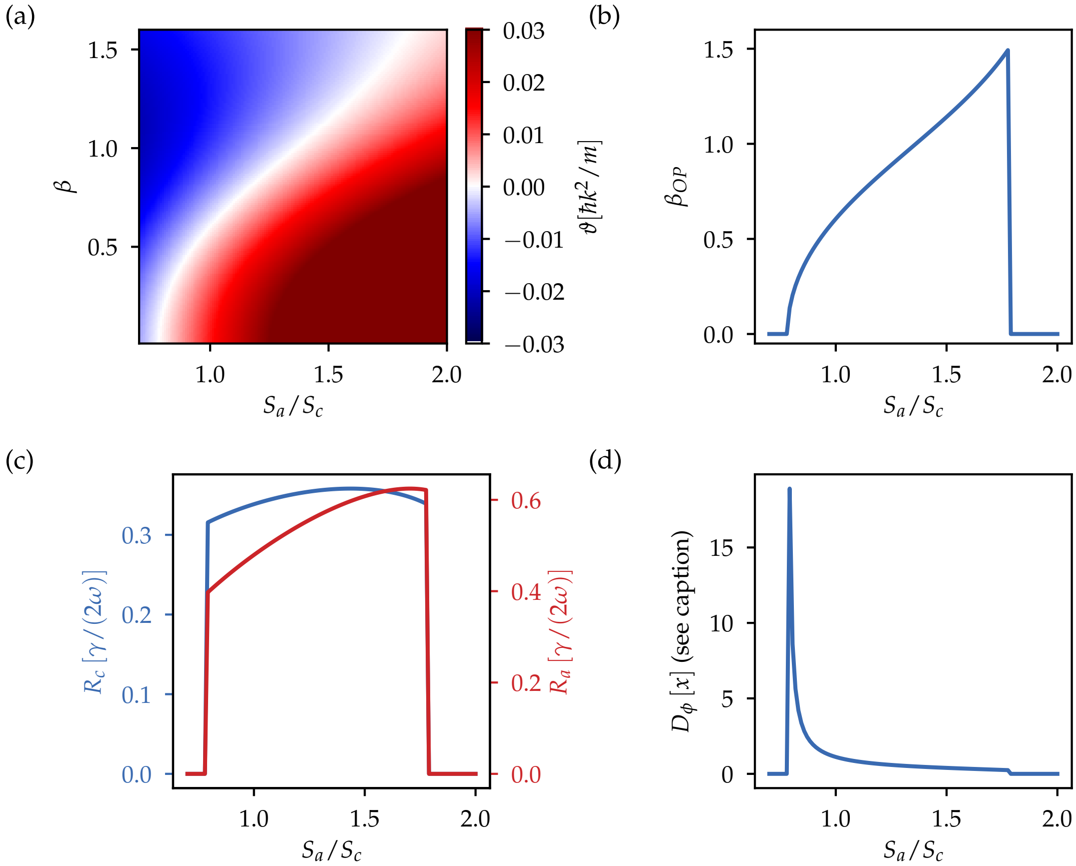

Figure 2.9.: (a) ϑ is used to numerically find the operating point amplitude β_{OP} depicted in (b) ($S_c = 0.1$, $\alpha_c = -1$, $\alpha_a = 0.5$). (c) Number of the scattered photons per oscillation cycle for the cooling beam R_c in blue and for the amplification beam R_a in red. (d) Phase diffusion coefficient D_ϕ in units of $x = (g/(4\pi))\,(\hbar k^2/m)^2\, 1/(\gamma/2)$ versus S_a/S_c. For small S_a the amplification is below the oscillation threshold. Above the threshold, D_ϕ is large and then decreases rapidly with S_a.

We immediately see that the accuracy is inversely proportional to the number of scattered photons.

The result obtained within the approximation is therefore in direct contrast to the conjecture made by Erker et al. [16], that the clock accuracy improve is accompanied by increased generation of waste heat. This can lead to the following conclusions:

- The conjecture by Erker et al. was verified for a specific clock implementation, but does not hold in general.
- Our specific implementation can not be seen as an autonomous clock operating in the thermodynamic limit.
- Our clock is not driven by thermal resources, but rather by low-entropy resources, and the conjecture does not hold for this case
- The model we use for our clock is incomplete or the approximations that have been made in Section 2.2.1 mask the connection between accuracy and waste heat.
- The contrast appears only within the approximation, which does not necessarily yield optimum operation parameters, and the conjecture only hold for optimium operation.

Therefore, a more thorough investigation of the relation between clock accuracy and operation parameters is necessary. The simplest way to extend Equation (2.59) to a more general case is to abandon the equal intensity and detuning approximation. In this general case we obtain behaviors contradicting Equation (2.59) as depicted in Figure 2.9. For a given set of S_c, S_a, α_c, α_a, the oscillation amplitude β_{OP} is numerically computed by finding roots of θ (Equation (2.49)) as depicted in Figure 2.9(b). D_ϕ can then be computed using Equation (2.52). Leaving S_c, α_c, α_a fixed, and varying S_a yields the phase diffusion coefficient plotted in Figure 2.9(d). We see again the threshold behavior of the oscillation: Below a certain S_a, the oscillation amplitude is zero and displays an increase beyond this threshold. At the threshold, D_ϕ assumes diverging values, while it decreases towards larger values of S_a. At the same time the scattering rates increase with increasing S_a as depicted in Figure 2.9(c). Consequently, we have a quite similar situation as depicted in Figure 1.2. In both cases the accuracy of the clock increase with the entropy production (quantified by heat in one and scattering rate in the other case) before reaching an approximately constant plateau. It is important to note, that this behavior depends on the way the scattering rate is increased. If we hold S_a fixed and increase S_c, we will find an increase in the phase diffusion coefficient instead of a decrease, as can be seen in the plot depicted in Figure B.2. A plot of D_ϕ over both S_a and S_c can be found in Figure B.1. It is therefore not completely clear how this result can be compared to those presented in Section 1.1.

3. Experimental Apparatus

The experimental apparatus consists of a Paul trap [1, 2] inside a vacuum chamber and laser optics that enable control over the ions internal and motional states. Figure 3.2 depicts a sketch of the setup. In Section 3.1 we will discuss the trap itself, in Section 3.2 the lasers and optics needed for the experiment and finally various electronics in Section 3.3. For more details see the work of Kaufmann [26] and Ruster [27].

3.1. The Ion Trap

The trap consists of two gold coated chips that form the DC and radio frequency (RF) electrodes separated by an insulating layer as depicted in Figure 3.1. The RF electrodes are supplied at a trap drive frequency of $2\pi \times 33\,\mathrm{MHz}$ and a peak-to-peak voltage of about $320\,\mathrm{V}$, leading to a radial confinement corresponding to trap frequencies of $\omega_x \approx 2\pi \times 3.8\,\mathrm{MHz}$ and $\omega_y \approx 2\pi \times 4.6\,\mathrm{MHz}$. Axial confinement corresponding to a trap frequency of $\omega_z \approx 2\pi \times 1.5\,\mathrm{MHz}$ is generated by a DC voltage of $-6\,\mathrm{V}$ at one trap segment. The trap is wire-bonded to a filter board, where low-pass filters suppress RF pickup from the RF to the DC electrodes and electrical noise. The trap consists of 32 independent segments between which ions can be shuttled by controlling the axial confinement through the DC voltages. In the experiments presented in this thesis, we will however only use a single segment.

Together with the filter board, the trap is mounted into a ultra high vacuum chamber. To provide a well defined quantization axis and for energetically splitting of degenerate states of the ion, an external magnetic field of $\approx 340\,\mu\mathrm{T}$ gives rise to a Zeeman splitting of $2\pi \times 10\,\mathrm{MHz}$ between the sublevels of the $S_{1/2}$ electronic ground state. Ions are trapped via resonantly enhanced photoionization of neutral Ca atoms from an effusive beam emanated from an oven [28].

3.2. Optics and Lasers

Lasers and various optical components are used in the experiment. Loading ions, cooling, coherent manipulation and of course sustained harmonic oscillation of the ion in the trap all require lasers resonant or near resonant to some electronic transitions of the ion. All of these lasers and some important components will be briefly discussed in this section. An overview on the relevant lasers and their orientation relative to the trap and the magnetic field is given in Figure 3.2.

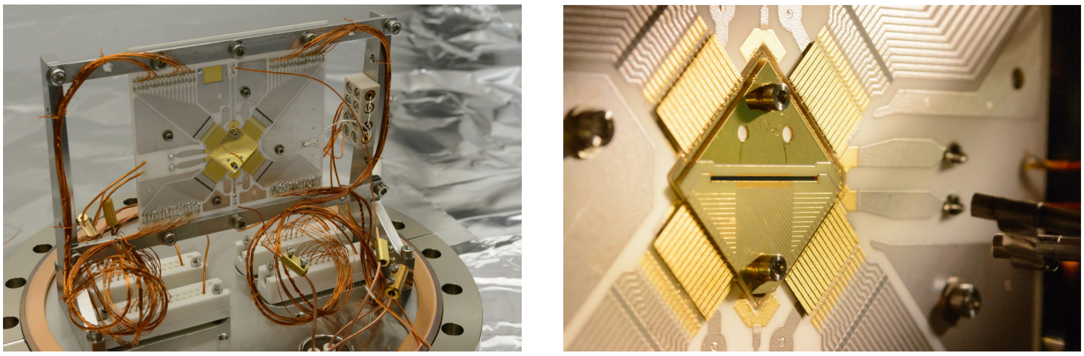

(a) (b)

Figure 3.1.: Pictures of the segmented Paul trap used in the experiment (taken from [26]). (a) Trap chip mounted to the filter board for electronic filtering, connected to the vacuum flange both mechanically and electronically. (b) Closeup of the trap chip wirebonded to the filterboard. The tube on the right is the calcium oven approximately 1 cm away from the trap surface.

Detection

Photons scattered by the ion need to be detected both to distinguish between magnetic substates in Chapter 5 and to detect the oscillation in Chapter 6. In our setup we use an objective [1] mounted inside an inverted viewport to decrease the distance to the ion and thus increase the covered solid angle. Of the light collected by the objective 10 % is split of to the EMCCD camera using a beamsplitter. Most of the emitted light is focused onto a PMT [2] for detection. In both cases a narrow bandpass filter [3] transmits only light around 397 nm.

397 nm: Light Forces

A 396.959 nm laser near resonant to the $S_{1/2} \leftrightarrow P_{1/2}$ transition is employed to generate radiation pressure forces depending on the detuning from resonance. If it is red detuned it decreases the ions velocity, if it is blue detuned it increases it. For the measurements in Chapter 4 and Chapter 5 a single red detuned, vertical and thus π polarized beam is used for Doppler cooling [23, 24] and fluorescence detection. To drive the spatial oscillation of the ion, a red detuned σ_+ polarized and a blue detuned π polarized beam are used. These two beams will consequently be called "Sigma" and "Doppler" or "cooling" and "amplification" beams in the following. Both of the beams are derived from a diode laser source [4]. Subsequently, two independent acousto-optical modulators (AOMs) shift the light frequency in a double pass configuration and are used for turning the beams on and off. A single mode fiber then guides the light to the trap. Using a Pound-Drever-Hall type locking technique [29] the laser frequency is stabilized to a cavity. The π polarized

[1] $f \approx 67$ mm, $d_o = 45$ mm, $l = 192$ mm, S6ASS2241/045 SILL 132177, Sill Optics GmbH & Co. KG
[2] Photon counting head H10682-210, Hamamatsu Photonics K.K.
[3] Semrock FF01-395/11
[4] DL 100 Pro (TOPTICA Photonics)

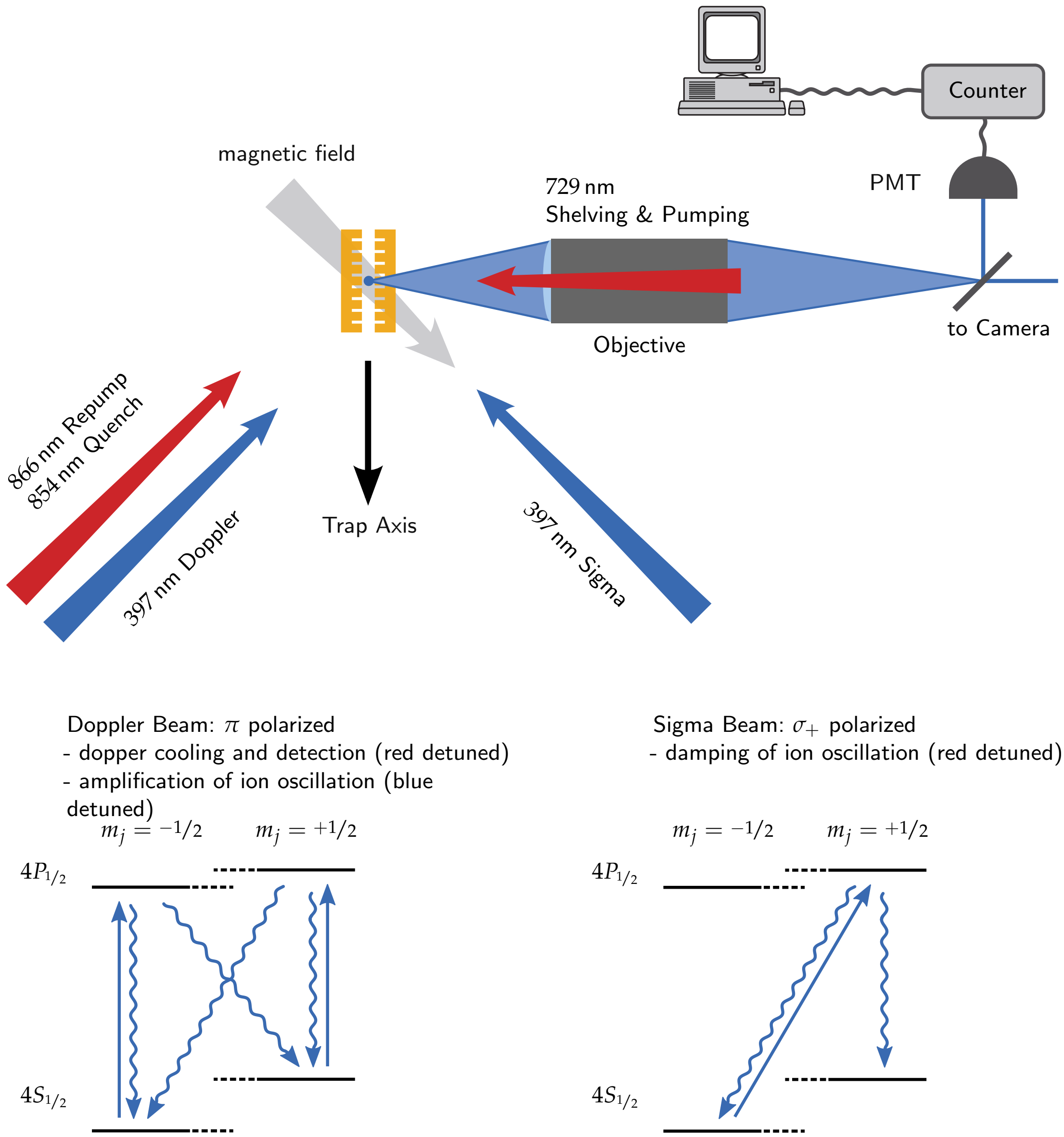

Figure 3.2.: Sketch of experimental setup. The segmented trap is depicted in gold in the middle. Inside an inverted view port an objective collects the fluorescence light from the ion and guides it to the photomultiplier tube (PMT) and the electron multiplying charge-coupled device (EMCCD) camera. The signal from the PMT is transmitted to a counter which can be read out using a personal computer. The Doppler beam, which is π polarized, is used for Doppler cooling and detection for some measurements while it is used as the amplification beam for the sustained ion oscillation. The Sigma beam, which is σ_+ polarized, is used for damping of the ion oscillation.

beam is polarized parallel to the magnetic field using a polarizing beam splitter (PBS) just before the vacuum chamber. A Glan-Taylor polarizer and a subsequent $\lambda/4$-plate produce the right circular light needed for the Sigma beam.

866 nm & 854 nm: Repumping

During illumination of the ion with 397 nm or 729 nm light, the dark, metastable $D_{3/2}$ and $D_{5/2}$ states become populated. 866.451 nm (repump) and 854.443 nm (quench) light [5] is used to transfer the population back into the $P_{1/2}$ or $P_{3/2}$ states respectively, from where rapid decay into the $S_{1/2}$ ground state is possible. Both of these lasers are stabilized in frequency using the measurement from a wavelength meter [6]. Both beams are shifted in frequency using AOMs and are then overlapped on a PBS before being coupled into a single-mode fiber. After the fiber, the polarization is rotated to be diagonal to the magnetic field to drive $\Delta m = 0, \pm 1$ transitions and thus address all possible sublevels.

729 nm: Shelving and Pumping

729.347 nm[7] light drives the $S_{1/2} \rightarrow D_{5/2}$ electric quadrupole transition. It is used both for optical pumping and for shelving of individual Zeeman $S_{1/2}$ states for state detection which is necessary for the experiments in Chapter 5. The diode laser frequency is stabilized relative to a high-finesse Fabry-Perot cavity [8] using a Pound-Drever-Hall technique. Its frequency is shifted using an AOM and it is guided to the trap using a single mode fiber where the beam is focused on the ion using the same objective as for imaging.

3.3. Electronics

For some of the experiments presented in Chapter 4 and Chapter 5, multiple electronic components like AOMs or a PMT for fluorescence detection need to be controlled synchronously and on the timescale of sub-microseconds. A custom-made arbitrary waveform generator based on a FPGA can be programmed to address those components and to run complex experiment sequences. For the oscillation measurement in Chapter 6, continuous laser beams are used and such well timed control is not necessary. However, we need to calibrate the intensities and frequency detunings of the beams and have higher requirements on the detection of the scattered light as discussed in the following.

[5] both DL 100 (TOPTICA Photonics)
[6] Wavelength Meter WSU, HighFinesse Laser and Electronic Systems, ≈ 10 MHz accuracy.
[7] TA 100 (TOPTICA Photonics)
[8] ATFilms 6020 notched cavity, finesse $F \approx 140\,000$ [30]

Lase Intensity and Frequency Calibration

For driving the trapped-ion phonon laser, two laser beams are employed as descibed above in Section 1.2. For the experiments presented in thesis, the existing control infrastructure for these lasers was modified. Each of the double-pass AOMs controlling the frequency and intensity of these beams is now individually driven by a voltage-controlled oscillator (VCO), where the frequency is tuned within the range between 80 MHz and 150 MHz via an analog voltage derived from the experiment control system. To calibrate the voltage supplied to the VCOs to a frequency, the frequency was measured once versus the voltage using an oscilloscope. This calibration measurement was then used to determine the actual AOM frequency in the measurements.

The efficiency of the AOMs depend on their driving frequency, such that the laser intensity arriving at the ion varies correspondingly. Consequently, a system is needed to maintain constant intensity at varying optical frequency. This is done by adjusting the RF amplitude of the signal going into the AOMs using a variable attenuator. A small part of the beam is split of before the trap and is focused onto a photo diode which outputs a voltage proportional to the intensity. We then use a simple search algorithm that finds the correct RF amplitude for the AOM that leads to the desired intensity. Obviously, this enables us to calibrate intensities in terms of the photo diode voltage but not in absolute terms relative to an atomic transition. This already motivates the measurements presented in Chapter 5 that aim at calibrating intensities in units of the resonant saturation parameter of a transition.

In some of the measurements, laser intensities are required that are significantly smaller then the common intensities used for fluorescence detection or Doppler cooling. To attenuate the 397 nm laser, an electro optical modulator (EOM) [9] was installed which, together with a $\lambda/2$-plate, reduces the intensity of both the Doppler and the Sigma beam. The EOM can be switched between two states during experiment sequences which is used in the measurements presented in Chapter 5.

Detection

For fluorescence detection, two different schemes are used in this work. For the measurements presented in Chapter 4 and Chapter 5, a custom-made counter based on a micro controller is connected to the PMT output and the number of measured photons can be read out using a computer. This allows for the discrimination of the two $m_j = \pm 1$ ground level states after shelving to the dark $D_{5/2}$ state as described in Section 5.2. For the oscillation stability measurement in Chapter 6, measurement of an averaged count rate is not sufficient. Here it is necessary to measure arrival times of photons on timescales much shorter then one oscillation period of about 0.6 µs. For this purpose, a PicoQuant PicoHarp 300 time tagging module is used. It supplies time stamps with a resolution of 4 ps and a dead time of < 95 ns, surpassing the requirements for the resolution by orders of magnitude. The same PMT is used in that case for the detection of the photons

[9] Linos LM0202

4. Photon Detection Efficiency

For multiple reasons the amount of scattered photons and its distribution over time is a crucial quantity in this thesis. The amount of photons scattered from the ion is our measure of waste heat, i.e. the entropy produced by the system as described in Section 1.2. Its distribution is important to infer the oscillation stability of the ion as explained in Chapter 6. Finally we want to measure the total amount of scattered photons to approximate the degree certain magnetic sublevels are depleted during scattering to estimate how good our approximation of a two level system in Section 2.2 actually is. Due to numerous imperfections in the experimental system, not all photons emitted by the ion are detected by the photomultiplier tube (PMT). Combining the efficiency of the involved components yields an estimate for the total detection efficiency. Previous measurements [31] however show that the actual measured count rates are significantly lower then the expected values. In this chapter we present a simple and accurate method to measure the photon detection efficiency without any previous knowledge about any of the involved components.

For the experimental setup described in Chapter 3 we can summarize the different effects that lead to a count rate at the PMT which is lower then the scattering rate of the ion:

- Collection of the scattered light with an objective from one side at a finite distance from the ion leads to a covered solid angle of $\Omega/4\pi \approx 2.48\,\%$ (lens diameter $d = 38\,\mathrm{mm}$, distance to ion $g \approx 60\,\mathrm{mm}$, g is not known very well however) [32].
- The objective [1] has a transmission of 96 % [32].
- The fluorescence light is filtered before the PMT using a bandpass filter [2] with a transmission of $> 85\,\%$ at 397 nm.
- The PMT [3] has a quantum efficiency of about 20 %. This is however only a very rough estimation as no specific value for used PMT is known.
- Only about 90 % of the light is detected by the PMT, the rest is directed to the electron multiplying charge-coupled device (EMCCD) camera using a beamsplitter.

Multiplying these contributions yields an expected efficiency of 0.36 %. As the value of the solid angle and the PMT quantum efficiency is not very well known, this result can only be seen as a rough estimate.

To measure the actual detection efficiency, a simple experiment sequence is used, which is depicted in Figure 4.1. The goal is to extract exactly one photon from the ion per experimental run and then count the photons using the PMT. The number of measured photons divided by the number of experiments then directly gives the detection efficiency.

[1] $f \approx 67\,\mathrm{mm}$, $d_o = 45\,\mathrm{mm}$, $l = 192\,\mathrm{mm}$, S6ASS2241/045 SILL 132177, Sill Optics GmbH & Co. KG
[2] Semrock FF01-395/11
[3] Photon counting head H10682-210, Hamamatsu Photonics K.K.

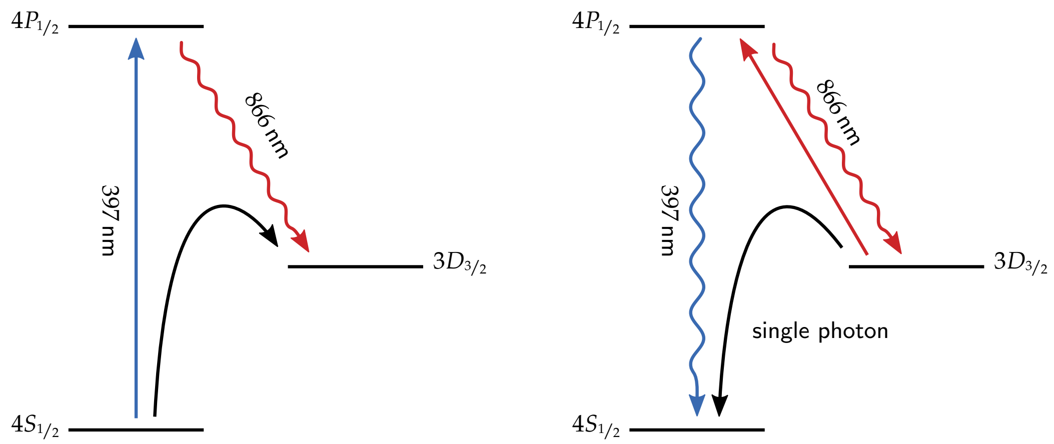

(a) (b)

Figure 4.1.: Schematic steps in the process to extract exactly one photon from the ion to then measure the detection efficiency of the setup. (a) First the ion is illuminated with a 397 nm beam, which drives transitions to the $P_{1/2}$ state from which population can decay into the metastable $D_{3/2}$ state. (b) After all population has been transferred, a 866 nm repump beam drives the transition to the $P_{1/2}$ state from which decay back into the $S_{1/2}$ ground state is again possible. Exactly one 397 nm photon will then be emitted on this transition.

In order to get exactly one scattered photon from the ion, a meta-stable dark state is used. After Doppler cooling, only the 397 nm cooling beam is switched on without the 866 nm repump beam. Consequently, after a time much larger than the $P_{1/2}$ life time, the ion will be pumped to the meta-stable $D_{3/2}$ state (lifetime 1.18 s [33]). The time needs to be large compared to the lifetime, as the decay to the $D_{3/2}$ state is suppressed by a factor of 15.88 [34] as compared to the decay into the $P_{1/2}$ state. If the 866 nm repump beam is now switched on, population will be transferred from this state back to the $P_{1/2}$ state. Now either a 866 nm photon can be emitted, leaving the ion in $D_{3/2}$ again or a 397 nm emission transfers the ion to $S_{1/2}$. In any case, after sufficient 866 nm irradiation, exactly one 397 nm photon will be emitted. Here, an irradiation duration of a few $P_{1/2}$ lifetimes is sufficient, as the branching ratio favors the 397 nm decay. In the ideal case, longer times should not change the result.In practice however, it should be chosen as small as possible to minimize the effect of stray light and dark counts.

To correct for detected photons due to dark counts and stray light we also measure the background count rate and subtract it from the value measured using the scheme above. We measure the background by detecting the photons while illuminating the ion with the 866 nm light, exactly the same as in the actual measurement, just without transferring the population into the $D_{3/2}$ state first with the 397 nm light. To eliminate systematic drifts in the background count rate the background is measured in an interleaved fashion between the experiment runs. Using the number of detected photons from $3.6 \cdot 10^6$

experiment runs, we get a value for the efficiency of

$$\eta = 0.1243(21)\,\%\,.$$

For these measurements, the ion was first illuminated with 397 nm light for 10 µs before switching on the 866 nm light and simultaneously detecting the scattered photons for 2 µs.

This value is about half the expected efficiency computed from the individual efficiencies. Keeping in mind that the individual efficiencies are not very well known, the difference between the values is not unreasonably large.

5. Dipole Transition Calibration

For the oscillation stability measurements presented in Chapter 6 it is necessary to know the laser operation parameters in terms of units of the atomic dipole transition, i.e. the resonant saturation parameter S_0 and the frequency detuning δ from resonance. In the lab however, we set those quantities using voltages of photo diodes for the laser intensity and acousto-optical modulator (AOM) frequencies for the detuning. In this chapter we will present a method to measure saturation parameters and detunings relative to an atomic transition which enables the calibration of the values set in the lab to these quantities. These calibrations are then used in Chapter 6 to determine the operation parameters of the cooling and the amplification beams, i.e. the 397 nm Doppler and Sigma beams.

In principle, one could simply measure the rate of photons scattered by the ion for different laser frequencies. Using Equations (2.14) along with the measured photon detection efficiency η, the detuning δ and the Rabi frequency Ω could be determined. However, there are several problems to this approach. First, for low laser powers the count rates would be quite low and the measurement time to acquire sufficiently good statistics would be relatively high. This is especially important, as the photon detection efficiency is quite low (see Chapter 4). Second, for continuous illumination by the laser, radiation pressure forces will have a significant impact on the motional state of the ion and therefore on the scattering. Only the red detuned side of the resonance can be easily measured as the ion heats up for blue detuned radiation. But also on the red detuned side of the resonance will radiation pressure effects distort the line shape compared to Equations (2.14). Additionally, Equations (2.14) holds only for an ideal two-level system. For our particular problem, four subtransitions can be driven, and using a sum Lorentzians given by Equations (2.14) requires additional assumptions on the laser polarization components.

Here, a different technique is used that is based on the measurement of spin-flip rates. By spin-flip we understand the transfer of population between the $|4^2S_{1/2}, m_j = -1/2\rangle$ and $|4^2S_{1/2}, m_j = +1/2\rangle$ states (further denoted as $|\downarrow\rangle$ and $|\uparrow\rangle$ respectively) as depicted in Figure 5.1. Depending on the polarization direction of the laser relative to the magnetic field at the ion, $\Delta m = 0, \pm 1$ transitions can be driven, effectively transferring population between the two spin states. Evidently, the amount of this transfer depends on the rate at which photons are scattered by the ion and thus on the detuning from the transition and the Rabi frequency, i.e. the light intensity. Measuring spin-flip rates can therefore be used to infer these quantities. This method has the distinct advantage that the amount of scattered light can be extremely low (only a few photons are necessary) and therefore the influence on the motional state of the ion is small.

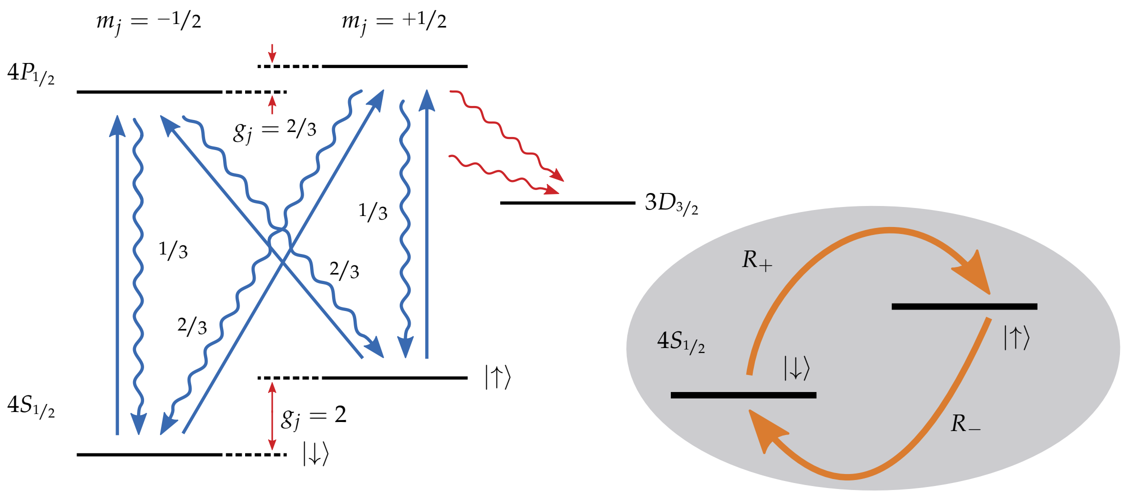

Figure 5.1.: Illustration of the population transfer between the two Zeeman sublevels (spin-states) $|\uparrow\rangle$ and $|\downarrow\rangle$ of the $|4S_{1/2}\rangle$ state. 397 nm light drives the $|4S_{1/2}\rangle \leftrightarrow |4P_{1/2}\rangle$ transition (blue arrows) inducing a change in the magnetic quantum number m_j by excitations and decays with $\Delta m_j = \pm 1$. The allowed excitations depend on the polarization of the light field. Here all possibilities are depicted. As the Landé factors g_j are different for the two levels, all four transitions have different energies, this needs to be considered for the detuning δ in Equation (5.6). As represented in Equations (5.12), the branching to the $|3D_{3/2}\rangle$ state needs to be taken into account (red, wiggly arrows). The rates $R_\pm$ then describe the rates at which population is transferred between the states spin-states (orange arrows).

The idea for this method is inspired by work conducted by Hettrich et al. [35]. There, the measurement of spin-flip rates is used for precise measurements of the dipole matrix elements of the $S_{1/2} \leftrightarrow P_{1/2}$ transition. Contrary to the work presented in that publication, the approximation of large detunings does not hold for the experiment presented here. This is the main difference, otherwise the theoretical model is essentially the same as the one presented in the following.

We will first establish the theory needed to find analytical expressions for these rates depending on the Rabi frequency and the detuning in Section 5.1. Subsequently, we briefly discuss in Section 5.2 how spin state populations can be measured in an experiment, before finally presenting experiments to calibrate Rabi frequency and the detuning for the 397 nm laser beams via these rates in Section 5.3.

5.1. Spin-Flip Rates

In this section the rates of population transfer between spin states will be derived. We will find expressions for these rates in the case of constant driving of the $|4^2S_{1/2}\rangle \leftrightarrow |4^2P_{1/2}\rangle$ transition as a functions of the laser intensities and frequency detunings. $R_+(R_-)$ is defined as the rate at which population in transferred from $|\downarrow\rangle$ to $|\uparrow\rangle$ ($|\uparrow\rangle$ to $|\downarrow\rangle$) as depicted in Figure 5.1. We will first extend the theory of a two-level system (TLS) summarized in Section 2.1 to multilevel systems in Section 5.1.1 before analyzing the rates $R_\pm$ and the resulting state populations in Section 5.1.2. We will restrict this derivation to the case of pure σ_+ and pure π polarization as the two beams used in the experiments have those polarizations. The case of σ_+ polarization will be discussed in detail before reviewing the essentially analogous derivation for π polarization.

5.1.1. Rabi Frequencies for Multiple Transitions

For a TLS there is simply one matrix element of the dipole operator $\mathcal{D} = \langle e|\, d\, |g\rangle$. If, however, more energy levels are involved, dipole matrix elements will depend on the chosen final and initial states and they become $\mathcal{D}_{if} = \langle f|\, d\, |i\rangle$. A simple and elegant way to compute these matrix elements for angular momentum eigenstates $|j,m\rangle$ is through the Wigner-Eckert theorem [36] which separates $\mathcal{D}$ into the reduces dipole matrix element $\tilde{\mathcal{D}}$, which is independent of j and m, and a Glebsch-Gordon coefficient:

$$\mathcal{D} = \langle j',m'|\, d\, |j,m\rangle = \tilde{\mathcal{D}} \langle j,m;1,q|j',m'\rangle \;. \tag{5.1}$$

For the sake of simplicity we will use the spherical basis

$$\begin{aligned} \boldsymbol{e}_\pm &= \mp\frac{1}{\sqrt{2}}(\boldsymbol{e}_x \pm i\boldsymbol{e}_y) \\ \boldsymbol{e}_0 &= \boldsymbol{e}_z\,. \end{aligned} \tag{5.2}$$

In which the electrical field components $-,0,+$ in

$$\boldsymbol{E} = (\boldsymbol{e}_-\epsilon_- + \boldsymbol{e}_0\epsilon_0 + \boldsymbol{e}_+\epsilon_+)|\boldsymbol{E}| \tag{5.3}$$

correspond to σ_-, π, σ_+ light. Evidently the polarization vector $\boldsymbol{\epsilon}$ must be normalized to one: $\epsilon_-^2 + \epsilon_0^2 + \epsilon_+^2 = 1$.

In the following, we will discuss transitions with $\Delta m = 0, \pm 1$, which are allowed only for exactly one of the above polarization components. To calculate the Rabi frequency for those individual transitions we can consequently restrict ourself to one of the electric field components and for $k = \pm, 0$ the corresponding Rabi frequencies become

$$\begin{aligned} \Omega &= \frac{\langle f|\, \boldsymbol{E}\boldsymbol{d}\, |i\rangle}{\hbar} \\ \Rightarrow \quad \Omega_k &= \frac{|\boldsymbol{E}|}{\hbar}\epsilon_k \langle f|\, d_k\, |i\rangle \;. \end{aligned} \tag{5.4}$$

And using Equation (5.1)

$$\begin{aligned} \Omega_k &= \frac{|\boldsymbol{E}|}{\hbar}\epsilon_k\tilde{\mathcal{D}} \langle j,m;1,q|j',m'\rangle \\ &= \tilde{\Omega}\,\epsilon_k \langle j,m;1,q|j',m'\rangle \end{aligned} \tag{5.5}$$

with the base Rabi frequency $\tilde{\Omega} = \frac{|\boldsymbol{E}|}{\hbar}\tilde{\mathcal{D}}$. Equation (5.5) has the distinct advantage over Equation (5.4) that we can separate a part common to all field components ($\tilde{\Omega}$) and a part that is specific to each individual one. The individual part can additionally be evaluated straightforwardly using a Glebsch-Gordon coefficient.

5.1.2. $R_\pm$ and Spin State Populations

As shown in Equations (2.14), the probability to find the system in the excited state of a two level system is given by

$$p^{\mathrm{ex}} = \frac{\Omega^2}{4\delta^2 + 2\Omega^2 + \gamma^2} \tag{5.6}$$

if the system is in an equilibrium. Here, transitions of the form $|4^2S_{1/2}, m_j = \pm 1/2\rangle \rightarrow |4^2P_{1/2}, m_j = \pm 1/2\rangle$ are of interest. The excitation probabilities and Rabi frequencies are defined as p_-^{ex}, p_0^{ex}, p_+^{ex} and Ω_-, Ω_0, Ω_+ for $\Delta m_j = -1, 0, +1$ transitions respectively. Using Equation (5.5), we get

$$p_k^{\mathrm{ex}} = \frac{\tilde{\Omega}^2 \epsilon_k^2 c_k^2}{4\delta^2 + 2\tilde{\Omega}^2 \epsilon_k^2 c_k^2 + \gamma^2} \tag{5.7}$$

with $k = -, 0, +$, $c_+^2 = c_-^2 = \langle 1/2, -1/2; 1, 1 | 1/2, 1/2\rangle^2 = 2/3$ and $c_0 = \langle 1/2, 1/2; 1, 0 | 1/2, 1/2\rangle^2 = 1/3$.

The rate in which population in transferred from the $m_j = -1/2$ to the $m_j = +1/2$ ($m_j = +1/2$ to the $m_j = -1/2$) state R_+ (R_-) is

$$\begin{aligned} R_+ &= \gamma_{PS}(p_+^{\mathrm{ex}} p_0^{\mathrm{dec}} + p_0^{\mathrm{ex}} p_-^{\mathrm{dec}}) \\ R_- &= \gamma_{PS}(p_-^{\mathrm{ex}} p_0^{\mathrm{dec}} + p_0^{\mathrm{ex}} p_+^{\mathrm{dec}}) \,. \end{aligned} \tag{5.8}$$

The decay probability p_k^{dec} is also proportional to the dipole matrix element so we get

$$\begin{aligned} p_\pm^{\mathrm{dec}} &= \frac{c_\pm^2}{c_\pm^2 + c_0^2} = c_\pm^2 = \frac{2}{3} \\ p_0^{\mathrm{dec}} &= \frac{c_0^2}{c_\pm^2 + c_0^2} = c_0^2 = \frac{1}{3} \,. \end{aligned} \tag{5.9}$$

We will first restrict ourselves to the case of pure σ_+ polarization. This simplifies the expressions above to

$$\begin{aligned} R_+ &= \gamma_{PS} \frac{\tilde{\Omega}^2 c_+^2 c_0^2}{4\delta^2 + 2\tilde{\Omega}^2 c_+^2 + \gamma^2} \\ R_- &= 0 \end{aligned} \tag{5.10}$$

as $\epsilon_+ = 1$ and $\epsilon_0 = \epsilon_- = 0$ in this case.

Additionally to the $4S_{1/2} \leftrightarrow 4P_{1/2}$ transition the decay channel $4P_{1/2} \rightarrow 3D_{3/2}$ needs to be taken into account. The rate R_D at which population is transferred from $|4^2S_{1/2}, m_j = -1/2\rangle$ to the $D_{3/2}$ manifold can be derived completely analogous to the case discussed above for the $S \rightarrow P$ transition. We then get

$$R_D = \gamma_{PD}\, p_+^{\mathrm{ex}} = \gamma_{PD} \frac{\tilde{\Omega}^2 c_+^2}{4\delta^2 + 2\tilde{\Omega}^2 c_+^2 + \gamma^2} \tag{5.11}$$

The total rate at which population is transferred away from the $|4^2S_{1/2}, m_j = -1/2\rangle$ is then

$$\begin{aligned} R_{\text{tot}} &= R_+ + R_D \\ &= \left(\gamma_{PS} c_0^2 + \gamma_{PD}\right) \frac{\tilde{\Omega}^2 c_+^2}{4\delta^2 + 2\tilde{\Omega}^2 c_+^2 + \gamma^2} \\ &= (1+b)\, R_+ \end{aligned} \tag{5.12}$$

with the branching ratio $b = \frac{\gamma_{PD}}{\gamma_{PS} c_0^2}$.

State Population

The rates determined above, can now be used to set up rate equations for the state population $p_\downarrow$ ($p_\uparrow$) of the $|4^2S_{1/2}, m_j = -1/2\rangle$ ($|4^2S_{1/2}, m_j = +1/2\rangle$) state

$$\begin{aligned} \dot{p}_\downarrow(t) &= -R_{\text{tot}} p_\downarrow(t) \\ \dot{p}_\uparrow(t) &= R_+ p_\downarrow(t) \end{aligned} \tag{5.13}$$

which can easily be solved for the starting conditions $p_\downarrow(0) = 1$ and $p_\uparrow(0) = 0$:

$$p_\downarrow(t) = e^{-R_{\text{tot}} t} \tag{5.14}$$

$$\begin{aligned} p_\uparrow(t) &= \frac{R_+}{R_{\text{tot}}} \left(1 - e^{-R_{\text{tot}} t}\right) \\ &= \frac{1}{1+b} \left(1 - e^{-R_{\text{tot}} t}\right) \end{aligned} \tag{5.15}$$

Pure π Polarization

The case of pure π polarized light driving $\Delta m_j = 0$ transitions can be derived essentially analogous to the case of σ_+ polarized light discussed above. The two possible π transitions have different resonant frequencies ω_+ and ω_- for the $m_j = +1/2 \rightarrow +1/2$ and $m_j = -1/2 \rightarrow -1/2$ transition respectively. The spin-flip rates become

$$\begin{aligned} R_\pm &= \gamma_{PS} p_{0,\mp}^{\text{ex}} p_\pm^{\text{dec}} \\ &= \gamma_{PS} p_{0,\mp}^{\text{ex}} c_\pm^2 , \end{aligned} \tag{5.16}$$

where $p_{0,\mp}^{\text{ex}}$ is the probability for being in the excited $m_j = \mp 1/2$ level. By again using Equations (2.14) we obtain

$$R_\pm = \gamma_{PS} \frac{\tilde{\Omega}^2 c_+^2 c_0^2}{4(\omega - \omega_\mp)^2 + 2\tilde{\Omega}^2 c_0^2 + \gamma^2} \tag{5.17}$$

and for the branching rate in to the $D_{3/2}$ state

$$R_{D,\pm} = \gamma_{PD}\, p_{0,\mp}^{\text{ex}} = \gamma_{PD} \frac{\tilde{\Omega}^2 c_0^2}{4(\omega - \omega_\mp)^2 + 2\tilde{\Omega}^2 c_0^2 + \gamma^2} , \tag{5.18}$$

which yields the total spin-state depletion rates

$$\begin{aligned} R_{\text{tot},\pm} &= R_\pm + R_D \\ &= \left(\gamma_{PS} c_+^2 + \gamma_{PD}\right) \frac{\tilde{\Omega}^2 c_0^2}{4(\omega - \omega_\mp)^2 + 2\tilde{\Omega}^2 c_0^2 + \gamma^2} \\ &= \left(1 + b'\right) R_\pm \,, \end{aligned} \tag{5.19}$$

with the branching ratio

$$b' = \frac{\gamma_{PD}}{\gamma_{PS} c_+^2} \,. \tag{5.20}$$

The rate equations for the two spin-states

$$\begin{aligned} \dot{p}_\downarrow(t) &= -(1+b')R_+ p_\downarrow(t) + R_- p_\uparrow(t) \\ \dot{p}_\uparrow(t) &= -(1+b')R_- p_\uparrow(t) + R_+ p_\downarrow(t) \end{aligned} \tag{5.21}$$

can then be solved for the probability to be in the $|\uparrow\rangle$ level after a scattering time t and the initial condition $p_\uparrow(0) = 0$ and $p_\downarrow(0) = 1$:

$$p_\uparrow(t) = \frac{2}{\tilde{R}} e^{-\bar{R}t/2} R_+ \sinh(\tilde{R}t/2) \tag{5.22}$$

where the new quantities

$$\begin{aligned} \bar{R} &= R_{\text{tot},+} + R_{\text{tot},-} \\ \text{and} \quad \tilde{R}^2 &= \bar{R}^2 - 4b'(2+b')R_- R_+ \end{aligned} \tag{5.23}$$

have been introduced.

5.2. Spin State Detection and Preparation

To be able to measure the populations $p_\uparrow$ and $p_\downarrow$ for the two levels of the $4S_{1/2}$ groundstate, population shelving and fluorescence detection are used. The objective is to transfer the population from only one of the two levels into a meta-stable state (shelving) and subsequently detect fluorescence upon driving the $4S_{1/2} \leftrightarrow 4P_{1/2}$ transition, as depicted in Figure 5.2. In this experiment we use the 729 nm quadrupole transition from $|4S_{1/2}\rangle$ to $|3D_{5/2}\rangle$ for the shelving process. Due to the long life time of the $|3D_{5/2}\rangle$ state, the transitions are sufficiently narrow in frequency to address the two magnetic sublevels separately, which have a Zeeman splitting of approximately 10 MHz. Using RAP pulses [37] the population from the $|4S_{1/2}, m_j = +1/2\rangle$ state is transferred to the $m_j = +1/2$ and $m_j = -3/2$ states of the $|3D_{5/2}\rangle$ state. RAP pulses are used as the population transfer is significantly less sensitive to laser power and frequency fluctuations as compared to e.g. simple π-pulses. We can now drive the $|4S_{1/2}\rangle \leftrightarrow |4P_{1/2}\rangle$ transition using a 397 nm laser and detect the fluorescence light using a photomultiplier tube (PMT). If the population was in $m_j = +1/2$ before, no resonance fluorescence will be detected, while

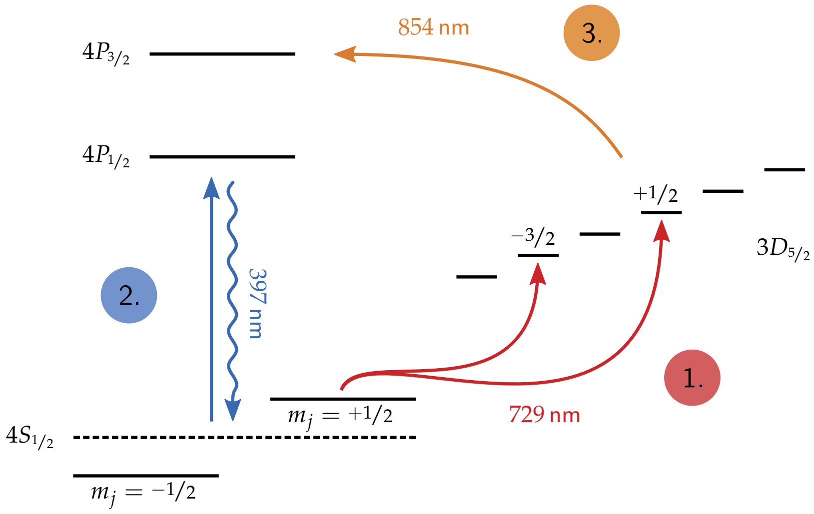

Figure 5.2.: Illustration of the spin state detection. First, population from the $m_j = +1/2$ state is transferred ("shelving") to the $|3D_{5/2}\rangle$ state (to $m_j = -3/2, +1/2$) using rapid adiabatic passage (RAP) pulses. Second, fluorescence on the $|4S_{1/2}\rangle \leftrightarrow |4P_{1/2}\rangle$ is measured. Only if the $m_j = -1/2$ state has been populated fluorescence will be detected. The spin state measurement has therefore been mapped to a dark-bright measurement. Finally, after the detection, 854 nm light transfers the shelved population to the $|4P_{3/2}\rangle$ state where it decays back to the $|4S_{1/2}\rangle$ ground state.

emitted photons will be detected if it was in $m_j = -1/2$. Thus, the spin discrimination measurement has been mapped to a simple dark-bright discrimination. Resetting of the state before the subsequent measurement cycle is accomplished by illuminating the ion with 854 nm light, driving the population to the $|4P_{3/2}\rangle$ state from where it can decay back to $|4S_{1/2}\rangle$. This measurement is repeated e.g. 100 times for fixed parameters such as scattering pulse time or detuning to infer the occupation probabilities of the spin levels after the scattering pulse. Obviously, the more measurement repetitions the smaller the uncertainty of the population (uncertainty $\propto 1/\sqrt{\text{repetitions}}$).

For initialization of the spin at the beginning of a measurement cycle, we use optical pumping. By subsequently driving the 729 nm quadrupole transition and the 854 nm repumping (see Figure 5.2) we systematically deplete one of the $|4S_{1/2}\rangle$ m_j levels and pump population into the other one. As above for the detection, RAP pulses are used for robust transfer to $|3D_{5/2}\rangle$. Occupation probabilities above 99.9 % can be achieved by this pumping scheme [27].

5.3. Measuring Spin-Flip Rates - Calibrating Laser Parameters

In this section, we will use the spin-flip rates derived in Section 5.1 to measure the intensity and detuning of the 397 nm beams. The goal of this measurement is to calibrate the values of the beams set in the lab, i.e. the intensity via photo diode voltages and the detuning via AOM frequencies, to resonant saturation parameters and detunings relative to the atomic dipole transition. The experiment sequence is depicted in Figure 5.3. After

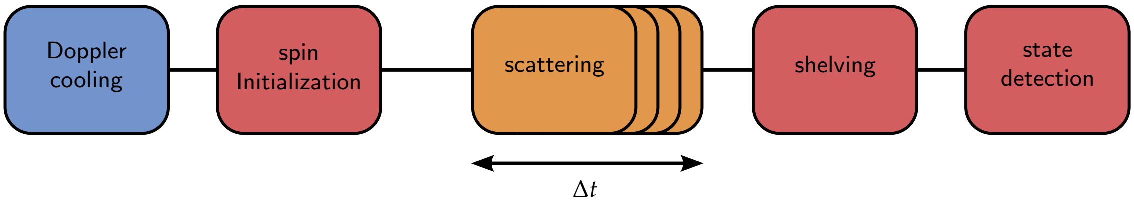

Figure 5.3.: Sequence to measure the spin-flip rate. After Doppler cooling and spin initialization to the $|\downarrow\rangle$ state, the laser of which detuning and power need to be calibrated, is switched on. During this scattering time, population is transferred to $|\uparrow\rangle$. Spin dependent shelving to a metastable state and subsequent fluorescence detection then determines the probability to be in the $|\uparrow\rangle$ state and thus the amount of scattered light.

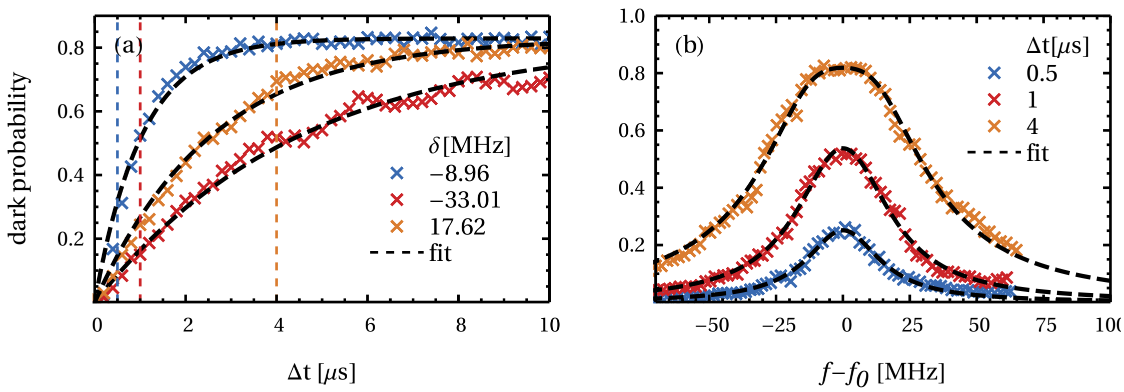

Figure 5.4.: Measurements of laser-induced spin population depletion for the Sigma beam, the dark probability is equal to $p_\uparrow$. Both panels show the population in $|\uparrow\rangle$ after initialization in $|\downarrow\rangle$ and exposure to the Sigma beam. (a) shows populations versus the scattering time Δt for different AOM frequencies and at fixed intensity, while (b) shows the populations versus AOM frequency for different scattering pulse times and fixed intensity (f_0 is the fitted resonance frequency). The vertical dashed lines in (a) correspond to the pulse times Δt which are used in (b). The black dashed curves are fits to Equation (5.24). The data in panel (b) allows for accurate calibration of the laser detuning δ in terms of the AOM frequency.

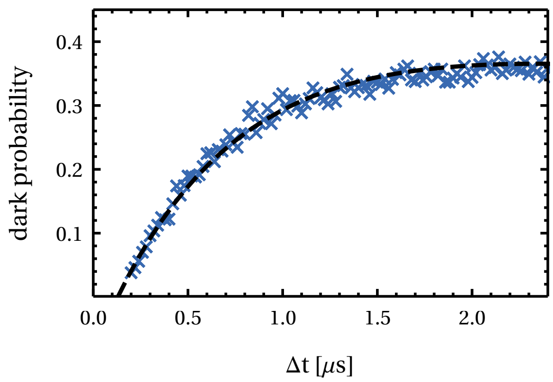

Figure 5.5.: Measurements of laser-induced spin population depletion for the Doppler beam, the dark probability is equal to $p_\uparrow$. As the Doppler beam is used for detection, the frequency can not be easily scanned as compared to the measurements in Figure 5.4(b). Using the detuning determined from spectra of the Sigma beam, the Rabi frequency of the Doppler beam can be computed using a fit to Equation (5.22) (dashed curve). An additional offset t' in Δt was used to fit the data.

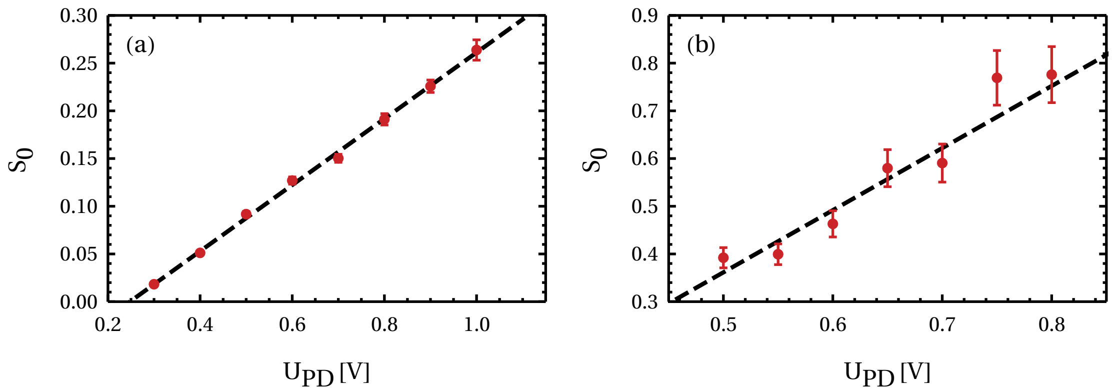

Figure 5.6.: Calibration of the saturation parameter S_0 versus the voltage U_{PD} of the photo diode for the Sigma beam in (a) and the Doppler beam in (b). Note that U_{PD} is not the voltage during the scattering pulse, the intensity is first set to the given voltage before the electro optical modulator (EOM) attenuates the intensity for the experiment. (a) Relative uncertainty of the slope 1.6 % and the y-axis intersection 2.8 %. (b) Relative uncertainty of the slope 28 % and the y-axis intersection 11 %.

Doppler cooling [23, 24] on the 397 nm $S_{1/2} \leftrightarrow P_{1/2}$ transition, the spin is initialized as described in Section 5.2. In all experiments discussed here, pumping to $|\downarrow\rangle$ is used. Starting in $|\downarrow\rangle$, the laser, of which detuning and power need to be calibrated, is switched on for some time Δt, leading to population transfer to $|\uparrow\rangle$. The spin populations can subsequently be measured using the method described in Section 5.2.

As derived in Section 5.1, the probability to be in $|\uparrow\rangle$ after initialization to $|\downarrow\rangle$ and scattering with a σ_+ polarized light field for a time Δt with the reduced Rabi frequency $\tilde{\Omega}$ and detuning δ is

$$p_\uparrow = \frac{1}{1+b}\left(1 - e^{-R_{\mathrm{tot}}\Delta t}\right), \tag{5.24}$$

with the rate

$$R_{\mathrm{tot}} = (1+b)\,\gamma_{PS}\frac{\tilde{\Omega}^2 c_+^2 c_0^2}{4\delta^2 + 2\tilde{\Omega}^2 c_+^2 + \gamma^2}, \tag{5.25}$$

at which population is depleted from the $|\downarrow\rangle$ state. If $p_\uparrow$ is now measured versus Δt for fixed laser intensity and detuning, we observe an exponential behavior as depicted in Figure 5.4 (a). The larger the detuning from resonance δ, the smaller R_{tot} and hence the depletion of the initial spin level. We can therefore choose an appropriate Δt and scan the detuning to obtain the line shape as depicted in Figure 5.4 (b). By fitting Equation (5.24) to the measured data the reduced Rabi frequency $\tilde{\Omega}$, and therefore the resonant scattering parameter S_0, and the AOM frequency corresponding to $\delta = 0$ can be determined.

The ion oscillator clock is driven by two laser beams (Doppler and Sigma), both of which have to be calibrated. Their frequencies are controlled with two different AOMs and have different polarization. The Sigma beam is σ_+ polarized and therefore drives $\Delta m_j = +1$ transitions as discussed above. The Doppler beam is π polarized and therefore drives $\Delta m_j = 0$ transitions. The cooling and detection are done using the Doppler beam. The Sigma beam can therefore be easily characterized, as the Doppler settings (i.e. frequency and intensity) can remain fixed throughout the sequence. For characterizing the Doppler beam however, its frequency and intensity would need to be changed between the detection and characterization settings which is not possible with the current control infrastructure. To avoid this issue, the scheme to calibrate both beams consist of two steps: First, the Sigma beams intensity and frequency are determined as discussed above. As both beams are derived from the same laser and are detuned from the original laser frequency with different AOMs, the detuning calibration is identical for both beams. Second, $p_\uparrow$ is measured versus Δt as depicted in Figure 5.5. With the known detuning this data can then be fitted to Equation (5.22) in order to determine the Doppler beam's Rabi frequency.

One difficulty we encounter when fitting the measured data to Equation (5.24) is the fact that the measured linewidth is broader then the natural linewidth. The the FWHM of the $\Delta t = 1\,\mu\mathrm{s}$ line depicted in Figure 5.4 (b) is $2\pi \times 32.30(55)$ MHz and thus much broader than expected due to saturation broadening alone [1] . However, the data matches

[1]The natural linewidth is $\gamma = 2\pi \times 21.578$ MHz and the saturation broadened full width at half maximum (FWHM), using the measured Ω, is $\sqrt{\gamma^2 + 2\Omega^2} = 2\pi \times 21.999$ MHz.

a Lorentzian line (reduced $R^2 = 0.996$) which eliminates Doppler broadening as a cause. Doppler broadening, and all other Gaussian broadening mechanism, would lead to a change in line shape to a Voigt profile which could be distinguished from a Lorentzian at the amount of broadening present in the data. So far, no satisfactory explanation for this line broadening could be found.

In the following, we will assume a Lorentzian broadening mechanism with a FWHM of 2ξ, which simply adds to the FWHM of Equation (5.25). Instead of the Lorentzian in Equation (5.25) with a FWHM of $\sqrt{\gamma^2 + 2\Omega^2}$ we will therefore us a Lorentzian of FWHM $\sqrt{\gamma^2 + 2\Omega^2} + 2\xi$. It is important to note that this purely phenomenological.

Using this method, the saturation parameter for the Doppler and the Sigma beam can be measured versus the voltage of a photo diode as depicted in Figure 5.6. The photo diodes can only measure light intensities above a certain threshold. As we want to use light intensities below this threshold, an EOM is used together with a $\lambda/2$ plate to attenuate the beams. The intensities are first set using the unattenuated beams before switching on the attenuation for the scattering measurement.

The connection between the two quantities is linear in good approximation, which is to be expected as both the voltage of the photo diode and the saturation parameter are proportional to the light intensity. The data is therefore fitted to a linear function. For the Sigma beam the calibration works relatively well, the relative uncertainties for the fitted slope and y-axis intersection are in the order of few percent. The uncertainties of the individual points for the Doppler calibration are significantly larger and also the fitted parameters have relative uncertainties of well above 10 %. This can be attributed to the different methods that have been used for the two beams as described above.

The fitted photo diode calibration can then be used in further experiments to determine the saturation parameter for arbitrary photo diode voltages. Different EOM attenuations have been used in some cases. There, the calibration is simply extended by multiplying the saturation parameter with the ratio of the attenuation used in the calibration measurement and the current one.

To determine the detuning of a beam using a calibration measurement one has to be aware of the different transitions, and therefore the different resonance frequencies, which are involved. The frequency calibration is done using spectra of the Sigma beam as depicted in Figure 5.4 (b) and consequently we obtain the resonance frequency of the σ_+ transition which we are going to call $\omega_{\sigma+}$ in the following. For the Doppler beam there are two involved transitions with the resonant frequencies ω_+ and ω_- for the $m_j = {}^{+1}/_{2} \rightarrow {}^{+1}/_{2}$ and $m_j = {}^{-1}/_{2} \rightarrow {}^{-1}/_{2}$ transition respectively. They are different due to the different Zeeman splittings of ground and exited states Δ_g and Δ_e which are given by

$$\Delta_{g,e} = g_{g,e} \frac{\mu_B}{\hbar} B \tag{5.26}$$

where g_g and g_e are the Landé factors of the ground and exited states and B is the magnetic field (see also Figure 5.1). Δ_g is known to be approximately $2\pi \times 9.6\,\text{MHz}$ for the used magnetic field. Therefore we can calculate $\Delta_e = g_e/g_g\,\Delta_g = 1/3\,\Delta_g$ and find the two π transition frequencies relevant for the Doppler beam [2]

$$\begin{aligned} \omega_+ &= \omega_{\sigma+} - \Delta_g \\ \omega_- &= \omega_{\sigma+} - \Delta_e\,. \end{aligned} \tag{5.27}$$

For the measurements in Chapter 6 we want to determine the dimensionless detunings as defined in Equations (2.50) which become

$$\begin{aligned} \alpha_{\sigma+} &= 2\frac{\omega - \omega_{\sigma+}}{\gamma} \\ \alpha_+ &= 2\frac{\omega - (\omega_{\sigma+} - \Delta_g)}{\gamma} \\ \alpha_- &= 2\frac{\omega - (\omega_{\sigma+} - \Delta_e)}{\gamma} \end{aligned} \tag{5.28}$$

In Chapter 6 we will talk about cooling and amplification beams rather then Doppler and Sigma beams and therefore we will use different terms with the corresponding indices $\alpha_c = \alpha_{\sigma+}$, $\alpha_{a+} = \alpha_+$ and $\alpha_{a-} = \alpha_-$.

[2]For the σ_- transition the frequency is $\omega_{\sigma-} = \omega_{\sigma+} - \Delta_g - \Delta_e$, this transition will however not be needed in the following.

6. Oscillation Stability Measurements

In this chapter we will discuss the measurement of the stability of the phonon laser clock. Viewing the ion as a pendulum of a clock, we want to measure the oscillation stability to infer its capability to serve as a time keeping device. Using the amount of scattered photons as our measure for waste heat production of the system, we then can investigate connections between the oscillation stability and the scattering rate and compare it to the findings discussed in Section 1.1.

We will discuss the experimental implementation of the ion oscillator in Section 6.1. In Section 6.2 we will describe how the oscillation of the ion can be detected via the scattered photons and subsequently in Section 6.3 how we can use these measurement to evaluate the oscillation stability of the ion. Finally in Section 6.4, measurements of the oscillation stability and connections to the laser operation parameters and the scattering rate are presented.

6.1. The System

In the experiment presented here, the $^{40}\mathrm{Ca}^+$ $4S_{1/2} \leftrightarrow 4P_{1/2}$ electric dipole transition is used to drive the oscillation. A 397 nm laser beam (Section 3.2) is split into two individual beams which are each shifted in frequency using a double pass acousto-optical modulator (AOM) configuration. The red detuned beam is σ_+ polarized and is therefore called Sigma or cooling beam. The blue detuned beam is π polarized and is called Doppler or amplification beam in the following [1]. The components of the wave vectors of these two beams have equal sign along the trap axis and opposite sign perpendicular to the trap axis (see Figure 1.5 and Figure 3.2 for the beam geometry). This beam geometry excludes undesired oscillation on the radial modes of vibration.

Ideally, one would use an isolated two-level system or at least a closed transition where no additional decay channels are present. This case is considered in the theory in Section 2.2. Unfortunately, this is not possible using the $4S_{1/2} \leftrightarrow 4P_{1/2}$ transition, as both levels are split into two Zeeman substates. In total we have thus four levels and due to the light polarizations three driven transitions (two π transitions and one $\sigma+$ transition). For arbitrary operation regimes it is not completely clear how this deviation from the model system will affect the measurements. However, we assume that the system is still qualitatively similar to the idealized case discussed in Section 2.2. The difference is particularly small if the number of scattered photons per oscillation cycle is $\ll 1$. In this case none of the sublevels are depleted by optical pumping and the scattering rates

[1] This beam is used for Doppler cooling in other experiments, hence the name.

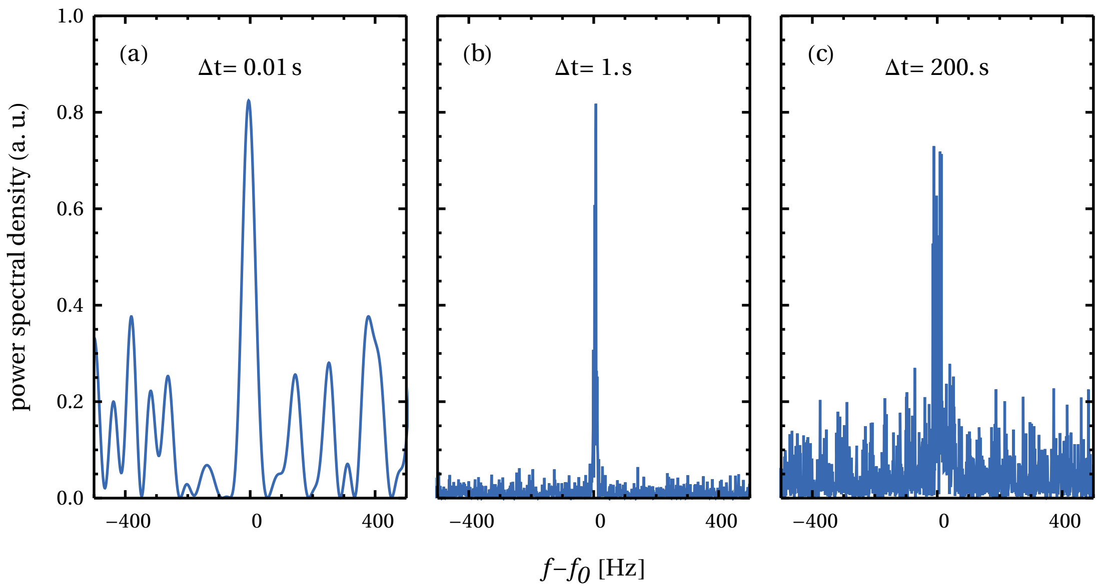

Figure 6.1.: Power spectral density as computed from the photon time stamps measured during ion oscillation. f_0 is the frequency of maximal power spectral density, determined from this data, it is $f_0 = 2 \times 1.484\,89\,\mathrm{MHz}$ (two times the axial trap frequency). The three panels correspond to different acquisition times Δt. (a) For small Δt, the peak is Fourier limited with a full width at half maximum (FWHM) of $\approx 1/\Delta t = 100\,\mathrm{Hz}$ and the peak is not very well distinguishable from the noise floor. (b) For medium Δt in the range of seconds, the peak becomes well pronounced and narrow (FWHM$\approx$ 10 Hz at $\Delta t = 1\,\mathrm{s}$). (c) For large times technical noise will lead to a broadening of the peak. *Note:* The power spectral density scale is chosen differently for the three plots, it decreases rapidly with Δt.

on the different transitions are independent, effectively giving similar behavior as for a two-level system. In the outlook in Chapter 8 we will propose a possibility to prevent those problems in future experiments.

Additionally to the decay into different Zeeman substates, decay into the metastable $3D_{3/2}$ state is possible from $4P_{1/2}$. It is therefore necessary, to use an additional 866 nm repumping laser (Section 3.2) driving the $3D_{3/2} \leftrightarrow 4P_{1/2}$ transition.

6.2. Detecting the Oscillation Frequency

We investigate the phonon laser oscillation stability by detecting the photons scattered by the ion. The 397 nm light does not only serve the purpose of supplying the energy needed for sustained oscillation but also enables the detection of the velocity modulation via the scattered photons. As the lasers are resonant with the dipole transition only for a certain velocity due to the Doppler shift, photons will only be scattered if the ion is at a certain point in its oscillation cycle. There will thus be two points per oscillation period for each laser for which the light is in resonance with the transition as depicted in Figure 2.7. The scattering rate will therefore have the periodicity of the ion oscillation and a Fourier analysis of the scattering rate will show components at the oscillation frequency and its integer multiples. There is one main peak for each beam per oscillation cycle which makes the Fourier component at twice the oscillation frequency the most pronounced as can be observed in Figure C.1

The scattered photons are measured using a photomultiplier tube (PMT) connected to a time tagging module (see Section 3.3). The acquired data are time stamps of the photon arrivals at the PMT. The simplest approach to compute the frequency spectrum of the ion oscillation is to perform a Fourier transform of these time stamps.

For a continuous signal $f(t)$ in the time domain the Fourier transform is defined as

$$\hat{f}(\omega) = \mathcal{F}(f)(\omega) = \int_{-\infty}^{\infty} \mathrm{d}t f(t) e^{-i\omega t} \tag{6.1}$$

The problem in our case, is that the signal consists of discrete time stamps instead of an continuous signal or a discrete signal at equally spaced points in time. To get an estimator for the Fourier transform of our time stamps we will use the (mathematically not so rigorous) assumption that the signal consists of δ-peaks at the the time stamps. If the signal consists of time stamps t_i, $i = 1, \ldots, N$ our continuous signal then becomes

$$f(t) = \sum_{i=1}^{N} \delta(t - t_i) \tag{6.2}$$

for which the Fourier transform is

$$\begin{aligned} \hat{f}(\omega) = \mathcal{F}(f)(\omega) &= \int_{-\infty}^{\infty} \mathrm{d}t f(t) e^{-i\omega t} \\ &= \sum_{i=1}^{N} \int_{-\infty}^{\infty} \mathrm{d}t \delta(t - t_i) e^{-i\omega t} \\ &= \sum_{i=1}^{N} e^{-i\omega t_i} . \end{aligned} \tag{6.3}$$

Example plots of spectra obtained by this method are depicted in Figure 6.1. Computing the Fourier transform of the time stamps in this manner becomes particularly useful later on, when we perform computations on subsets of the acquired data, i.e. for different count intervals Δt or count event numbers N. Here, we compute the complex numbers $\exp(-i\omega t_i)$ once for a given data set, and then compute Fourier transforms for a given subset by summing over it.

6.3. Quantifying Oscillation Stability

Up until now, we have discussed how we can determine the frequency spectrum of the ion's motion via the spectrum of the photon time stamps. Our goal is however, to quantify the oscillation stability in order to get a measure of the system's ability to measure time. The most common way of quantifying the stability of clocks is to use frequency samples f_n, $n = 1, \dots, K$ over time and compute the Allan variance [38]

$$\sigma_y^2(\tau) = \frac{1}{2}\langle(\bar{y}_{n+1} - \bar{y}_n)^2\rangle\,, \tag{6.4}$$

where $\bar{y}_n$ are the clocks fractional frequencies defined as

$$\begin{aligned} \bar{y}_n &\equiv \frac{\bar{f}_n - f_0}{f_0} \\ \bar{f}_n &\equiv \langle f \rangle_\tau \end{aligned} \tag{6.5}$$

with the time average $\langle\cdot\rangle_\tau$ over the n-th interval of duration τ. The Allan variance quantifies the variation of the frequency samples as a function of the averaging period τ. It can not just be viewed as a single value for the frequency stability but rather as a whole function characterizing the noise sources affecting the clock. An exemplary Allan variance is depicted in Figure 6.3. We can clearly see that the Allan variance decreases for increasing τ up to some minimal value τ_{min} before it increases approximately linearly. This can be explained with different frequency components of the noise: For small τ the Allan variance is dominated by high-frequency noise. In our case, this consists of shot noise, i.e. the Fourier limit arising from the limited number of detection events during the respective time interval, in combination with the finite emission phase windows (see Section 2.2.5) and technical noise at high frequencies. If the averaging time τ increases, this high frequency noise is averaged out and the Allan variance decreases. For large τ low frequency noise is dominant and the Allan variance will increase for increasing τ. We will now define more precisely what we mean by low and high frequency noise and how the Allan variance behaves for different types of noise.

6.3.1. Allan Variance for Different Noise Components

In the course of evaluating the oscillation stability of the ion we want to separate different sources of noise. The Allan variance is a suitable tool to achieve this, as different types of noise will lead to different behavior in its scaling as already outlined above. We will use a power law as an approximation of the power spectral density S_y of the frequency noise:

$$S_y(f) = \sum_{\alpha=-2}^{2} h_\alpha f^\alpha \tag{6.6}$$

The scaling of the Allan variance for these five components are summarized in Table 6.1. We furthermore refer the reader to [39] for a more thorough discussion on the subject. FPM and WPM have very similar scaling and are therefore difficult to distinguish [2]. As we are mainly interested in WPM noise, we will simply assume one component $\propto \tau^{-2}$ and neglect FPM. In the following, we will qualitatively investigate the dependence of

[2] The modified Allan variance [40] can be used to for enhanced distinguishability of these components.

Table 6.1.: Scaling of the Allan variance σ_y^2 for different noise types. $S_y(f)$ is the power spectral density of the fractional frequency. We define new coefficients k_n for qualitative analysis of the noise intensities. Note, that flicker phase modulation (FPM) and white phase modulation (WPM) have very similar scaling behaviors and are therefore difficult to distinguish using the Allan variance. f_h is a cutoff frequency that is defined to limit the non-physical infinite power of white noise. See [39] for a more thorough discussion of this table. For FPM we define $\mathcal{C}_1 = (1.038 + 3\ln(2\pi f_h \tau))/(4\pi^2)$.

$S_y(f)$	Noise	Source	$\sigma_y^2(\tau)$	k_n
$h_{-2}f^{-2}$	random walk frequency modulation (RWFM)	slow trap frequency drift	$k_{-2}\tau^1$	$k_{-2} = \frac{2\pi^2 h_{-2}}{3}$
$h_{-1}f^{-1}$	flicker frequency modulation (FFM)	n/a	$k_{-1}\tau^0$	$k_{-1} = \frac{2h_{-1}}{ln2}$
$h_0 f^0$	white frequency modulation (WFM)/random walk phase modulation (RWPM)	fast trap frequency noise/ photon recoils	$k_0\tau^{-1}$	$k_0 = \frac{h_0}{2}$
$h_1 f^1$	flicker phase modulation (FPM)	n/a	$h_1\,\mathcal{C}_1\tau^{-2}$	
$h_2 f^2$	white phase modulation (WPM)	finite phase emission window, shot noise	$k_2\tau^{-2}$	$k_2 = \frac{2h_2 f_h}{4\pi^2}$

certain noise types and will simply use the coefficients k_n as defined in Table 6.1. To determine these different noise coefficients we will use the model function

$$\sigma_y^2(\tau) = k_2\tau^{-2} + k_0\tau^{-1} + k_{-1} + k_{-2}\tau\,, \tag{6.7}$$

which we can later fit to the measured data.

6.3.2. Computing the Allan Variance from Time Stamps

To compute the Allan variance we use the method described in Section 6.2 to compute frequency samples from the photon time stamps. We need a sequence of time-ordered frequency samples f_n, each pertaining to an interval of duration τ. We therefore divide a measurement of time stamps into intervals of equal duration τ and compute the spectrum for each interval by computing the Fourier transform. The task is now to infer an estimate of f_n from the spectrum. To that end, we choose the frequency pertaining to the maximum power spectral density. This has proven to be a simple, yet reliable method.

For the measurements discussed below, we use photon time stamps acquired over a time in the order of a few minutes (5 min for almost all measurements) and partition them into varying intervals in the range of $\tau = 1 \ldots 500$ ms, for which the oscillation frequencies are computed. As can be seen from the frequency samples depicted in Figure 6.2, these frequencies contain numerous outliers. If the Allan variance would be computed directly from these unfiltered frequency samples it would be dominated by these instead of reflecting a valid measure of the ion's oscillation stability.

There are several reasons for frequency outliers: Depending on the operation parameters, i.e. laser intensities and detunings, the oscillation is so unstable that the ion stops

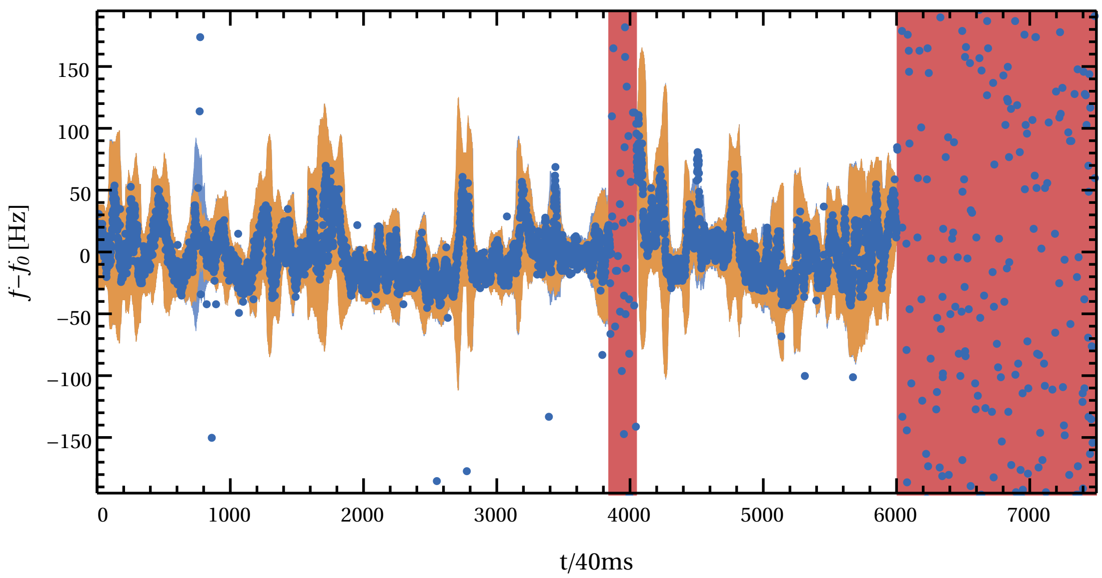

Figure 6.2.: Example plot of the inferred oscillation frequency during a 300 s measurement and the outlier filtering. The data is partitioned in chunks of 40 ms, for each of which the frequency is determined (blue dots). First, areas with exceptionally high standard deviation are removed to exclude chunks where the ion has not been oscillating (red area). Second, interquartile range (IQR) filtering is applied to remove further outliers (blue area) which can be repeated a second time (orange area). 100 frequency samples around an individual point are used to calculate the IQR in this case. f_0 is the mean of the filtered data.

oscillation for some periods of time. Additionally, the method of determining the ion's oscillation frequency is prone to outliers, as the spectral density of some random frequency can exceed the one pertaining to the actual oscillation frequency due to noise. This effect is particularly pronounced for short acquisition times as can be seen from the spectra depicted in Figure 6.1. Evidently, it is necessary to filter these frequency samples to retain only samples corresponding to the actual ion oscillation and consequently an Allan variance that is a satisfactory representation of the oscillation stability.

Time intervals in which no ion oscillation can be detected are filtered out by computing the standard deviation of the frequencies in an appropriate range around this interval. Only if the standard deviation is below a well chosen threshold, the interval will be used for further evaluation. This method filters out contiguous intervals of times where the ion is not oscillating properly (red areas in Figure 6.2). Subsequently, interquartile range (IQR) filtering is used to exclude isolated outliers. This filtering technique is commonly used in different scientific fields. It has the major advantage over methods using mean and standard deviation, of being less dependent on the outliers themselves, the size of the data set and the distribution of the outliers [41, 42]. The latter property is especially important for our case, as the outliers are rather uniformly then normal distributed. The IQR is computed by subtracting the first quartile Q_1 of the data from the third Q_3. We then reject all data points that lie below $Q_1 - 1.5\,\mathrm{IQR}$ or above $Q_3 + 1.5\,\mathrm{IQR}$ [3]. The

[3] The value of 1.5 for the IQR coefficient is relatively arbitrary but widely used in the literature [41].

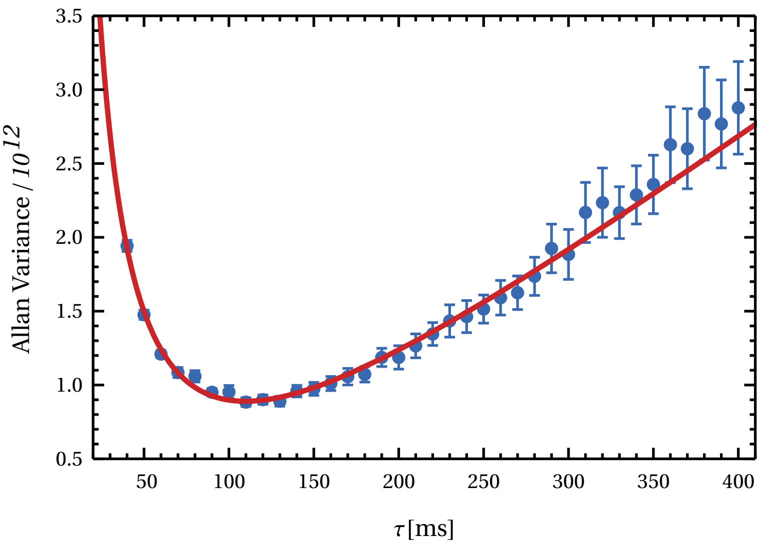

Figure 6.3.: Allan variance of frequency samples generated from photon time stamps during ion oscillation. Error bars are standard errors from the mean of squared frequency differences. The data points are fitted using the model function Equation (6.7) (red curve).

quartiles, and therefore the filtering, are very robust to the values of the outliers and make for a reasonable approach in this case as can be appreciated from the exemplary measurement in Figure 6.2. To account for drifts in frequency, the IQR is computed only in an appropriate range around each point instead of the whole data set.

Once the frequency samples are free from outliers, they can directly be used to compute fractional frequencies, where the nominal frequency f_0 is taken to be the mean of the frequency samples. The Allan variance can then be computed directly from these fractional frequencies. To save computation time, the Fourier transform is not computed independently for every partition of the time stamps into different values of τ. Instead, the Fourier transform is computed once for a partition into intervals of sufficiently small size τ_0. The Fourier transform of intervals of integer multiple lengths of τ_0 can then be efficiently computed by simply taking the sum of the Fourier transform of the subintervals before taking the squared modulus to arrive at the power spectral density.

6.3.3. Evaluating the Allan Variance

When frequency samples f_n over time for different averaging times τ have been acquired, the Allan variance can be computed. We want to evaluate the Allan variance to gain knowledge about the stability of the oscillation. Therefore we use Equation (6.7) to fit the data and infer the noise power coefficients k_n. An exemplary fit is depicted in Figure 6.3. Uncertainties of the Allan variance values are approximated by the standard uncertainty of the mean in Equation (6.4), and the uncertainties of the Allan variance parameters are computed by the fitting algorithm [4]. In the following section we will use this method to evaluate the different noise components for different operation parameters of the phonon laser clock.

6.4. The Phonon Laser Clock at Variable Operation Parameters

In this section, we will discuss the main measurements of this thesis. Time stamps of the photons scattered by the ion during oscillation are measured for different operation parameters. We evaluate the different noise components for these operation parameters and investigate the relation to the total scattering rate. In the experiments, the detunings and the saturation parameters of the amplification (Doppler) and cooling (Sigma) lasers are calibrated using the method described in Chapter 5. As the amplification beam is π polarized, the two transitions $|4S_{1/2}, m_J = -1/2\rangle \leftrightarrow |4P_{1/2}, m_J = -1/2\rangle$ and $|4S_{1/2}, m_J = +1/2\rangle \leftrightarrow |4P_{1/2}, m_J = +1/2\rangle$ are driven at the same time. We therefore specify the detunings α_{a-} and α_{a+} for these two transitions as defined in Section 5.3. In the experiments presented here, we keep the detunings fixed and vary the intensity of the lasers and thus the saturation parameters. We will present the different measurements and their results in this section and discuss them further in Chapter 7.

Linear Scan of the Amplification Saturation Parameter

Figure 6.4 shows the result of a measurement for which the cooling laser power was held fixed, while the amplification power was varied. The power of the laser beams was set during the measurement by adjusting the radio frequency (RF) power supplied to the acousto-optical modulator (AOM) such that the desired intensity, measured via a photo diode, was reached as described in Section 3.3. After the measurement, the voltages of the photo diodes can be converted to the resonant saturation parameters S_a and S_c using the calibration curves depicted in Figure 5.6. An additional spectrum of the cooling (Sigma) beam, analogous to the one depicted in Figure 5.4 (b), was measured to infer the zero detuning AOM frequency for the σ_+ transition which can then be used to calculate the detunings relative to all other relevant transitions as described in Section 5.3. We find that the cooling detuning was $\alpha_c = -6.4$ and the amplification detunings where $\alpha_{a-} = -0.47$ and $\alpha_{a+} = 0.12$ for the two π transitions. Hence the amplification laser was blue detuned relative to only one of the two transitions.

The plots show the values of the different noise coefficients of the Allan variance defined in Table 6.1. Each point in the plots corresponds to a 5 min acquisition of photon detection times for a given value of the amplification laser power. These time stamps are then partitioned into 15 000 intervals of 20 ms duration from which a time series of oscillation frequencies is obtained according to Section 6.2. After removing outliers as described in Section 6.3.2 the Allan variances are computed and fitted to Equation (6.7), analogous

[4] Mathematicas `NonLinearModelFit` function was used. Weights are taken to be $1/\text{uncertainty}^2$ for the individual points and using the correct `VarianceEstimatorFunction` yields faithful uncertainties for the fitted parameters.

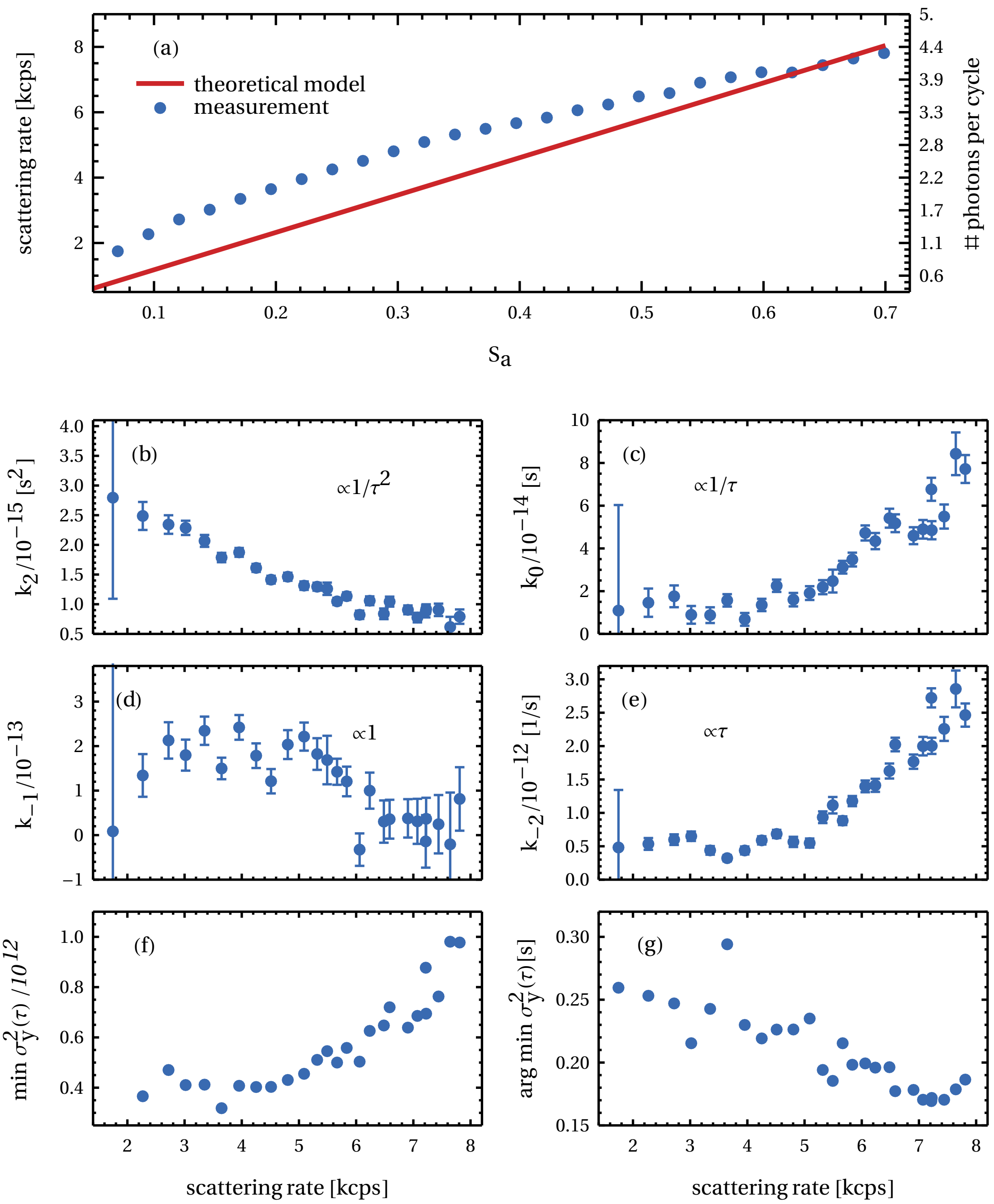

Figure 6.4.: Evaluation of a single S_a scan ($S_c = 0.13$, $S_a = 0.06 \ldots 0.7$, $\alpha_c = -6.4$, $\alpha_{a-} = -0.47$, $\alpha_{a+} = 0.12$). The intensity of the amplification beam was scanned while the intensity of the cooling beam was held fixed. (a) Shows the scattering rate over the resonant saturation parameter S_a. Due to the long acquisition times the uncertainties are small and are not depicted in the plot. The number of photons scattered by the ion is additionally calculated as described in the text and the theoretical curve is computed using the operation parameters. (b)-(e) Show the fit parameters of the Allan variance to the model Equation (6.7), the inset τ dependencies are the scalings of the Allan variance for the corresponding coefficients. (f) and (g) are the minimal value of the Allan variance ($\min \sigma_y^2(\tau)$) and the value of τ at that point ($\arg\min \sigma_y^2(\tau)$) respectively. (measurement from 05.11.2018)

to Figure 6.3. This yields the coefficients k_n which are plotted versus the scattering rate to investigate connections to the waste heat production. In addition, the mean number of photons scattered by the ion per oscillation cycle is computed by taking the detected scattering rate, dividing it by the detection efficiency and multiplying it with the duration of one cycle.

We now discuss the different panels in Figure 6.4:

(a) shows the scattering rate versus the amplification saturation parameter S_a over which it increases monotonously. Also the corresponding number of photons that are scattered by the ion per oscillation cycle are depicted. To compare this measurement to the theory we compute the operating point amplitude β_{OP} numerically from the saturation parameters and detunings as described in Section 2.2.3 and calculate the number of scattered photons per oscillation cycle using Equation (2.56). Obviously, the measurement fits the theory reasonably well.

(b) shows k_2 which is the coefficient of the $1/\tau^2$ component of the Allan variance. It is proportional to white phase modulation (WPM), which we connected to the finite width of the scattering peak in Section 2.2.5. From the theory we would expect the intensity of the WPM to increase with the scattering rate due to a broader scattering peak at higher saturation parameters. Obviously, this is not the case in the measurement, where k_2 decreases approximately linearly over the scattering rate.

(c) shows k_0 which is the coefficient of the $1/\tau$ component of the Allan variance. This coefficient is proportional to the random walk phase modulation (RWPM) intensity, which is equal to white frequency modulation (WFM). There should consequently be a contribution due to technical white noise on the trap frequency leading to WFM and a contribution due to phase diffusion leading to RWPM. The part corresponding to the technical noise should be independent of S_a and, up to a constant, the behavior we observe in the measurement should be only due to the phase diffusion. We see from the plot that after a relatively constant region, k_0 increases approximately linearly with the scattering rate. This directly contradicts the prediction of the theory depicted in Figure 2.9, where the phase diffusion coefficient decreases with increasing S_a. Consequently, in this case higher waste heat production corresponds with an increase in phase diffusion.

(d) shows the part proportional to flicker frequency modulation (FFM) for which we do not have an immediate source. The values are however significantly different from zero. Also they do not change much with the scattering rate which could point to a purely technical source of FFM which is not connected to the phase stability of the ion oscillation.

(e) shows k_{-2}, the part proportional to the random walk frequency modulation (RWFM) intensity, which should corresponds to long term drifts in the trapping frequency due to technical imperfections. However, k_{-2} strongly depends on the scattering rate, and therefore on S_a in this measurement. Furthermore, it behaves very similarly to k_0. This must mean that not only technical sources of noise contribute to the value of k_{-2}.

(f) shows the minimum of the Allan variance. It can be seen as a general measure of the frequency stability. Just like k_{-2} it behaves very similarly to the k_0 part and increases with the scattering rate. The clock stability consequently decreases with the scattering rate.

(g) shows the value of τ at which the minimum occurs. It decreases slightly with the scattering rate.

2D Scan of Saturation Parameters

In this measurement, we characterize the oscillation stability versus varying amplification *and* cooling saturation parameters, at fixed detunings as depicted in Figure 6.5. The measurement and parameter calibration was performed identically to the measurement presented above. Here, the cooling detuning was $\alpha_c = -6.3$ and the amplification detunings where $\alpha_{a-} = -0.81$ and $\alpha_{a+} = -0.21$ for the two π transitions. According to this calibration the amplification laser was therefore red detuned. According to the theoretical model no stable oscillation should be possible in this case. We attribute the fact that stable oscillation can nevertheless be observed to the discrepency between the theoretetical model and the actual system which will be further discussed in Chapter 8. Also we observe striking similarities between this measurement and the one discussed above for the linear scan of the amplification intensity for which one of the amplification detunings was positive and therefore blue detuned. Points for which the fit of the Allan variance failed or the oscillation was extremely unstable have been filtered out and are marked by grey squares (see also Figure C.3 to get an impression of the frequency stability).

The interpretation of the results is rather complicated using the heatmaps in Figure 6.5. We will therefore discuss the plots in Figure 6.6 and Figure 6.7. Here, specific regions of saturation parameters have been selected, for which the coefficients k_n are plotted over the corresponding scattering rate. See also Figure C.2 for analogous plots over the entire region of saturation parameters.

Figure 6.5 (a) depicts the scattering rate during oscillation over S_a and S_c. As in Figure 6.4 (a), it increases monotonously with the saturation parameters. Using the grey, filtered out points we can observe the region of stable oscillation similar to the one predicted by the theory and depicted in Figure 2.6.

The plots in Figure 6.6 correspond to a region of scattering parameters which is restricted in S_c (see rectangle in Figure 6.6 (g)). This case is therefore similar to the one shown in Figure 6.4 where S_c is held fixed while S_a was varied. The different k_n behave similar to that case. The main difference is k_0, which does not show the clear increase with the scattering rate here. It needs to be noted that S_c is significantly higher in this case ($S_c = 0.2 \ldots 0.25$) as compared to Figure 6.4 ($S_c = 0.13$).

Figure 6.7 depicts essentially the same plots as Figure 6.6 but for a different region of saturation parameters. Here, the amplification intensity is restricted and the behavior of the k_n is significantly different from the one for fixed or restricted cooling intensity. In this case k_2 stays approximately constant over the scattering rate, meaning that the WPM of the oscillation does not depend on the scattering rate in this case. In contrast to Figure 6.4 (c), k_0 decreases with the scattering rate before reaching a approximately constant plateau, and so does the minimum of the Allan variance. Again k_{-2} behaves similarly to k_0 but the correlation is not as strong as for the case in Figure 6.4.

We can therefore conclude, that the behavior of the different noise components strongly depends on the chosen region of saturation parameters. For a restricted region of the amplification saturation parameter S_a, the phase diffusion (proportional to k_0) and the minimum of the Allan variance decrease over the scattering rate if the cooling saturation parameter is varied. This can be interpreted as an increase in clock performance with an increase in waste heat production. However, we observe the opposite case if we restrict S_c and vary S_a.

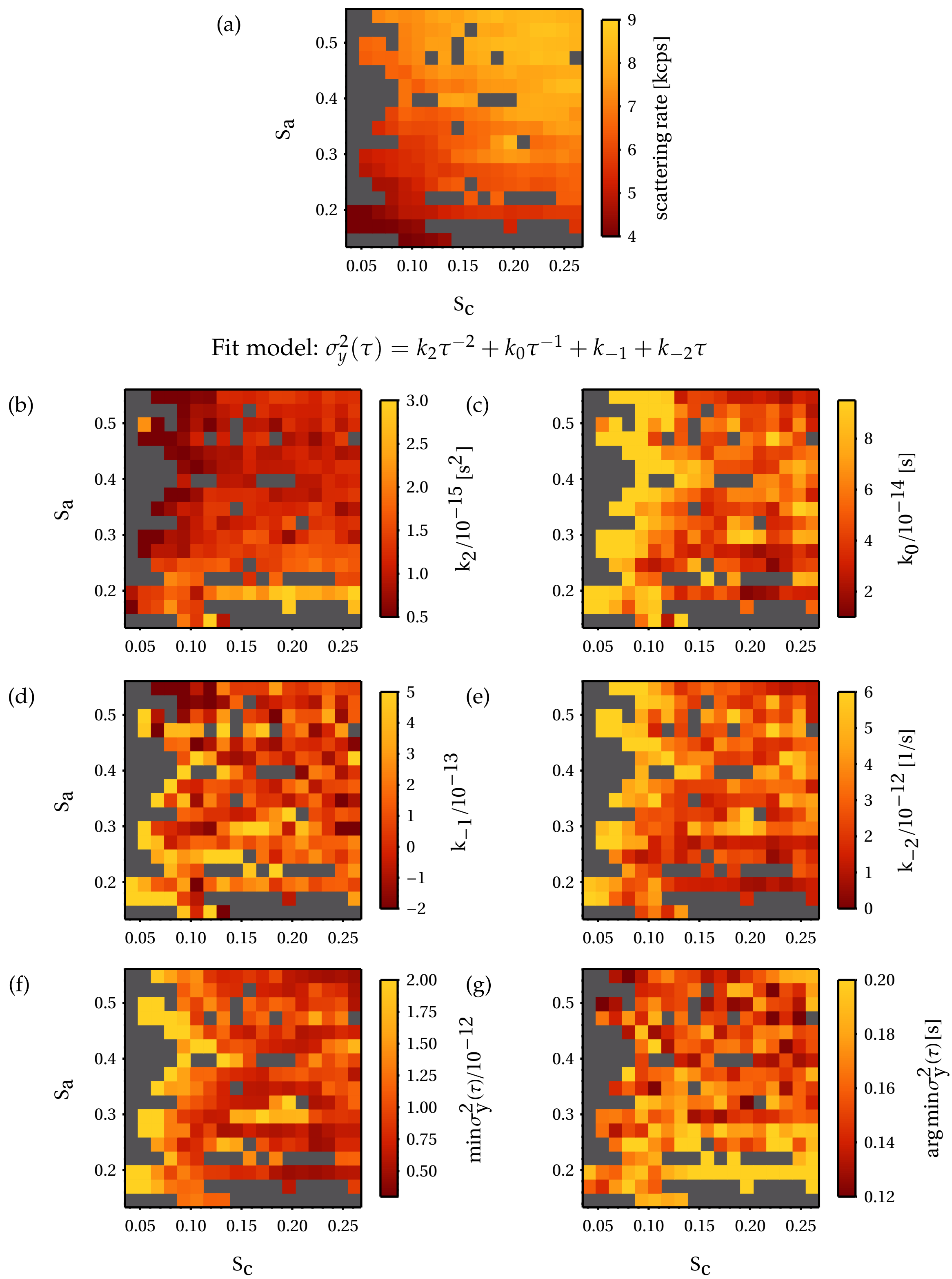

Figure 6.5.: Evaluation of a scan of both cooling (S_c) and amplification (S_a) saturation parameters ($\alpha_c = -6.3$, $\alpha_{a-} = -0.81$, $\alpha_{a+} = -0.21$ (?)). (a) Scattering rate over resonant saturation parameters. (b)-(e) Fit parameters for the Allan variance fit (model depicted above). (f), (g) The minimal value of the Allan variance ($\min \sigma_y^2(\tau)$) and the value of τ at that point ($\arg\min \sigma_y^2(\tau)$) respectively. The grey squares correspond to measurements that have been identified as outliers. (measurement from 02.11.2018)

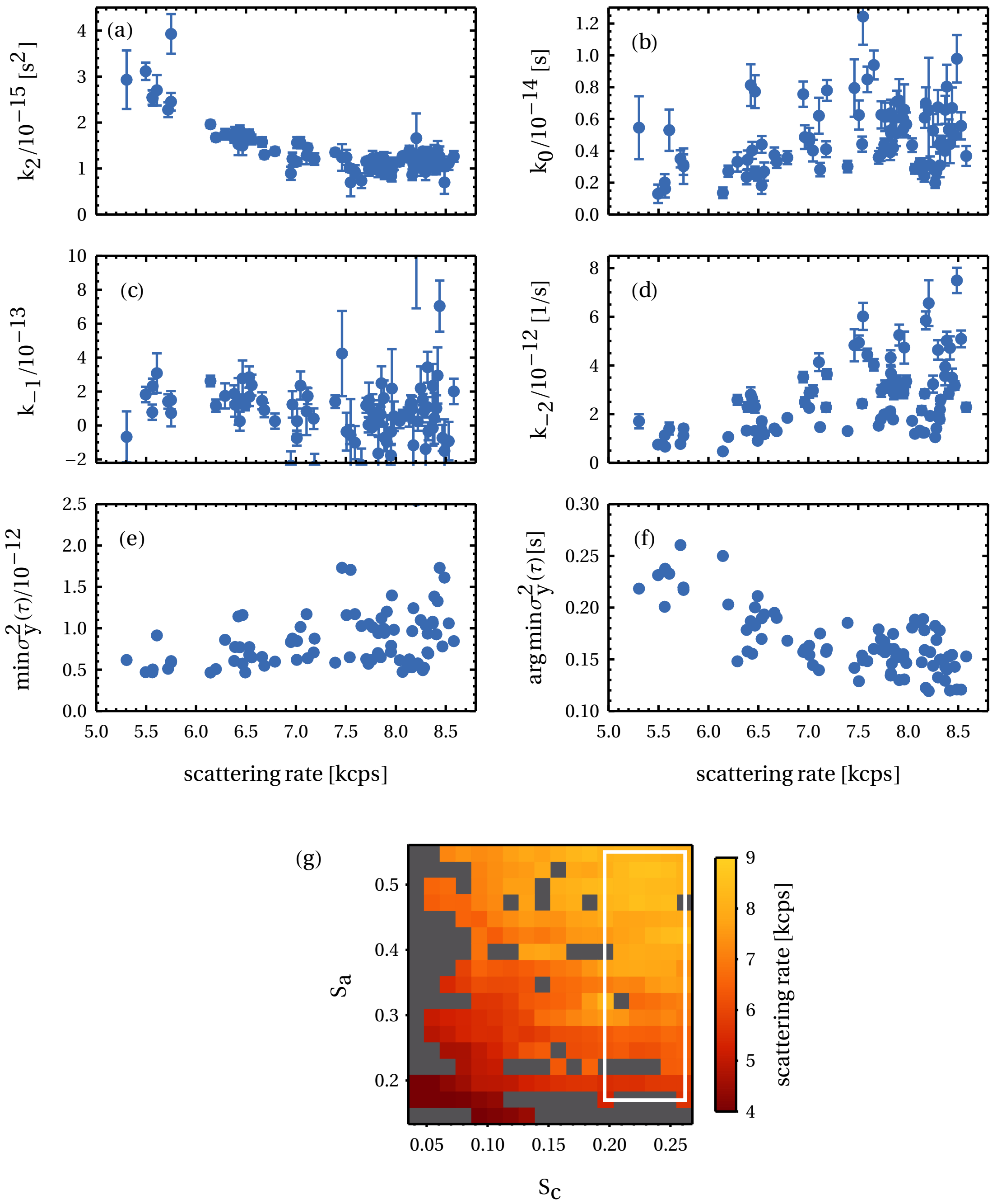

Figure 6.6.: Same data as in Figure 6.5. For a selected region of resonant saturation parameters (depicted by the white rectangle in (g)) the fit parameters for the Allan variance fit versus the corresponding scattering rates are depicted in (a)-(d). (e) and (f) are the minimal value of the Allan variance ($\min \sigma_y^2(\tau)$) and the value of τ at that point ($\arg\min \sigma_y^2(\tau)$) respectively. See also Figure C.2 for plots of the full region. (measurement from 02.11.2018)

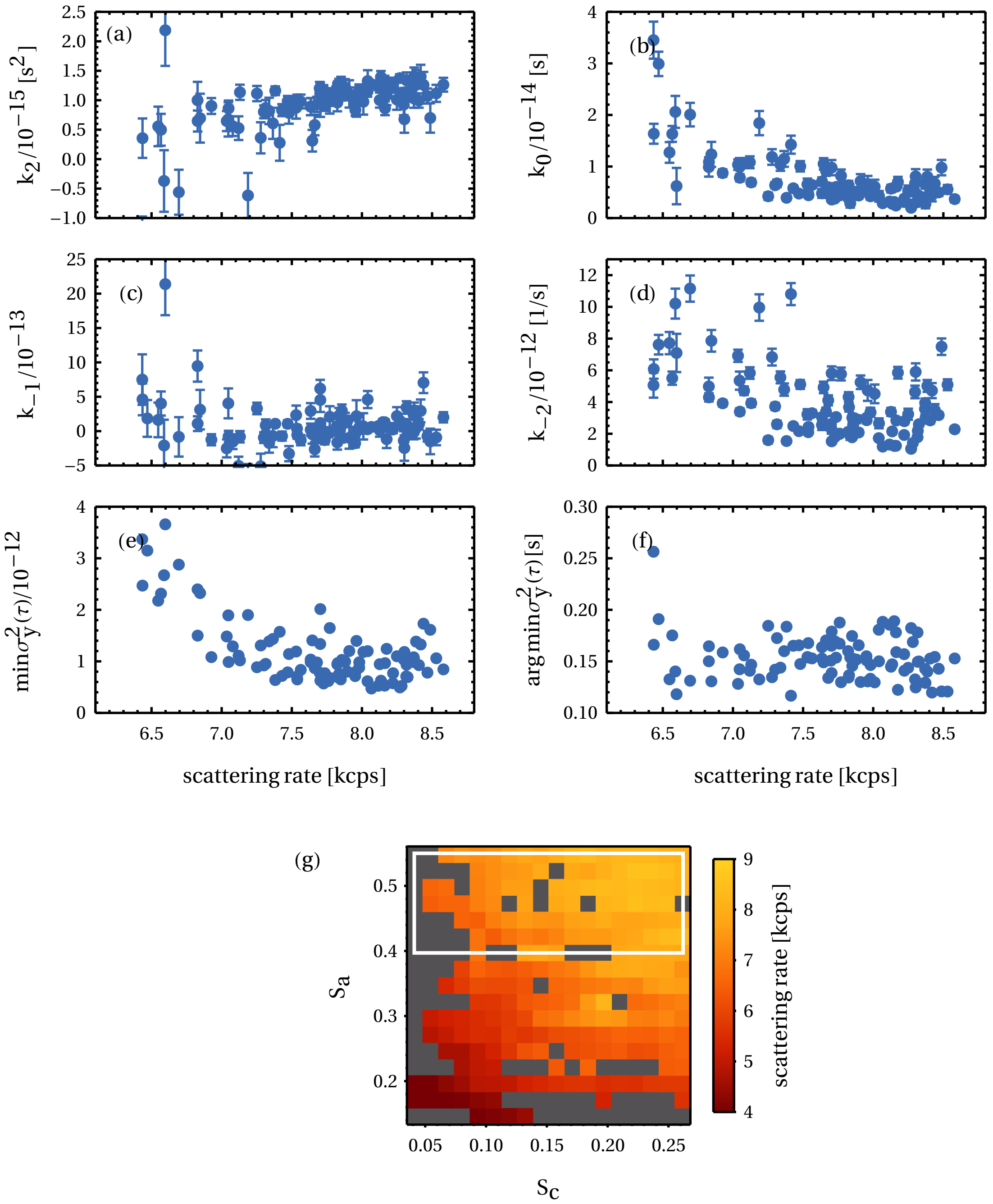

Figure 6.7.: Completely analogous to Figure 6.6 but for a different region of resonant saturation parameters. For this region the behavior of the plotted parameters is significantly different from the case depicted in Figure 6.6. (measurement from 02.11.2018)

7. Discussion

Here we will further discuss the measurements presented in Chapter 6. The goal will be to compare the results to the theory that has been developed in Section 2.2.2 and to investigate possible connections between oscillation stability and waste heat production. Unfortunately the measurement results are not conclusive and difficult to interpret. We will therefore discuss multiple interesting aspects of the data.

The saturation parameter region of stable oscillation can be seen both in Figure 6.5 by the points filtered out as outliers and in Figure C.3 by the stability of the frequency. In both cases this region qualitatively fits the theoretical prediction as depicted in Figure 2.6. There is a threshold behavior for both the amplification and the cooling intensity, below the threshold no stable oscillation is possible, and there is a triangular stability region. Quantitatively however, the stability region does not fit the theory. Theoretically, the stability region should be symmetrical in S_a and S_c (see Figure 2.6) for equal detunings. If one of the detunings is larger than the other, the stability region will be shifted such that the corresponding saturation parameter is also larger on the symmetry axis of this region [1] . In the measurement the case is however the opposite: The cooling detuning is significantly larger then the amplification detuning, and still S_a is about two times larger then S_c on the symmetry axis.

To judge the validity of the assumption that our system behaves like a two-level system (TLS), we evaluate the number of scattered photons per oscillation cycle. The detected scattering rates in the measurements depicted in Figure 6.4 and Figure 6.5 are in the range of $2 \dots 9$ kcps which corresponds to a mean value of $\approx 1 \dots 5$ scattered photons per oscillation cycle. This means that on the order of one or more photons are scattered per cycle and consequently, that the two magnetic sublevels of the $S_{1/2}$ ground state can be depleted during a cycle by one of the beams which would change the scattering behavior of the other one. In order to get as close to the behavior of a TLS as possible, we would need to use even lower scattering rates such that the number of scattered photons per cycle is $\ll 1$. Nevertheless, the scattering rate predicted by the theory for the values of the saturation parameters and detunings in Figure 6.4, fit the measurement relatively well.

The measurement of the different noise components however do not agree with the theory. The random walk frequency modulation (RWFM) intensity, corresponding to the linear part of the Allan variance k_{-2}, should be independent of the the saturation parameters of the laser as only technically induced noise should lead to a random walk in frequency. This is not the case in the measurements. It is also interesting to note, that k_{-2} behaves similarly to k_0 which is proportional to the random walk phase modulation

[1] By symmetry axis we understand the bisection of the triangular stability region.

(RWPM). From the theoretical model it is unclear why these two quantities should be connected. Furthermore, the white phase modulation (WPM) part k_2 should increase with the scattering rate rather then decrease due to broadening at higher saturation parameters. However, only in the selected region in Figure 6.7 can a slight increase be observed, while it decreases significantly over the scattering rate in the other cases.

The k_0 component is proportional to the RWPM intensity and therefore to the phase diffusion coefficient. Its behavior depends strongly on the chosen region of saturation parameters. If S_c is held fixed and S_a is varied, it increases with the scattering rate as depicted in Figure 6.4 (c). In the opposite case it decreases with the scattering rate as depicted in Figure 6.7 (b). This contradicts the theoretical predictions. Using the theoretical model, we see in Figure 2.9 that for fixed S_c the phase diffusion coefficient rapidly decreases with increasing S_a (and thus increasing scattering rate) once the oscillation threshold has been reached.

These results make it difficult to give a final statement about the connection of oscillation stability and waste heat production in this system. Clearly, we can not just arbitrarily increase the waste heat production by increasing any laser intensity and expect the clock accuracy to go up. But for certain cases, an increase in scattering rate coincides with an decrease in certain noise components. Furthermore, the measurements show that our theoretical model does not fit our system very well. While the scattering rate could be reproduced relatively well, the measured noise components and the region of stable oscillation largely contradict the theoretical predictions.

8. Conclusion & Outlook

During the course of this thesis theoretical models have been derived, measurement schemes where presented and the resulting data was thoroughly discussed. In this chapter we will give a summary over these achievements and their relation to each other and discuss remaining problems and possible improvements.

We have presented a concept to implement an autonomous clock based on a trapped $^{40}Ca^{+}$ ion phonon laser. This system can be seen as the microscopic limit of a pendulum clock. We have implemented this phonon laser in a Paul trap in which the sustained oscillation of the ion is driven with two lasers, damping (cooling) and amplifying the motion by exciting the $4S_{1/2} \leftrightarrow 4P_{1/2}$ transition. In order to obtain a better understanding of the stability of this clock, we have derived a theoretical model which allows for characterization of the phase stability of the oscillation via the phase diffusion coefficient D_ϕ. We can evaluate D_ϕ in terms of the operating parameters of the clock and found interesting behaviors in connection with the rate of photons scattered by the ion, our measure of waste heat production of the ion oscillator. To evaluate the stability of the clock we have developed a method to compute the Allan variance of the oscillation frequency using the detection times of the scattered photons during oscillation. This required well chosen methods for the outlier removal from the frequency samples to obtain a faithful measure of the Allan variance. The Allan variance was used to evaluate different noise components that can be connected to quantities from the theoretical model and to technical sources of noise. Measurements have been presented which connect these noise components with the intensities of the two driving lasers and therefore to the scattering rate of the ion. These measurements show systematic dependencies of the noise components on the scattering rate and the laser intensities which however contradict the theoretical model in large parts. Solely the measured scattering rate predicted by the theory was reproduced in relatively good agreement in the measurement. The behavior of the noise intensity corresponding to long term phase stability (random walk phase modulation (RWPM)) is strongly dependent on the way the scattering rate in increased. By increasing the amplification intensity, we found an increase of the noise with increasing scattering rate while the phase stability improved with increasing scattering rate if the cooling intensity was increased. The latter case can be interpreted as an argument for the conjectured connection between time measurement and thermodynamics by Erker et al. presented in Section 1.1. However, this connection is evidently neither universal nor well understood for our system at hand.

Additionally to these measurements on the autonomous ion clock, we have presented a novel scheme to calibrate the parameters of a laser beam driving an electric dipole transition of an atomic multilevel system. In contrast to existing approaches, the one presented here is less sensitive to radiation pressure effects, as very few scattered photons

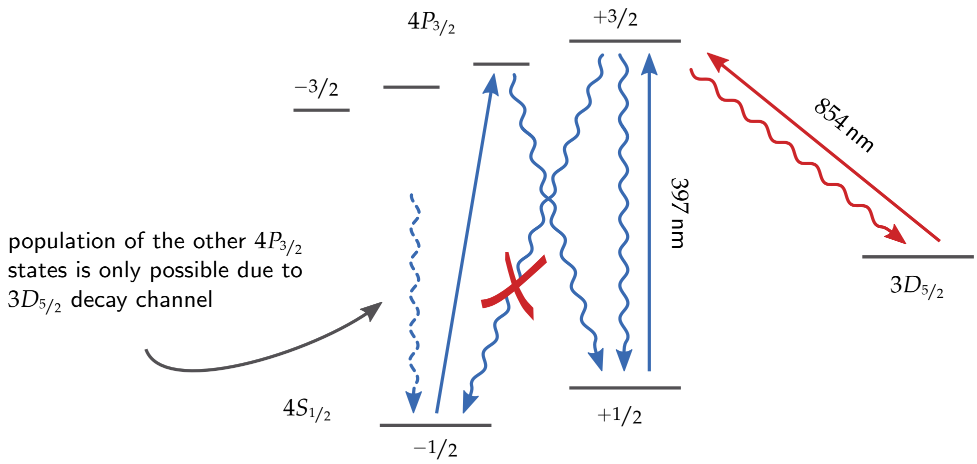

Figure 8.1.: Level scheme and transitions for the proposed change to the $4S_{1/2} \leftrightarrow 4P_{3/2}$ transition. By using σ_+ polarized light, the population will be pumped into the $4S_{1/2}$, $m_j = 1/2$ state from which only the transition into the $m_j = 3/2$ state is possible. Decay back into $m_j = -1/2$ is prohibited as $\Delta m_j = -2$. Due to the branching into $3D_{5/2}$, other m_j states can become populated. However, these states are then again depleted due to the pumping and additionally the effect is small as the branching is strongly suppressed.

per experimental run are sufficient. This method enables the calibration of the saturation parameter and the frequency detuning relative to the dipole transition to values which are readily accessible in the lab, i.e. photo diode voltages or power meter readings and acousto-optical modulator (AOM) frequencies. Furthermore, we introduced a technique to measure the photon detection efficiency of our setup by extracting a known amount of photons from the ion. In the measurements of the clock stability we use the calibration to determine the operation parameters which can in turn be connected to the theoretical model, and the detection efficiency to compare the measured and expected scattering rates.

We can summarize, that the presented experimental platform and the method to detect and analyze the oscillation stability of our clock is principally suited to address the fundamental question of this thesis: "Does thermodynamics limit our ability to measure time?" [16]. The stability of the clock can be measured using the Allan variance and the thermodynamical cost for running the clock is given by the waste heat in terms of scattered photons, which can easily be measured. However, multiple problems still persist. The theoretical model we have used does assume an ideal two-level system which is not given for the dipole transition we have used. This might lead to fundamentally different behavior which could explain the deviations of the measurements from the theoretical predictions. Even though the measured scattering rate fits the theory relatively well, we find that the average number of scattered photons per oscillation cycle is > 1. This means that the involved levels can be depleted during a single cycle, further enforcing the thesis that a two-level system is not a good approximation. Additionally, strong technical noise could dominate the oscillation stability which would make it impossible to detect the phase stability intrinsic to the driven ion oscillator.

Multiple methods to approach these problems are conceivable. To reduce the effect of technical noise, a trap with stronger filters could be used. To eliminate the discrepancy between the experimental system and the theoretical model, the model could be extended to a multilevel system. While this would be possible, it would be tedious and we would still be left with a relatively complex system. The alternative solution is to use a different transition which approximates the ideal two-level system better. Such a candidate could be the $4S_{1/2} \leftrightarrow 4P_{3/2}$ transition as depicted in Figure 8.1. Here the highest m_j state of the excited level is $3/2$ and thus greater by one then the highest m_j state of $1/2$ of the ground state. If we drive the transition with σ_+ polarized light, we will pump the population into the $4S_{1/2}$, $m_j = 1/2$ state. From there, only transitions into the $m_j = 3/2$ state are possible from where decays are only allowed back into the $m_j = 1/2$ state. We thus have a closed transition between two levels. The only imperfection is caused by decay into the metastable $D_{5/2}$ state. Population needs to be repumped which in turn leads to repopulation of the $4S_{1/2}$, $m_j = -1/2$ state. As the branching to the $D_{5/2}$ state is suppressed by a factor of 17.6 [34] this can be seen as a small perturbation. Plans to implement this configuration in an existing experiment are under discussion at the moment.

Appendix

Appendix A.

Evaluation of Integral Expressions

Here we evaluate the integral expressions needed for the derivations in Section 2.2.2. These derivation have been developed by Nahuel Freitas during joined work on the subject.

First we derive the expressions for G and K defined in Equation (2.46). We use integration by parts to obtain:

$$\begin{aligned} G(v) &= \frac{1}{\pi}\int_0^{2\pi} d\theta\, \frac{1}{mS_a}\frac{dF_a}{dv}(v\cos(\theta))\sin^2(\theta) \\ &= \frac{1}{\pi}\frac{1}{v}\int_0^{2\pi} d\theta\, \frac{1}{mS_a}F_a(v\cos(\theta))\cos(\theta) \\ &= \frac{1}{\pi}\frac{1}{v}\frac{\hbar k}{m}\frac{\gamma}{2}\int_0^{2\pi} d\theta\, \frac{\cos(\theta)}{1+(2\delta_a/\gamma+2kv/\gamma\,\cos(\theta))^2}\,. \end{aligned} \tag{A.1}$$

Using the tangent half-angle substitution the last integral can be rewritten as:

$$G(\alpha_a,\beta) = \frac{1}{\pi}\frac{2k}{\beta\gamma}\frac{\hbar k}{m}\frac{\gamma}{2}\int_{-\infty}^{+\infty} dt\, \frac{2(1-t^2)}{(1+t^2)^2+(\alpha_a(1+t^2)-\beta(1-t^2))^2} \tag{A.2}$$

where we have defined the dimensionless parameters $\alpha_a = 2\delta_a/\gamma$ and $\beta = 2kv/\gamma$. This integral can be solved using the residue theorem. The integrand has four poles t_k ($k = 1, \cdots, 4$), which can be chosen so that $t_1 = -t_2^* = -t_3 = t_4^*$. Using these symmetries, the result of the integral can be expressed in terms of a single pole and its residue and reads:

$$G(\alpha_a,\beta) = \frac{1}{\pi}\frac{\hbar k^2}{m}\frac{1}{\beta}\frac{1}{1+(\alpha_a+\beta)^2}\frac{2\pi i}{(t_1+t_1^*)(t_1-t_1^*)}\left[\frac{1-t_1^2}{t_1}+\frac{1-t_1^{*2}}{t_1^*}\right], \tag{A.3}$$

where t_1 is a solution of

$$t_1^2 = \frac{\pm 2i\beta-(1+\alpha_a^2-\beta^2)}{1+(\alpha_a+\beta)^2} \tag{A.4}$$

with positive real and imaginary parts. Using the last two equations the following closed expression can be derived:

$$G(\alpha_a,\beta) = \frac{\hbar k^2}{m}\frac{1}{\beta}\frac{\sqrt{2}/\sqrt{1+(\alpha_a-\beta)^2}-\sqrt{2}/\sqrt{1+(\alpha_a+\beta)^2}}{\sqrt{1+(\alpha_a-\beta)(\alpha_a+\beta)+\sqrt{1+(\alpha_a-\beta)^2}\sqrt{1+(\alpha_a+\beta)^2}}} \tag{A.5}$$

A similar expression is obtained for $K(v)$, where $K(\alpha_c, \beta) = -G(\alpha_c, \beta)$, with $\alpha_c = 2\delta_c/\gamma < 0$.

Two other integrals are relevant. First, to calculate the phase diffusion constant we need to evaluate

$$\begin{aligned} I_D &= \frac{1}{S_j \gamma/2} \int_0^{2\pi} d\theta \, R_j(\omega A_0 \cos(\theta)) \sin^2(\theta) \\ &= \int_0^{2\pi} d\theta \, \frac{\sin^2(\theta)}{1 + (2\delta_j/\gamma + 2kv/\gamma \, \cos(\theta))^2} \end{aligned} \tag{A.6}$$

Using the same kind of procedure as before, we obtain

$$I_D(\alpha_j, \beta) = \frac{\pi\sqrt{2}}{\beta^2} \left[\frac{\sqrt{1 + (\alpha_j + \beta)^2} + \sqrt{1 + (\alpha_j - \beta)^2}}{\sqrt{1 + (\alpha_j - \beta)(\alpha_j + \beta) + \sqrt{1 + (\alpha_j - \beta)^2}\sqrt{1 + (\alpha_j + \beta)^2}}} - \sqrt{2} \right] , \tag{A.7}$$

and the phase diffusion coefficient reads

$$D_\phi = \frac{z}{4\pi} \left(\frac{\hbar k^2}{m} \right)^2 \frac{1}{\gamma/2} \frac{1}{\beta^2} \left[S_c I_D(\alpha_c, \beta) + S_a I_D(\alpha_a, \beta) \right] . \tag{A.8}$$

Finally, the total number of scattered photons during a cycle is:

$$\begin{aligned} N_c &= \frac{1}{\omega} \int_0^{2\pi} d\theta \, \left[R_c(\omega A_0 \cos(\theta)) + R_a(\omega A_0 \cos(\theta)) \right] \\ &= \frac{\gamma/2}{\omega} \left[S_c I_N(\alpha_c, \beta) + S_a I_N(\alpha_a, \beta) \right] , \end{aligned} \tag{A.9}$$

where $I_N(\alpha, \beta)$ is given by:

$$I_N(\alpha, \beta) = \pi \, \frac{\sqrt{2}/\sqrt{1 + (\alpha - \beta)^2} + \sqrt{2}/\sqrt{1 + (\alpha + \beta)^2}}{\sqrt{1 + (\alpha - \beta)(\alpha + \beta) + \sqrt{1 + (\alpha - \beta)^2}\sqrt{1 + (\alpha + \beta)^2}}} . \tag{A.10}$$

Appendix B.

Theoretical Analysis of the Ion Oscillator

Here, we summarize various plots relevant for the theoretical model of the ion oscillator discussed in Section 2.2. Their context is explained there and in the corresponding captions of the figures.

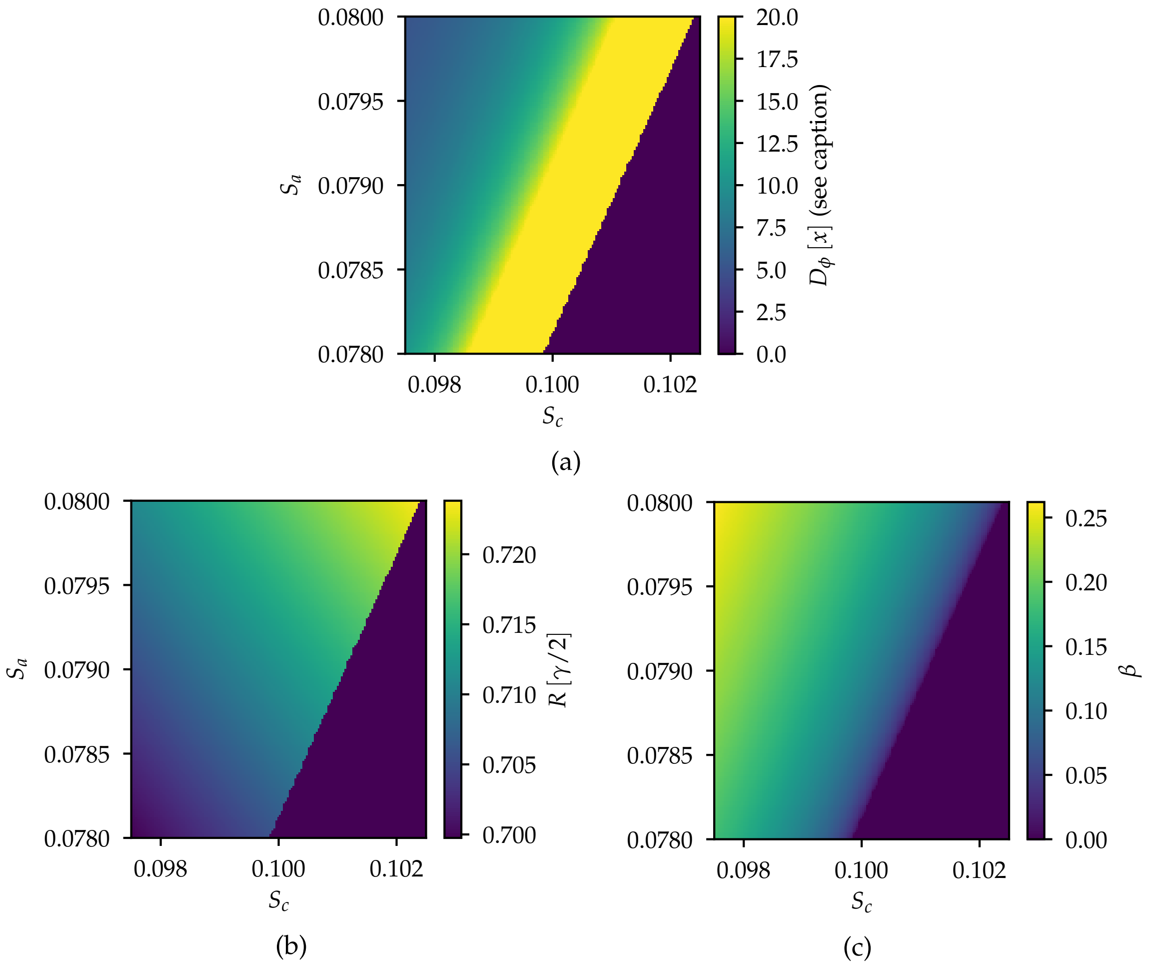

Figure B.1.: (a) Phase diffusion coefficient D_ϕ in units of $x = (g/(4\pi))\,(\hbar k^2/m)^2\,1/(\gamma/2)$ over amplification saturation parameter S_a and cooling saturation parameter S_c for $\alpha_c = -1,\ \alpha_a = 0.5$. (b) depicts the total scattering rate R and (c) the operating amplitude β_{OP}.

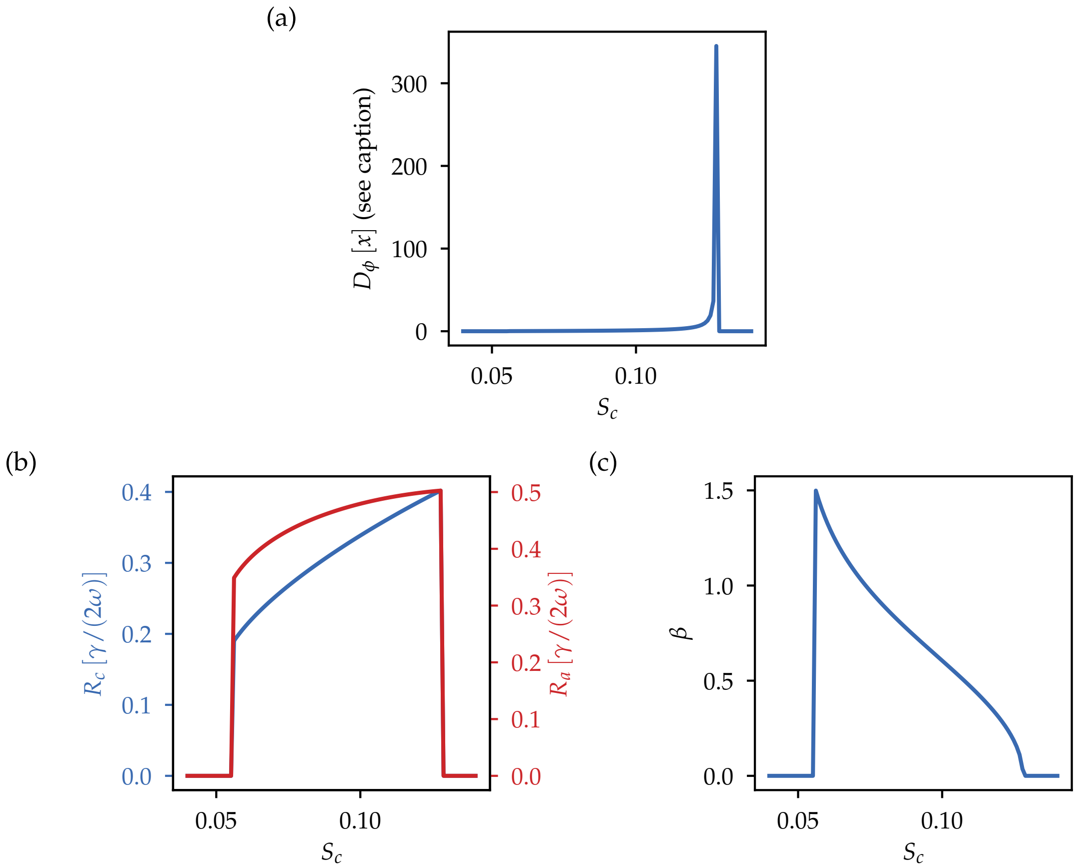

Figure B.2.: (d) Phase diffusion coefficient D_ϕ in units of $x = (g/(4\pi))\,(\hbar k^2/m)^2\, 1/(\gamma/2)$ over amplification saturation parameter for $S_a = 0.1,\ \alpha_c = -1,\ \alpha_a = 0.5$. (b) the total scattering rate R and (c) the operating amplitude β_{OP}. These plots are analogous to the ones in Figure 2.9 with the difference that here S_a is held fixed instead of S_c. The behavior of D_ϕ with respect to the scattering rate is opposite to the case in Figure 2.9. Here, it increases for increasing scattering rate.

Appendix C.

Oscillation Stability Measurements

Here, we summarize various plots relevant for the measurements discussed in Chapter 6. Their context is explained there and in the corresponding captions of the figures.

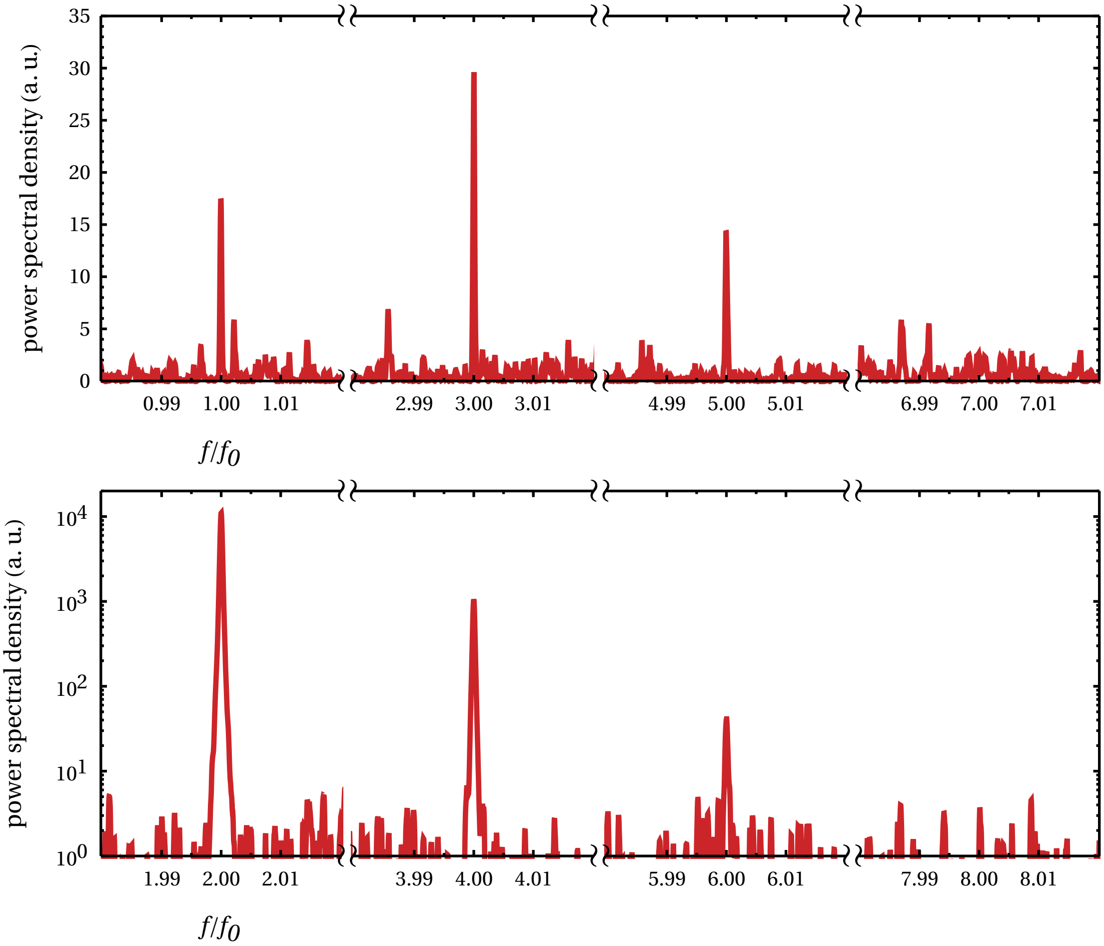

Figure C.1.: Power spectral density of the photon time stamps. These spectra have been computed using the Fourier transform of the autocorrelation function, a method, that has not been discussed above. Upper panel for odd multiples of the trap frequency ($f_0 = 1.484\,89\,\mathrm{MHz}$). Lower panel for even multiples of the trap frequency.

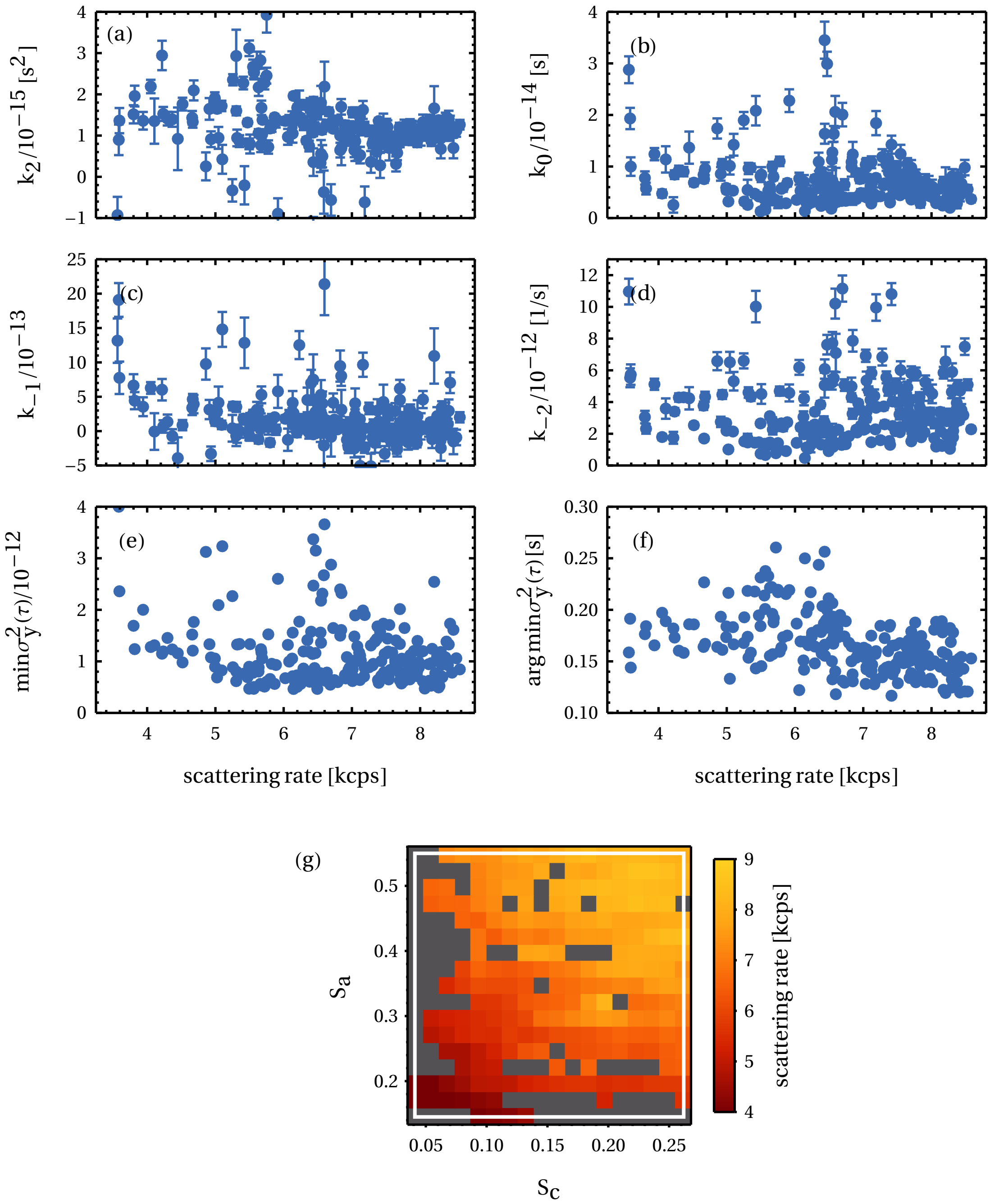

Figure C.2.: Fitted coefficients of the Allan variance over the saturation parameters S_a and S_c. Completely analogous to Figure 6.6 and Figure 6.7, but including all data points. Systematic behavior is by far not as evident as in the aforementioned figures. (measurement from 02.11.2018)

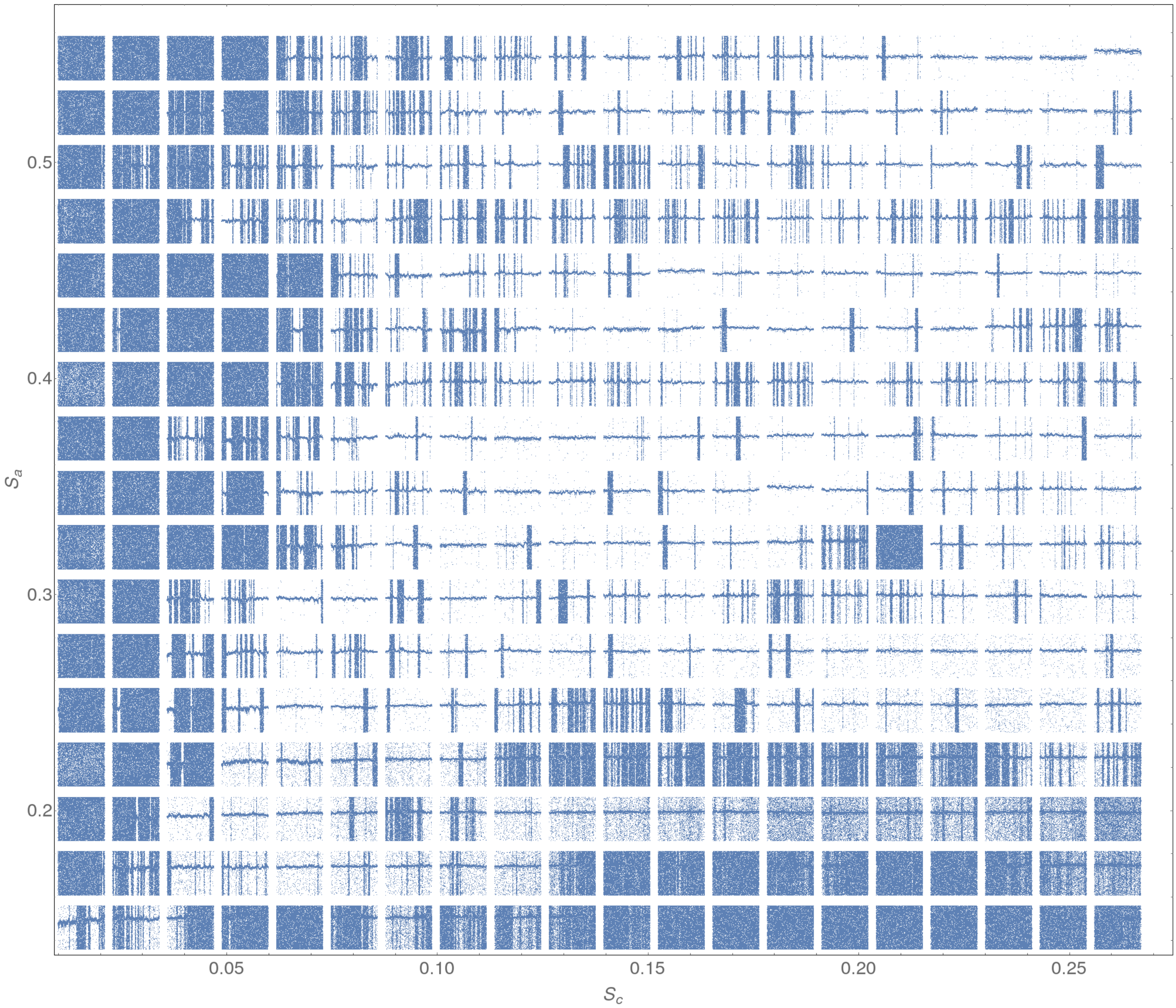

Figure C.3.: Plots of the resonance frequencies over time (analogous to Figure 6.2 before the outlier removal) over saturation parameters of the measurements depicted in Figure 6.5. Each inset plot is over a 5 min measurement and the y-axis range is 1.5 kHz. (measurement from 02.11.2018)

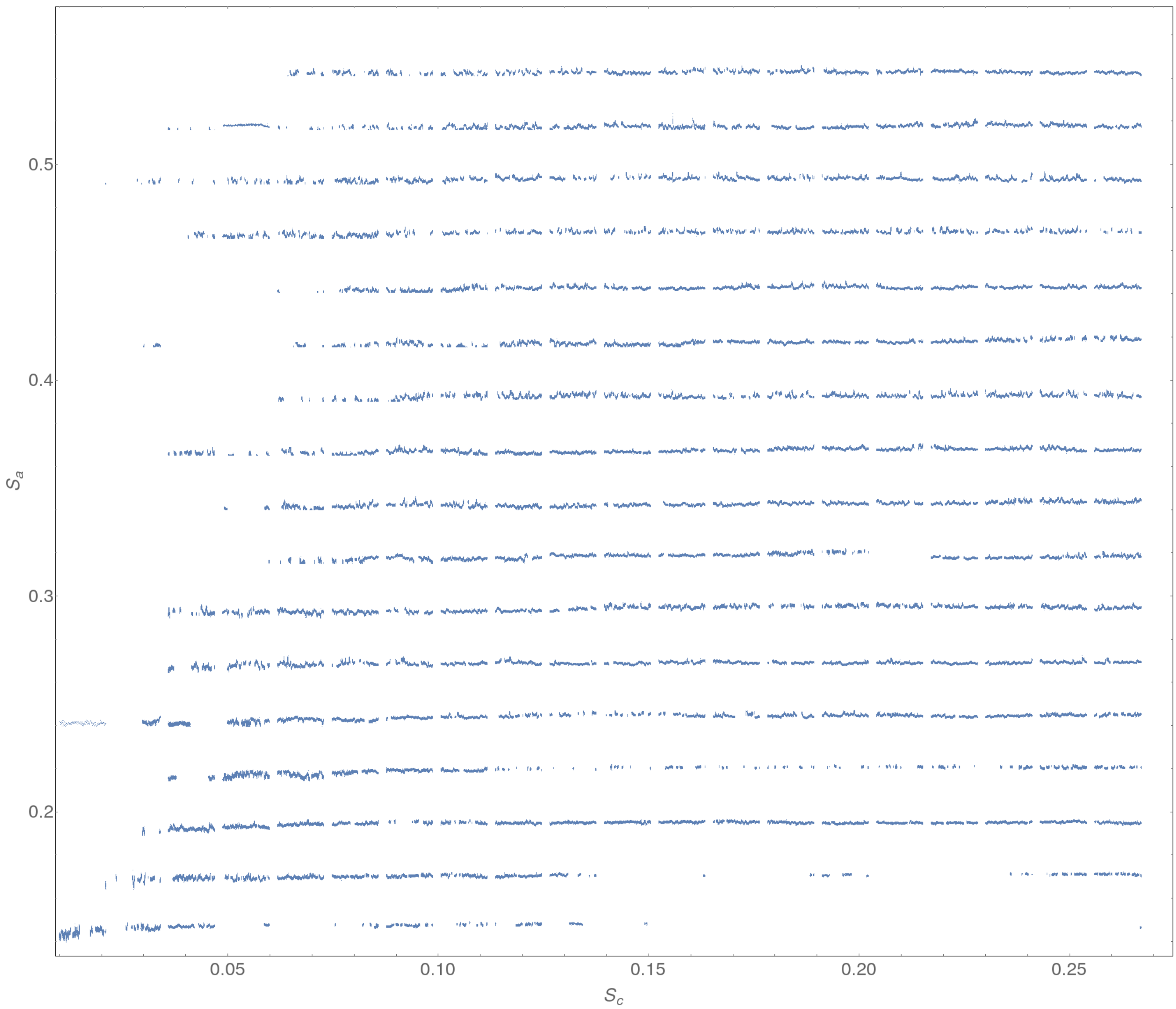

Figure C.4.: Completely analogous to Figure C.3 but after the outlier removal. Here the frequency (x-axis) range of the inset plots is adjusted for each plot individually.

Bibliography

[1] Wolfgang Paul and Helmut Steinwedel. "Ein neues massenspektrometer ohne magnetfeld." In: *Zeitschrift für Naturforschung A* 8.7 (1953), pp. 448–450 (cit. on pp. 1, 33).

[2] Wolfgang Paul. "Electromagnetic traps for charged and neutral particles." In: *Reviews of modern physics* 62.3 (1990), p. 531 (cit. on pp. 1, 33).

[3] David J Wineland and Wayne M Itano. "Laser cooling of atoms." In: *Physical Review A* 20.4 (1979), p. 1521 (cit. on p. 1).

[4] Ch Monroe et al. "Resolved-sideband Raman cooling of a bound atom to the 3D zero-point energy." In: *Physical Review Letters* 75.22 (1995), p. 4011 (cit. on p. 1).

[5] F Schmidt-Kaler et al. "Ground state cooling, quantum state engineering and study of decoherence of ions in Paul traps." In: *Journal of Modern Optics* 47.14-15 (2000), pp. 2573–2582 (cit. on p. 1).

[6] Dietrich Leibfried et al. "Quantum dynamics of single trapped ions." In: *Reviews of Modern Physics* 75.1 (2003), p. 281 (cit. on p. 1).

[7] Thomas Monz et al. "14-qubit entanglement: Creation and coherence." In: *Physical Review Letters* 106.13 (2011), p. 130506 (cit. on p. 1).

[8] T Ruster et al. "Entanglement-based dc magnetometry with separated ions." In: *Physical Review X* 7.3 (2017), p. 031050 (cit. on p. 1).

[9] Rainer Blatt and Christian F Roos. "Quantum simulations with trapped ions." In: *Nature Physics* 8.4 (2012), p. 277 (cit. on p. 1).

[10] Thomas Monz et al. "Realization of a scalable Shor algorithm." In: *Science* 351.6277 (2016), pp. 1068–1070 (cit. on p. 1).

[11] Johannes Roßnagel et al. "A single-atom heat engine." In: *Science* 352.6283 (2016), pp. 325–329 (cit. on p. 1).

[12] David von Lindenfels et al. "A spin heat engine coupled to a harmonic-oscillator flywheel." In: *arXiv preprint arXiv:1808.02390* (2018) (cit. on p. 1).

[13] Udo Seifert. "Stochastic thermodynamics, fluctuation theorems and molecular machines." In: *Reports on progress in physics* 75.12 (2012), p. 126001 (cit. on p. 1).

[14] Nicolas Brunner et al. "Entanglement enhances cooling in microscopic quantum refrigerators." In: *Physical Review E* 89.3 (2014), p. 032115 (cit. on p. 1).

[15] Armen E Allahverdyan, Roger Balian, and Th M Nieuwenhuizen. "Maximal work extraction from finite quantum systems." In: *EPL (Europhysics Letters)* 67.4 (2004), p. 565 (cit. on p. 1).

[16] Paul Erker et al. "Autonomous quantum clocks: does thermodynamics limit our ability to measure time?" In: *Physical Review X* 7.3 (2017), p. 031022 (cit. on pp. 1–6, 31, 73, 74).

[17] Rolf Landauer. "Irreversibility and heat generation in the computing process." In: *IBM journal of research and development* 5.3 (1961), pp. 183–191 (cit. on p. 1).

[18] Norman Margolus and Lev B Levitin. "The maximum speed of dynamical evolution." In: *Physica D: Nonlinear Phenomena* 120.1-2 (1998), pp. 188–195 (cit. on p. 1).

[19] Kerry Vahala et al. "A phonon laser." In: *Nature Physics* 5.9 (2009), p. 682 (cit. on pp. 1, 6, 16, 19, 22).

[20] AE Kaplan. "Single-particle motional oscillator powered by laser." In: *Optics Express* 17.12 (2009), pp. 10035–10043 (cit. on pp. 1, 6).

[21] Nicolas Brunner et al. "Virtual qubits, virtual temperatures, and the foundations of thermodynamics." In: *Physical Review E* 85.5 (2012), p. 051117 (cit. on p. 3).

[22] Brian Harold Bransden, Charles Jean Joachain, and Theodor J Plivier. *Physics of atoms and molecules*. Pearson Education India, 2003 (cit. on p. 11).

[23] Theodor W Hänsch and Arthur L Schawlow. "Cooling of gases by laser radiation." In: *Optics Communications* 13.1 (1975), pp. 68–69 (cit. on pp. 15, 34, 52).

[24] D. J. Wineland and H. Dehmelt. "Proposed 10^{14} $\Delta\nu < \nu$ Laser Fluorescence Spectroscopy on TL^+ Mono-Ion Oscillator III." In: *Bulletin of the American Phys- ical Society* 20.637 (1975) (cit. on pp. 15, 34, 52).

[25] Crispin Gardiner. *Stochastic methods*. Vol. 4. springer Berlin, 2009 (cit. on pp. 16, 18).

[26] Henning Kaufmann. "A scalable quantum processor." Phd thesis. JGU Mainz, 2018. URL: `http://nbn-resolving.org/urn:nbn:de:hebis:77-diss-1000018985` (cit. on pp. 33, 34).

[27] Thomas Ruster. "Entanglement-based magnetometry in a scalable ion-trap quantum processor." Phd thesis. JGU Mainz, 2017 (cit. on pp. 33, 49).

[28] S Gulde et al. "Simple and efficient photo-ionization loading of ions for precision ion-trapping experiments." In: *Applied Physics B* 73.8 (2001), pp. 861–863 (cit. on p. 33).

[29] Eric D Black. "An introduction to Pound–Drever–Hall laser frequency stabilization." In: *American journal of physics* 69.1 (2001), pp. 79–87 (cit. on p. 34).

[30] T. Macha. "Frequenzstabilisierung eines Titan-Saphir-Lasers und Verbesserung von Qubits mit Ca^+-Ionen." Diploma thesis. JGU Mainz, 2012 (cit. on p. 36).

[31] U.G. Poschinger. "Quantum Optics Experiments in a Microstructured Ion Trap." Phd thesis. Universität Ulm, 2010 (cit. on p. 39).

[32] T. W. Deuschle. "Kalte Ionenkristalle in einer segmentierten Paul-Falle." Phd thesis. Universität Ulm, 2007 (cit. on p. 39).

[33] A Kreuter et al. "Experimental and theoretical study of the 3 d D 2–level lifetimes of Ca+ 40." In: *Physical Review A* 71.3 (2005), p. 032504 (cit. on p. 40).

[34] C. F. Roos. “Controlling the quantum state of trapped ions.” Phd thesis. Leopold-Franzens-Universität Innsbruck, 2000 (cit. on pp. 40, 75).

[35] M Hettrich et al. “Measurement of dipole matrix elements with a single trapped ion.” In: *Physical review letters* 115.14 (2015), p. 143003 (cit. on p. 44).

[36] Eugene P Wigner. “On the matrices which reduce the Kronecker products of representations of SR groups.” In: *The Collected Works of Eugene Paul Wigner*. Springer, 1993 (cit. on p. 45).

[37] VS Malinovsky and JL Krause. “General theory of population transfer by adiabatic rapid passage with intense, chirped laser pulses.” In: *The European Physical Journal D-Atomic, Molecular, Optical and Plasma Physics* 14.2 (2001), pp. 147–155 (cit. on p. 48).

[38] David W Allan. “Statistics of atomic frequency standards.” In: *Proceedings of the IEEE* 54.2 (1966), pp. 221–230 (cit. on p. 58).

[39] Fritz Riehle. *Frequency standards: basics and applications*. John Wiley & Sons, 2006 (cit. on pp. 58, 59).

[40] David W Allan and James A Barnes. “A modified ‘Allan variance’ with increased oscillator characterization ability.” In: *35th Annual Frequency Control Symposium* (1981) (cit. on p. 58).

[41] Asghar Ghasemi and Saleh Zahediasl. “Normality tests for statistical analysis: a guide for non-statisticians.” In: *International journal of endocrinology and metabolism* 10.2 (2012), p. 486 (cit. on p. 60).

[42] William Cyrus Navidi. *Statistics for engineers and scientists*. McGraw-Hill Higher Education New York, NY, USA, 2008 (cit. on p. 60).